The Assessment of On-Board Clean Hybrid Energy Storage Systems For Railway Locomotives and Multiple Units

by

Mohamed Hegazi

BEng, The University of Nottingham, 2013

A THESIS SUBMITTED IN PARTIAL FULFILLMENT OF THE REQUIREMENTS FOR THE DEGREE OF

MASTER OF APPLIED SCIENCE

in

THE COLLEGE OF GRADUATE STUDIES

(Electrical Engineering)

THE UNIVERSITY OF BRITISH COLUMBIA

(Okanagan)

October 2016

The undersigned certify that they have read, and recommend to the College of Graduate Studies for acceptance, a thesis entitled: The Assessment of On-Board Clean Hybrid Energy Storage Systems For Railway Locomotives and Multiple Units submitted by Mohamed Hegazi in partial fulfilment of the requirements of the degree of Master of Applied Science

Loïc Markley, Applied Science/School of Engineering

Supervisor, Professor (please print name and faculty/school above the line)

Gordon Lovegrove, Applied Science/School of Engineering

Co-Supervisor, Professor (please print name and faculty/school above the line)

Wilson Eberle, Applied Science/School of Engineering

Supervisory Committee Member, Professor (please print name and faculty/school above the line)

Rudolf Seethaler, Applied Science/School of Engineering

University Examiner, Professor (please print name and faculty/school above the line)

26 October 2016

(Date Submitted to Grad Studies)

Abstract

Batteries, supercapacitors, and hydrogen fuel cells are energy storage devices that have no emissions at the point of use. The idea of powering railway locomotives using these devices is one that could, theoretically, eliminate emissions from the railway sector. The motivation behind the research work presented in this thesis is to assess the technical feasibility of employing batteries, supercapacitors, and hydrogen fuel cells in a railway vehicle. This is meant to serve as reference to future work regarding the cost-benefit analysis, well-to-wheel emissions analysis, and life-cycle assessment of railway vehicles that employ these power sources.

In this thesis, the application of on-board clean energy storage systems to railway vehicles were studied. Simulation models for battery/supercapacitor and hydrogen fuel cell/battery hybrid powertrains were developed in Simulink. These models were then used to conduct simulations for two train trips. The first trip selected was the 14 km Trehafod to Treherbert route, on which the British Class 150 diesel motive unit operates. The second trip was the 432 km London to Newcastle trip, on which the Intercity 125 train operates. Since no data regarding freight trains on freight tracks could be obtained, only passenger trains were simulated. The conclusions made at the end of this thesis could potentially apply to freight trains as well.

Based on the case studies considered, it was found out that railway systems are very well suited to run on on-board clean energy storage systems from an energy consumption point of view. Although being slower responding power sources, hydrogen fuel cells proved to be capable of handling dynamic load changes in railway systems to a great extent but still required the assistance of a faster acting power source. Despite having a significantly lower electrochemical efficiency, employing hydrogen fuel cells resulted in increasing the range of travel without re-fueling/recharging due to the high energy density of hydrogen. Lithium ion batteries proved to be very capable in handling all the required transient power demand. In regeneration, supercapacitors outperformed lithium-ion batteries and reduced the need for frictional brakes.

Preface

The work presented in this thesis was made possible through two consecutive grants by Transport Canada under the umbrella of their Clean Rail Grant program.

A technical report containing a portion of Chapter 2 was prepared for Transportation Development Centre of Transport Canada.

A version of Chapter 2 was was published in a technical poster at the 2014 AREMA Annual Conference in Chicago, Illinois.

The work presented in Section 3.3 was published in a technical poster at the 2015 AREMA Annual Conference in Minneapolis, Minnesota.

The results and associated methods in Subsection 4.2.3 were published in the 2016 Canadian Society of Mechanical Engineers International Congress (CSME2016).

The work presented in Subsection 4.2.4 was published in a technical poster at the 2016 AREMA Annual Conference in Orlando, Florida.

Table of Contents

List of Tables

List of Figures

Acronyms

BSC	battery/supercapacitor.
DMU	diesel motive unit.
EMI	electromagnetic interference.
EMS	energy management system.
ESS	energy storage system.
FC	fuel cell.
FCB	fuel-cell/battery.
GHG	greenhouse gas.
HEV	hybrid electric vehicle.
ICE	internal combustion engine.
LRV	light rail vehicle.
NiCd	nickel-cadmium.
NiMH	nickel-metal hydride.
PEMFC	proton exchange membrane fuel cell.
PHP	power hybridization potential.
PID	proportional-integral-derivative.
PLATHEE	platform for energy-efficient and environmentally friendly hybrid trains.
PMDC	permanent magnet direct current.
PWM	pulse width modulation.
RTRI	railway technical research institute.
SC	supercapacitor.
SMPS	switch mode power supply.
SOC	state of Charge.

TTW	tank-to-wheel.
UDDS	urban dynamometer driving schedule.
WTW	well-to-wheel.

Acknowledgements

As a student of science, and an engineer early in his career, the people who aided, supported, and encouraged me during my pursuit of this degree have touched my life in a most substantial way. To those people, I say thank you.

First of all, I would like to extend my utmost gratitude to my supervisor, Dr. Loïc Markley, for his guidance and support over almost three years. His unwavering commitment to high quality research work, and meticulous attention to detail had significant impact on my work.

For my co-supervisor, Dr. Gordon Lovegrove, I extend a special thank you. After all, my journey at UBC began with the first lecture, Social Cost Benefit Analysis by Gordon Lovegrove. His enthusiasm about sustainable transportation inspired me personally. I would also like to thank Dr. Wilson Eberle, and Dr. Rudolf Seethaler for serving on my thesis defense committee and taking the time to read and comment on my thesis.

For all the long hours and days at the Sustainable Transport Safety Research Lab, it was my fellow students that kept me focused and motivated. In particular, I would like to thank my lab partner, Abdul Rahman Masoud, for the interesting political discussions which served as a nice break between hours of research work. I would also like to thank my friends and colleagues Adam Lee, and Esraa Jamal, and my wonderful TA, Bara Emran. Special thanks to Victoria You, who took the time to work on a 3D volumetric visualization of a hydrogen powered locomotive.

Finally, I thank all of the friends that supported and encouraged me during the course of this degree. To Nasser A. Alqahtani, Fawaz Altamimi, Mohamed Alhashimi, and Aziz Alghamdi I say thank you. You were my family in Canada.

To my mother.

Chapter 1

Introduction

Ever since the first steam engine, transportation by rail has enhanced our way of life by reducing the time traditionally required to transport goods by land and sea. A low coefficient of friction between steel wheels and steel rails enabled a very efficient transportation system. Railway propulsion technology has developed tremendously since the introduction of the first steam engine. The use of liquid fossil fuels in internal combustion engines enabled faster and more reliable operation. Very powerful trains that could haul hundreds of people and tonnes of goods were manufactured. Unaware of their impact on the environment, governments started competing in building an increasing number of complex and innovative railroad networks.

Noisy, pollutant emitting, and very hazardous, the diesel train did not survive for long. Its replacement, the diesel-electric train promised better traction, safer operation, higher efficiencies and reduced emissions. Unlike diesel trains that have a mechanical coupling between the diesel engine and the wheelsets, diesel-electric trains have an electromechanical coupling. While still having a diesel engine as the prime-mover, diesel-electric trains depended on electric motors for traction. Mechanical energy produced by the diesel engine is converted to electrical energy by an on-board generator (alternator), which is then converted to mechanical energy at the wheels by electric traction motors. This arrangement improved the overall reliability of trains, and drastically reduced the cost of maintenance.

The next big step in railway emission reduction was the full electrification of railroads. These new trains did not burn fossil fuels for power generation, and did not store energy on-board the train. Fully electrified railway systems were cleaner than diesel-electric trains , although if fossil fuels were used to generate the electricity that powers these trains, then fully electrified railway systems would not have been entirely clean. They were also quieter, faster, safer and much more reliable. Having a train directly connected to the electricity grid enabled it access to a practically unlimited power supply, and also improved its acceleration. However, the cost of complete electrification remained prohibitively high in a majority of cases [1].

Recent developments in energy storage system (ESS) technology prompted research in hybrid electric powertrains for railway vehicles [2–5]. Electrical ESS such as batteries and supercapacitors can be placed on-board locomotives or motive units, and are able to store braking energy that is otherwise lost as heat when using frictional brakes. Contrary to batteries, supercapacitors have a very high power density but a very low energy density. They are typically needed for two reasons: 1) to provide the needed power for high acceleration rates, and 2) to more efficiently absorb regenerated energy during braking.

Freight and passenger trains are very well suited to run on on-board ESS. This is because passenger trains utilize the electrification infrastructure of overhead catenary or under-running conductor rails, and freight trains are mostly diesel-electric that typically utilize electric motors for traction. According to the literature reviewed, electrical ESS have so far been used to reduce the overall energy consumption of fully electrified railways. Research on the viability of discontinuous electrification by employing ESS has so far been theoretical in the majority.

Fuel cells, or in particular proton exchange membrane fuel cells (PEMFCs), combine hydrogen and oxygen to produce electricity with water as waste. The technology has been around since the 1960s, but is only recently showing promise in transportation applications due to improvements in PEMFC research. Although PEMFCs have efficiencies of levels comparable to that of diesel engines, the high energy density of hydrogen as compared to diesel makes them a better choice. Since PEMFCs have no moving parts, they are also much quieter and more reliable than internal combustion engines (ICEs). That being said, due to their relatively slow dynamic response they must typically be aided by an auxiliary power source. Figure 1.1 presents the gravimetric and volumetric energy densities of supercapacitors (SCs), lithium-ion batteries, diesel fuel, and hydrogen gas compressed at 350 bar.

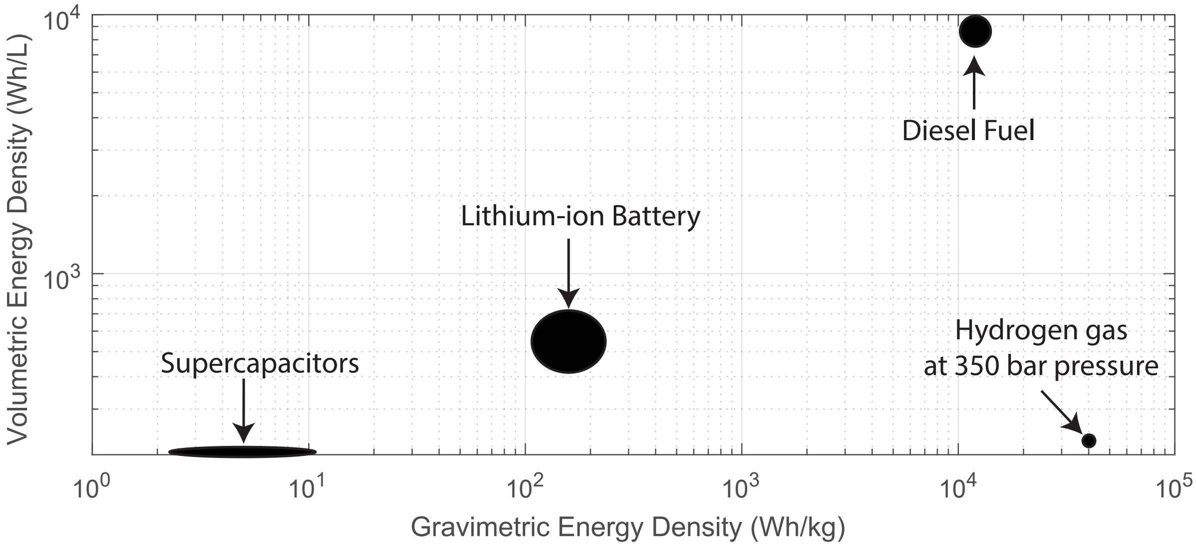

Figure 1.1: The gravimetric and volumetric energy densities of SC, lithium-ion batteries, diesel fuel, and hydrogen gas compressed at 350 bar.

A vehicle's duty cycle, or driving cycle, is the cycle of power demand along a specific journey. It depends on many factors, such as driver behavior (driving style), but it primarily depends on the route traveled. Factors like gradient profile (altitude fluctuations), track curves, and speed limits on certain sections of the tack are important for deciding whether a secondary power source is needed, and if so, how much it should contribute to the power mix. Studying a locomotive's duty cycle on a certain route as a precursor to designing a hybrid powertrain is a well documented practice in the literature [6, 7]. The energy required for propulsion during the discharge mode and the recoverable braking energy available for charging during the regeneration mode must be analyzed to decide on the type and size of the auxiliary power source [8].

Due to the high cost of building railway systems, a theoretical examination of railway duty cycles is required. The first step to generating a theoretical duty cycle is to computationally generate a trajectory profile. There are commercially available computational trajectory planning tools that accurately simulate train trips, but none have been developed for clean energy feasibility studies. Each of these tools has its own objective and motive behind its design, some optimize trip time and some optimize comfort. The work presented in this thesis explains the development of a Matlab / Simulink based powertrain simulator to conduct trip analysis and compare different clean propulsion technologies. It will be demonstrated that the developed simulator can be used in optimization, sensitivity, and feasibility studies. One particular feasibility study which is the topic of this thesis, is the technical feasibility of the different ESS sizing options on-board a moving railway vehicle or locomotive.

A hybrid powertrain is one where more than one type of power source is employed [9]. The inherent properties of power sources and the type of load influences the need for hybridization, the type of hybrid system, and the degree of hybridization. In particular, load dynamics and power source energy density are the main factors when it comes to decisions regarding hybridization. Typically, hybrid systems are employed as an attempt to optimize certain parameters including, for example : powertrain efficiency, range of travel, acceleration, regenerative braking, and emissions. Like any optimization problem, the optimization of hybrid ESS is subject to several physical and operational constraints. Physical constraints, such as mass and volume limits, are the only constraints considered in this study.

After defining gravimetric and volumetric constraints, a set of the most feasible hybridization options can be obtained through the simulation of different ESS combinations. Sizing scenarios that obey the physical constrains of the vehicle are chosen as discrete points. The results of the powertrain simulation of the chosen sizing scenarios can be then interpolated to produce functions of the hybridization mix. The more scenarios are simulated, the more accurate the interpolation process is, and the more computational power and time is required.

This project does not aim to focus on any one particular figure of merit, but to introduce a feasible range of scenarios that obey the physical and longitudinal train dynamics constraints. We do pay special attention to minimum component sizes that are required for continuous operation. It is up to the end user to decide on the hybridization mix that best suites their optimization goal.

1.1 Research Objectives

The main goal of this research was to compare different clean energy storage options for railway applications, to find an optimal mix of these options, and to comment on the viability of the proposed solutions as a part of a gateway technology in North America from diesel-electric to all-electric locomotives.

The objectives of the research presented in this thesis were to:

- Develop a train trajectory planning algorithm for velocity profile generation.
- Develop a battery/supercapacitor parallel hybrid powertrain model and use that model to simulate a number of railway duty cycles leading to optimization recommendations.
- Develop a fuel cell/battery series hybrid powertrain model and use that model to simulate a number of railway duty cycles leading to optimization recommendations.
- Simulate a number of trips on railroads of different characteristics in order to find a generalized answer as to the hybridization potential and the best candidates for hybridization.

1.2 Thesis Organization

The thesis is organized as follows:

- Chapter 2 includes a review of the literature as well as other background material that is relevant to the scope of this study.
- Chapter 3 explains the work done to develop a two-phase simulation process. The first phase solves the single-body longitudinal dynamics of the train to generate a target speed profile. The second phase simulates the actual powertrain.
- Chapter 4 presents the results of the conducted simulations, and the interpretation of these results. The chapter is devided into two sections, the first one dealing with a short 28 km round trip from Trehafod to Treherbert, and the second one dealing with a much longer 864 km round trip from London's King's Cross Station to Newcastle station.
- Chapter 5 is the final chapter and in it conclusions are made regarding the results of the simulated models. Recommendations on future research are also mentioned.

Chapter 2

Literature Review

2.1 Diesel-Electric Technology

Diesel-electric technology revolutionized the railway industry. Its replacement, the diesel-electric train promised better traction, safer operation, higher efficiencies, and reduced emissions. Unlike diesel trains that have a mechanical coupling between the diesel engine and the wheelsets, diesel-electric trains have an electromechanical coupling. While still having a diesel engine as the prime-mover, diesel-electric trains depended on electric motors for traction. Mechanical energy produced by the diesel engine is converted to electrical energy by an on-board generator (alternator), which is then converted to mechanical energy at the wheels by electric traction motors. This arrangement improved the overall reliability of trains, and drastically reduced the cost of maintenance.

Drivetrain Components A vehicle's powertrain is comprised of the components that are responsible for power delivery from the main power source to the road surface. In a hybrid electric vehicle, these components are:

- Prime Mover: This is typically a diesel engine in diesel-electric trains, and is responsible for transforming fuel to useful work as illustrated in Figure 2.1.
- Power Electronics Module: Before power electronics were available, traction motors were started by varying the resistance of resistor banks that were connected between the power source and the traction motors. This method, termed hard switching, was the only alternative to starting motors directly on-line (DOI).

  Power electronics are electronic switching devices that can handle high voltages and currents. The main job of the power electronics module is to change the type of electricity from the power source to suit the traction motors. This is established by either changing the voltage or the frequency of the electricity supplied to the traction motors. These modules allow for soft starting of the traction motors, and allow for a much bigger speed range.

- Propulsion Control: This is the system that controls the distribution of power in a railway vehicle. A system of "notches" control the power output of the diesel engine and are used to accelerate the train. Each notch corresponds to a fraction of the maximum available power. North American systems employ an eight notch system while in the UK a five notch system is used.

- Traction Motors: Motors convert electrical energy to mechanical energy. Traction motors in any land vehicle are used to convert electricity to motion, which is normally transmitted to the wheels through a transmission system.

- Braking System: Trains typically employ air actuated frictional brakes. A system of compressors, valves and pumps regulates the air that controls the braking effort of the train. Currently, newly built systems utilize electronic control of frictional brakes and are capable of regenerative braking.

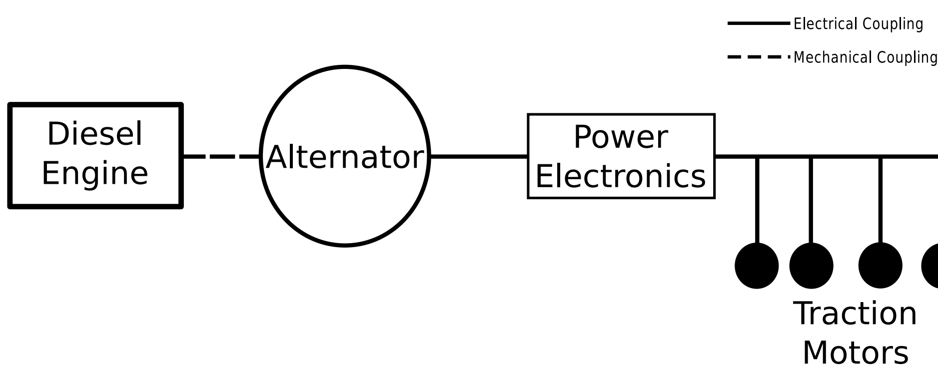

Figure 2.1: The main components of a diesel-electric powertrain.

2.2 Catenary-Electric Technology

The benefit of electrifying railway lines using catenary is that the prime mover no longer needs to be located on-board the locomotive. This allows any train operating on the line to access a practically unlimited power supply, and improves its acceleration. Electrified trains are also safer, as there is less risk of explosion in case of derailment since the train does not carry any combustible fuel. This comes at a price, however; the price to install continuous-feed electrification infrastructure can usually only be justified on busy routes. Figure 2.2 illustrates the operation of catenary-electric technology which is employed by most EU railway systems.

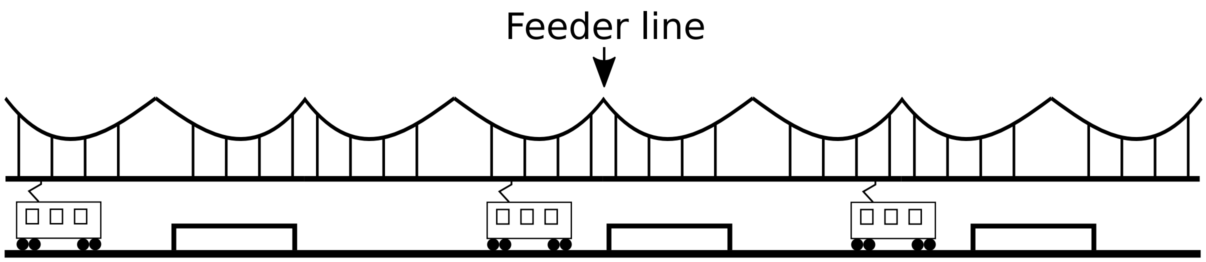

Figure 2.2: The operation of continuously electrified railroads.

Electrified overhead cables are usually single phase AC power drawn from the main three phase supplied by the local utility company. An electrified route will typically be divided into sections, each supplied from a different substation, and each fed from a different part of the utility network for increased security. Electricity is taken at very high voltage from the grid, transmitted in large cables to the substations, where the voltage is usually stepped down and then used to electrify a section of the track [10].

Single phase transformers inside the feeder stations aim to create a balanced load with respect to the other phases. Utility companies require balanced loads so as to ensure balanced currents and therefore good power quality. Having a train with power levels in the megawatts suddenly show up on a single phase line will inevitably create unbalanced currents within the three phase utility supply [11].

Electrifying an entire route is a complex process, partly due to the reasons mentioned earlier and partly due to other considerations such as safety, security, grounding and electromagnetic interference (EMI). Maintenance personnel who operate close to such high voltages are at constant risk of electric shock or electrocution. The measures required to ensure the safety of personnel add to the cost of any electrification project. Having very high currents in overhead cables or in the rails will create large magnetic fields which could interfere with electronic devices like pacemakers or other similarly sensitive equipment in the vicinity. There was also documented evidence that EMI causes corrosion in underground pipelines [12, 13].

Electrified routes also enable the use of dynamic (regenerative) braking, a mechanism by which a train's kinetic energy was transformed into electrical energy and is fed back through the overhead cables. The energy returned to the overhead cable can be used for driving other trains [2], or stored on-board the locomotive. If no storage system exists on-board the locomotives or in the substations, the energy returned can only be consumed if another train is nearby. This creates a need for regeneration and consumption to occur at the same time, otherwise the regenerated energy is wasted [2].

Electrifying over large distances requires conductor loss calculations to be taken into consideration [14]. The further an electric train is from the substation, the less voltage is available to it as there is a greater voltage drop across the conductor' s resistance. This requires all the power electronic and control systems to be designed to work for a range of voltages which further adds to the complexity of the system.

The current collection system, as the name suggests, is the system responsible for collecting the supply current and delivering it to the on-board electric traction motors. There are many accepted designs, but they all fall under two categories: overhead and track-level current collection systems. Generally, all overhead running systems utilize a current collector, otherwise known as a pantograph that establishes contact with the overhead current carrying cables [15]. There are many different configurations and arrangements of the overhead running cables, also known as catenary. These usually depend on the electrification system used, whether AC or DC, and on the level of voltage across the cables.

Track level electrification is very popular in metro systems that run in tunnels. It is much easier on the eyes than overhead electrification, but carries a significant safety risk factor. The current collector in track level electrification is typically called a conductor shoe, and it has the job of establishing contact with the third current carrying rail to close the circuit and allow current to reach the electric traction motors.

The powertrain of a fully electric train is the same as a diesel-electric train minus the diesel generator set. Electric trains will typically employ more sophisticated power electronics modules and energy management systems [16].

One of the best examples of the early success of electrification in North America is the Virginian Railway. Although it was a short, and a newer system at the time, the company operated one of the best engineered railroads in the United States. The Virginian Railroad hauled coal from South Appalachia, and competed with other companies in the region. It could only survive the competition because it was financed by the richest man at the time, Henry Rogers. The decision to electrify the Virginian Railroad came in 1922, and after three years, the electrification was complete [17]. It operated for 36 years until it was acquired by Norfolk & Western in 1959, and the electrification was shut down in 1961.

The Penn Central Transportation Company was another company that operated electrified railroads. It is famous for being the largest bankruptcy in US history at the time, when it went bankrupt in less than a decade from its inception [18]. One of the main reasons for this was the incredibly high cost of track maintenance, and the high salaries of the workers. Another example where electrification construction and maintenance costs proved too great to profitably operate is the Milwaukee Road Railway, which had capitalization problems that precluded its network from going completely all-electric [19]. Given these historic failures, electrifying freight rail in USA has remained only economically viable on short isolated routes connecting coal mines with power plants.

Recent developments in ESS technology has sparked a debate on the potential for reintroduction of electrified railways [20]. This would in turn reduce capital cost requirements, and encourage railway companies to reconsider all-electric locomotives and electrification.

2.3 Hybrid Energy Storage Technology

This section of the thesis discusses technologies that can replace fossil fuels in railway propulsion systems. While hybridizing with an ICE is an option that reduces a vehicle's emissions, it does not meet the objective of this research which is to eliminate all tank-to-wheel (TTW) emissions. TTW emissions, as opposed to well-to-wheel (WTW) emissions, are emissions at the point-of-use regardless of the power supply chain.

In this section, we will explore the state of the art in hybrid propulsion systems applied to railway vehicles. We will start with an introduction to ICE hybrids, otherwise known as " Green Goats". This will be followed by a discussion on discontinuous electrification, and then a review of the application of clean power sources as prime movers in railway vehicles.

Diesel-Electric Hybrids Green Goats are trains that employ a secondary power source, normally an electrical one. Batteries and SCs have been popular choices in diesel-electric hybrid projects [9, 21–23]. The main goal of hybridization with diesel powered vehicles is the optimization of the diesel engine efficiency. Diesel engines operate at their maximum efficiency when producing rated power, and at their lowest when idling. By reducing the size of the engine to have a rated power equal to the average trip power, we can guarantee that the engine will operate at its most efficient power levels and hence reduce particulate and greenhouse gas (GHG) emissions and energy waste. A secondary source is therefore needed to supply any excess power that cannot be delivered by the engine. The authors in [9] present a review of the different types of ESS that can be used in diesel hybrids, and the various diesel-hybrid powertrain architectures.

Green goat technology is pioneered by Railpower Technologies Corp, out of Vancouver, British Columbia and Erie, Pennsylvania. This technology however was only applied to switcher locomotives and not to mainline haul locomotives. Switchers spend about 60% to 80% of the time idling [21]. This means that the system is highly inefficient for most of the operating time which is the motivation behind the development of green goat technology.

Discontinuous Electrification Discontinuous electrification aims to reduce the cost of catenary technology, as well as extend the range of operation of any train, as a gateway or transition technology from diesel to full electrification or as a means to present a cheaper alternative to full electrification. On electrified sections, power provided by the overhead catenary is used to simultaneously propel the vehicle, and charge the on-board ESS. On non-electrified sections as presented in Figure 2.3, the ESS provides the power required for propulsion. The range of such trains could be further enhanced through the use of charging facilities that could be installed at stations along the non-electrified section. Employing ESS in railway systems increases the utilization of regenerated energy, reduces voltage drop across the conductors, reduces required electrification infrastructure and its maintenance, and reduces the visual impact of overhead cables and in-tunnel electrification. Depending on the capacity of the installed electric storage system, it may be possible to increase the regeneration braking force at the high-speed range as compared to full electrification [2].

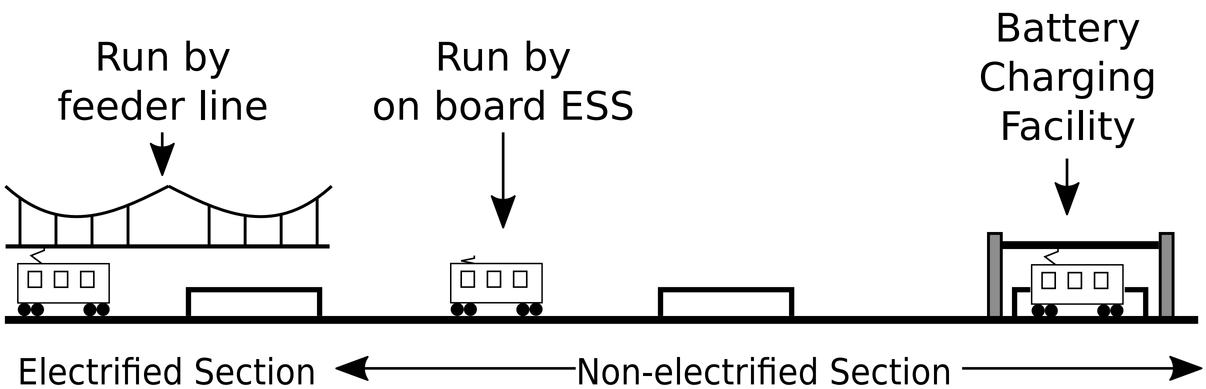

Figure 2.3: The operation of discontinuously electrified railroads [24].

A research project conducted at the Environmental Engineering Research Laboratory at East Japan Railway Company [3] studied a discontinuous electrification configuration. The project experimented with a typical 600 V line fed from a 1500 V DC electrified line through a DC/DC converter. The electricity fed the traction motors, ESS, and an auxiliary power supply unit to power a single railcar; no information was given about the route except that it was run in an urban area. The magnitude and direction of the current were controlled by a DC/DC converter by adjusting the output voltage. The setup relied on 672 lithium-ion battery cells, each operating at 3.6 V with a 30 Ah cell capacity. The cells were arranged in four parallel branches of 168 series-connected cells [2]. The total capacity of the battery bank was 72 kWh with the battery state of Charge (SOC) kept between 20%-95% in consideration of battery life.

Experimental vehicle operation modes:

- Non-electrified sections The battery system provides the entire power required, with the converter turned off. Dynamic braking generates electric power that supplies both the battery bank and the auxiliary power unit.

- Electrified sections The overhead catenary supplies electricity to the locomotive through the

> pantograph. This electricity is converted to the 600 V level by the DC/DC converter, which is then used to drive the traction motors. Depending on the SOC of the battery bank, some of the electricity supplied by the overhead catenary could also be used to charge the battery bank. Electricity regenerated from braking is used to charge the battery bank, or is supplied back to the overhead catenary for use elsewhere in the electricity grid depending on the battery SOC. This configuration also allows for powering assistance mode, in which the storage battery supplies electric power additional to the power provided by the catenary in order to overcome steeper grades.

In the same project it was shown that in power assistance mode, line voltage fluctuation was reduced which improved the overall power quality. Having a battery bank to supplement the power supplied by the catenary reduced fluctuations in the overhead voltage. Hybridizing with batteries reduced the stress on substations by reducing the peak power required. This eliminated the need for substation expansion to accommodate higher power requirements. Such setup has reportedly achieved over 30% energy saving in comparison to an inverter-fed regenerative tram [2]. Traveling at 40 km/h, the length of the non-electrified sections reached 25.8 km in total. The result showed that a 1000 A current could charge the on-board battery bank in about 60 seconds storing energy sufficient for 4 km or more [2]. This energy management strategy works best with power dense devices such as SCs but will have an adverse impact on the life time of batteries due to the high charging/discharging frequency.

Lithium-ion batteries are not the only option for on-board energy storage. Other options, such as SCs, have demonstrated good results when employed on rail vehicles. The Mitrac Energy Saver hybrid light rail vehicle (LRV) built by Bombardier in 2003 used SCs for energy storage and reportedly achieved up to 30% energy saving in comparison to other regenerative LRVs [14]. Similarly, the Sitras HES hybrid LRV built by Siemens in 2008 promised future energy savings of up to 30% [2].

Hydrogen Fuel Cell Technology A fuel cell locomotive is more efficient than a diesel-electric locomotive and has emissions at levels comparable to a catenary-electric locomotive. It has the low infrastructure cost of a diesel-electric, and the environmental benefits of a catenary-electric. Improved energy security of the rail transport system could be achieved by employing fuel cell technology in the rail industry. This would also reduce air and noise pollution, vibrations, and greenhouse gas (GHG) emissions, and has the possible added advantage of serving as mobile backup energy storage that could feed energy back to the electrical grid for critical infrastructure such as hospitals and military installations in emergencies [6].

Although there are many types of fuel cells, each one running on a different fuel, the most efficient is the PEMFC which runs on hydrogen. Hydrogen can be produced from many renewable energy sources, such as wind and solar energy, which directly translates to less dependence on fossil fuels. If hydrogen is produced from renewable energy sources, it would provide a zero-emission locomotive, when considering the entire energy cycle.

There are many different challenges facing the implementation of fuel cell technology in locomotives [25]. These challenges include: 1) the lack of hydrogen fuel infrastructure [25], 2) the safety of hydrogen fuel storage on-board a moving vehicle [26], and 3) the fact that diesel engines are still preferred due to their ability to accommodate transient load demands such as acceleration or hill climbing with a fairly constant efficiency range.

A few proof-of-concept fuel-cell rail projects have been completed in different parts of the world. The fuel cell mining locomotive developed by Vehicle Projects LLC during 1999-2002 [27] is considered as the first significant application of hydrogen fuel cells to a rail vehicle. During 2005-2007, the first fuel cell-battery hybrid switcher locomotive for urban and military-base rail applications [6] was developed by a North American project partnership among Vehicle Projects Inc., BNSF Railway Company, and the US Army Corps of Engineers.

Research into using hydrogen to power rail vehicles in Japan is spearheaded by two organizations, the railway technical research institute (RTRI), and East Japan Railway Company (JR East). The first tests were conducted by RTRI in 2001, reaching a significant milestone in 2003 when they succeeded in powering one bogie (wheel truck) using hydrogen fuel cells. In 2006, RTRI demonstrated a fully functioning hydrogen powered railcar. It was around the same time that JR East had transformed a diesel-hybrid railcar to operate using hydrogen, with test runs commencing in 2007 [6].

In France, the initiative for cleaner rail technology is headed by the platform for energy-efficient and environmentally friendly hybrid trains (PLATHEE) program [28]. In the UK, similar research is undertaken by the Birmingham Center for Railway Research and Education.

Researchers at the center have developed the UKs first hydrogen powered locomotive, the Hydrogen Pioneer [29]. Chinese researchers have also made efforts to integrate fuel cells into railway systems. The authors in [30] present the work done to build a fuel-cell powered shunting locomotive.

2.4 The Science of Hybridization

There are a number of factors to be considered when deciding on the need for hybridization of power sources for any application. The science of hybridization is essentially an assessment of supply and demand. The power demand profile must be analyzed to determine peak and mean values. The frequency of the power fluctuations, and a statistical description of multiple power demand profiles would greatly aid in decisions regarding hybridization. This section discussed the intrinsic properties of the three different power sources discussed in this thesis, presents an overview of active hybrid powertrain architectures, discusses the impact of duty cycles on power source sizing, and lists the different types of energy management systems (EMSs) present in the literature.

A) Power Sources

The inherent properties of power sources influence the need for hybridization, the type of hybrid system, and the degree of hybridization. There are three aspects to be considered with any power source: its energy density, its transient response (power density), and its control. This subsection presents an overview of the proposed power sources.

Batteries Batteries are a form of energy dense ESS which stores energy in an electrochemical form. Different chemistries come at different costs, energy densities, power densities and life expectancies. Nickel-cadmium (NiCd) batteries are the cheapest, but not the most environmentally friendly rechargeable battery chemistry on the market. Slightly more expensive chemistries such as nickel-metal hydride (NiMH) and lead-acid batteries were favored to NiCd for traction applications due to their enhanced energy densities.

The state of the art in battery technology are lithium-ion batteries. While being more expensive as compared to NiCd, NiMH and lead-acid batteries, they offer the highest energy densities of over 200 Wh/kg. Lithium-ion batteries have a high charge/discharge efficiencies of 80% to 90% due to the reduced internal resistance of each cell, with the disadvantage of having a short life cycle as compared to other battery chemistries. Lithium based batteries can be found in most electronic devices, ranging from cell phones and laptops to electric vehicles. Examples of electric vehicles that run on lithium-ion technology include: Tesla Roadster, Tesla Model S, Tesla Model X, Tesla Model 3, Nissan Leaf, and BMW i3.

To understand the behavior of any battery, we must first examine its discharge curve. Batteries lose voltage as their charge is depleted. Unlike SCs however, they do not do so in a linear fashion. Figure 2.4 presents the typical charge/discharge curve of a generic battery. The curve can be broken into three segments of interest that define how the battery voltage is related to its SOC: an exponential rise segment, a nominal segment, and an exponential decay segment. The authors in [31] briefly discuss the various computer models of lithium-ion batteries present in the literature. They also propose a generic Simulink based model that relies on a polarization voltage and is freely available in the SimPowerSystems library in Simulink, which was the model used in this study.

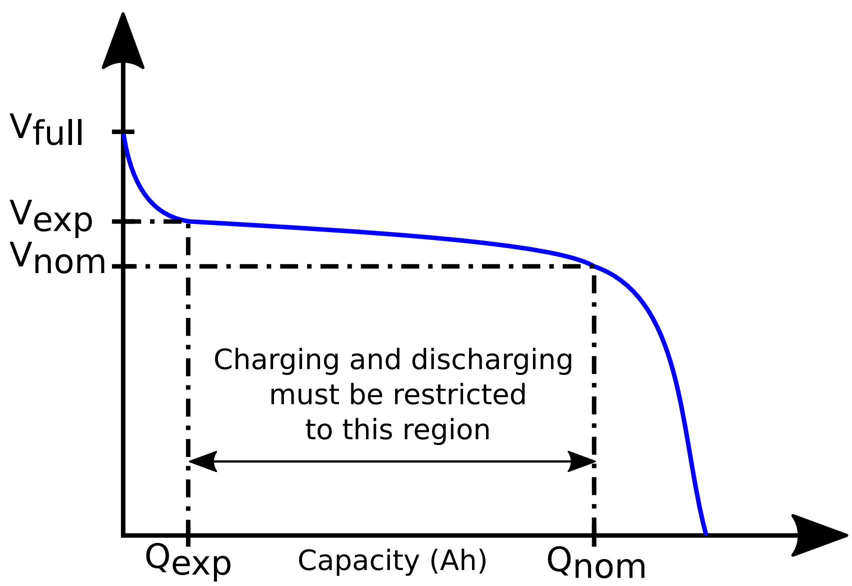

Figure 2.4: The charge/discharge curve of a typical battery relating the terminal voltage of the battery to its SOC [31]. Where Q_{nom} and Q_{exp} are the nominal battery charge and exponential battery charge respectively.

Batteries are not meant to be operated in either exponential region. In fact, operating in those regions adversely impacts battery life. Charge controllers or battery management systems are control circuits that aim to charge batteries while ensuring that they do not operate in the exponential regions. The battery chosen for this study is the *UPF454261* lithium-ion 3.7 V cell manufactured by Panasonic.

Supercapacitors Previously termed electric double-layer capacitors, these high-capacity capacitors are now called supercapacitors. Contrary to batteries which discharge at lower powers over longer time periods, supercapacitors have a very high power density but a very low energy density of typically less than 10 Wh/kg meaning that they discharge at higher powers over shorter time periods. In traction applications, they are typically employed for two reasons: 1) to provide the needed power for high acceleration rates, and 2) to absorb more of the regenerated energy during braking. Supercapacitors are rarely used as the sole power source in any application due to their drastically low energy density. The *BCAP3400* 3400 Farad SC manufactured by Maxwell Technologies is the SC of choice for all the simulations presented in this thesis.

Hydrogen Fuel Cells PEMFCs combine hydrogen and oxygen to generate electricity. Water and heat are the only waste products. Like an ICE, PEMFCs do not store energy, they merely convert it from one form to another at a certain efficiency. Hydrogen is an excellent energy carrier with a gravimetric energy density of approximately 40 kWh/kg when compressed at 700 bar, but a lower volumetric energy density of 1-2 kWh/L at the same pressure. PEMFCs are typically 50-60% efficient, which is lower than typical battery and supercapacitor efficiencies of over 95%, but this is balanced by the high energy density of hydrogen. The PEMFC model used in this study was freely available in Simulink as a part of the SimPowerSystems library and the details of its development can be found in [32].

The fuel cell (FC) stack chosen for this study is manufactured by Honda and commercially known as the *Honda FCX* family of experimental fuel cell stacks. Table A.3 contains the parameters of the 100 kW PEMFC model used in this study as obtained from [33]. While we do not aim to discuss the details of the theory of operation of a PEMFC, it is important to highlight a few key concepts:

- The FC fuel delivery system: Hydrogen and oxygen gas are the two inputs to the FC stack, and must be properly regulated to maintain the electrical output of the stack. Although the stack may be rated at a 100 kW maximum power, it can only deliver such power when the gas flow rates are adequate.

  Hydrogen is often stored as gas in pressurized vessels typically at 350 bar and 700 bar for traction applications. The stack itself operates at a 3 bar pressure , which necessitates the use of a decompresser and a flow rate controller. Oxygen on the other hand is not stored on-board the vehicle, but is obtained from the air and compressed to the required pressure levels. As a result, the hydrogen delivered to the stack is of purity levels up to 99.99% while the air is only 21% oxygen.

- FC dynamics: Several studies addressed the main challenges associated with implementing FC technology. In [34], the transient power required for acceleration, deceleration and start-up of a FC vehicle was obtained through simulation. The research team showed that the FC response exhibited a delay time as well as an undershoot/overshoot phenomenon when exposed to varying operating conditions as shown in Figure 2.5. In a FC vehicle, it is necessary to use a system of pumps and compressors to deliver oxygen at the required pressure. The dynamic response of the different subsystems responsible for oxygen delivery may cause oxygen (air) starvation during step load changes, otherwise know as mass transport loss. Several studies [35, 36] placed the maximum power density of PEMFCs at 18 kW/s.

  The issue of FC durability was investigated in [37], and the results showed that the transient power demand of the vehicle affected the FC lifespan and performance, which was adversely affected with frequent stops. Considering all these factors, it is concluded that FCs cannot be the sole energy source in an electric vehicle. Instead, they should be coupled with another energy storage device to share the transient load demand and improve the overall powertrain efficiency.

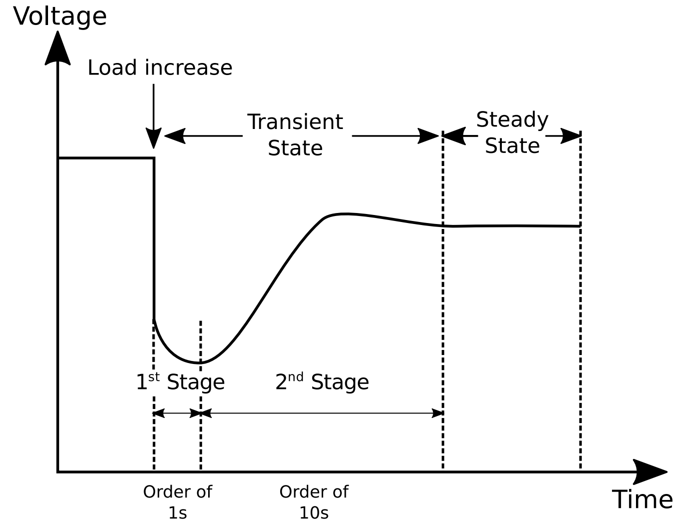

Figure 2.5: Voltage response of a FC stack during a positive step change in load [34].

Both batteries and SCs are viable options for hybridization with FCs for traction applications [38–40]. Unless there is a need for the superior dynamic response of SCs, batteries offer more advantages in FC series hybrids due to the higher energy density of batteries. The reason is that the terminal voltage of SCs fluctuates unlike that of batteries. It is important that the line voltage of the powertrain be kept constant to not affect the speed of the motor. If a SC bank is to be used as the secondary source in a FC hybrid powertrain, an active parallel architecture would be the better choice. This converter would regulate the SC bank's voltage to result in a relatively fixed DC bus voltage [38, 39].

- The polarization curve: Each electric power source has its own unique voltage-current relationship, just like each mechanical power source has its own unique speed-torque relationship. Just like lithium-ion batteries, FC systems have their own unique nonlinear voltage-current relationship which is often termed as the "polarization curve".

  It is important to keep in mind that the FC stack is most efficient when operating in the region between the rated power and the maximum power. In this case, between 85 kW and 100 kW. It is also important to notice from Figure 2.6 that the current drawn from the FC stack decides its terminal voltage and overall efficiency. Although not presented in the figure, in this particular example, if current of over 350 A is drawn, a sudden drop in voltage and thus power will occur. While there are sophisticated control techniques that reduce FC stack degradation [41, 42], maximize stack efficiency [43], and improve its dynamics response [44], the approach used in this thesis introduced an upper limit to the current demand from the stack to prevent a sudden drop in FC power .

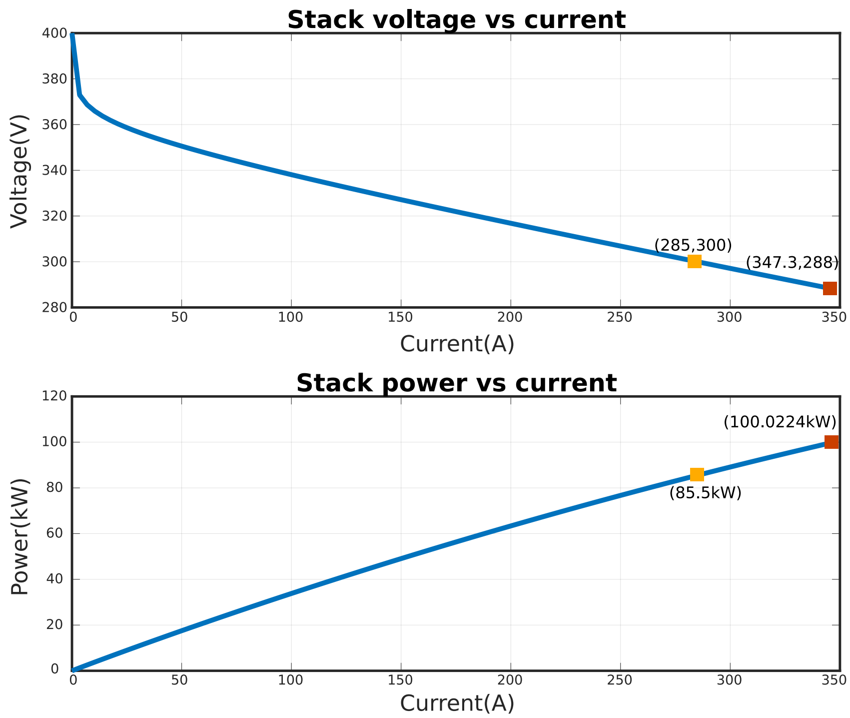

Figure 2.6: The polarization curve of the 100 kW PEMFC presented in [33] with its parameters detailed in the appendix as generated by the SimPowerSystems FC model developed by the authors in [32].

- The FC power conditioning system: To prevent overload and fault conditions, a current controlled boost converter to control the FC power output. Using this boost converter, we can ensure that the stack operates continuously and that changes in load (current demand) are rate limited. It is important to note that current ripple due to the switching behavior of the boost converter can reflect badly on the stack performance and cause its degradation. It is also important to mention that the response of the boost converter should not be faster than that of the FC stack. If the boost converter reacts much faster than the FC system, it will attempt to draw current which the FC cannot instantly supply and mass transport loss may occur. Details regarding the design, modeling and control of the boost converter will be covered in later chapters.

Hydrogen Storage Tanks Hydrogen can be stored in more than one form. Its gaseous form is most popular in traction applications [45]. Hydrogen gas is stored in pressurized vessels (tanks) typically at 350 bar and 700 bar pressures. The FC stack, which is tasked to combine hydrogen with oxygen gas to produce electricity, operates at approximately 3 bar pressure, which necessitates the use of a decompresser and a flow rate controller. Oxygen on the other hand is not stored on-board the vehicle, but is obtained from the atmospheric air and compressed to the required pressure levels. The hydrogen delivered to the stack is of purity levels up to 99.99% while the air is only 21% oxygen.

In this thesis, we assume that hydrogen is stored at a 350 bar pressure. A 350 bar Type IV hydrogen tank typically weighs around 100 kg, has a volume of approximately 300 L, and can store up to 5.6 kg of usable hydrogen [45]. The exact parameters used in the simulation are listed in Table 2.1.

Table 2.1: The specifications of the hydrogen tank.

Physical Specs	
Volume	316.4 L (380 L effective)
Mass	105 kg
Usable Hydrogen	5.6 kg

B) Active Hybrid Powertrain Architectures

There are several ways to categorize the types of hybridization architectures possible in all-electric hybrids that do not rely on an ICE. First they are categorized as either passive or active hybrids. A passive hybrid architecture does not employ a power electronic converter as an interface between the multiple power sources. Therefore, there is a loss of controllability of power flow which is often justified by the reduced powertrain cost. Active hybrids on the other hand employ power electronic converters to increase the degree of controllability of the power flow. Only active hybrids were considered in this study.

Active Series hybrid powertrains: In series hybrids, the power sources are connected in series with one source always feeding the other. The secondary power source located between the primary power source and the load, acts as a buffer and is typically employed to handle the dynamics of the power demand cycle. The main function of the primary power source is to provide base power demand, and to keep the secondary source charged. Figure Figure 2.7 shows an active series hybrid powertrain architecture. The figure illustrates how each power source is connected to a DC/DC converter. The DC/DC converter between the primary and secondary power sources serves to control the voltage/SOC of the secondary power source. In simple terms, it is like a tap that is turned off if the secondary power source is sufficiently charged, and is turned on when the secondary power source drops below required charge levels. This mode of operation is often called "charge sustaining control". The second DC/DC converter between the secondary source and the load controls the motor torque and speed. Both converters can be bidirectional if regenerative braking is required. If the primary source is a non-rechargeable device, like a fuel cell system, the first converter must be unidirectional.

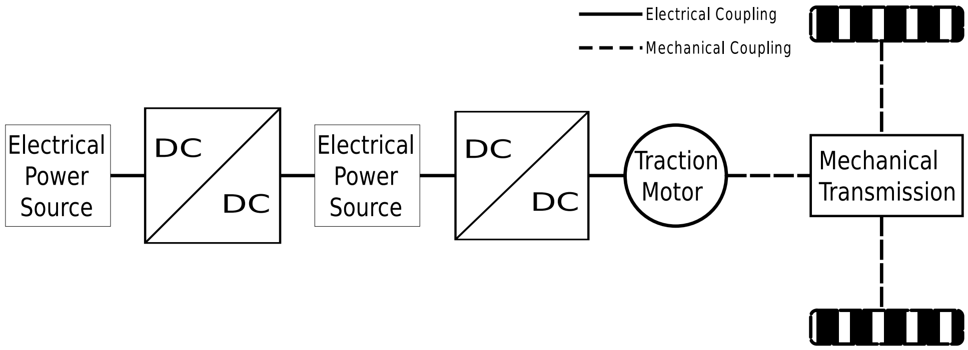

Figure 2.7: Active Series Hybrid Powertrain Architecture.

Active Parallel hybrid powertrains: Parallel hybrids utilize power sources connected in parallel to a DC bus of a fixed voltage controlled by DC/DC converters as shown in Figure 2.8. This setup allows more power flow controllability in either direction. Sophisticated control systems must be implemented to control how each power source reacts to load change and how much of the regenerated energy is fed into each source. Unlike series hybrids, neither of the power sources acts as a buffer. It is common to keep the DC bus voltage fixed and to use a third DC/DC converter to convert bus voltage according to the desired motor speed.

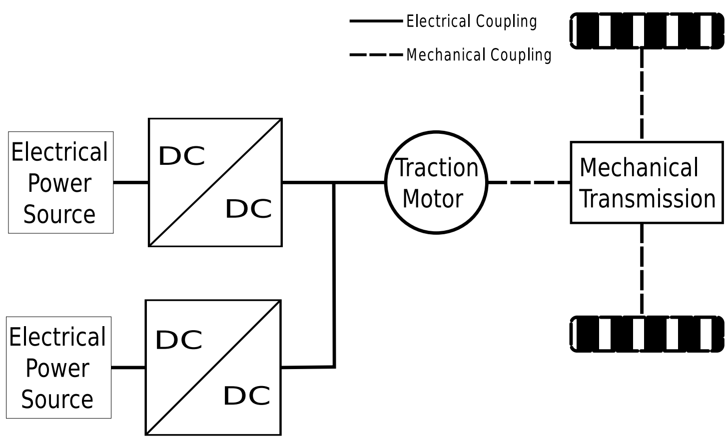

Figure 2.8: Active Parallel Hybrid Powertrain Architectures.

D) Duty Cycles and Energy Source Sizing

A vehicle's duty cycle, or driving cycle, is the cycle of power demand in a specific journey. It depends on many factors, such as driver behavior (driving style), but it primarily depends on the route traveled. Factors like gradient profile (altitude fluctuations), track curves, speed limits on certain sections of the tack, must be taken into account when deciding whether a secondary power source is needed, and if it is, how much of the power mix it should contribute. Studying a locomotives duty cycle on a certain route as a precursor to designing a hybrid power drive is well documented in the literature [6, 8, 22, 28]. The general procedure is to calculate the average power demand on a specific journey as a ratio of the peak power demand resulting in the power hybridization potential (PHP), which decides if a secondary power source is needed [46].

After examining the duty cycle of a locomotive on a certain route, and if the PHP indicates that a secondary power source is needed, a decision will have to be taken regarding the size of each of the power sources. For the selection of the type of auxiliary power source and the size of the auxiliary storage system for locomotives, the energy required for propulsion during the discharge mode and the recoverable braking energy available for charging during the regeneration mode must be analyzed on different duty cycles of the locomotive [22].

The authors of [28] report on two approaches to decide on the size of the power sources, namely:

1. Standard (Sequential) Design Methodology
    (a) Decide on the powertrain architecture
    (b) Size the system components
    (c) Design an optimal EMS
2. Frequency Design Methodology
    (a) Decide on the powertrain architecture
    (b) Design an optimal EMS
    (c) Size the system components accordingly

In [28], it is argued that the second methodology ensures that factors such as system cost and volume, battery stress, and atmospheric pollution are taken into account as the intrinsic characteristics of the power sources. In [22] a computer program was developed and used for battery analysis. It took into account the capacity of a battery at different charge rates for charging and discharging. Charge rates, or C-rates, are multiples of the rated battery capacity under which the battery should operate for one hour. For example, a 1 Ah (Ampere hour) 30 C battery could deliver one ampere of current at its rated voltage for one hour, and up to thirty times the rated amperage, or 30 A for two minutes.

E) Energy Management Systems

Energy management is needed for systems that allow bidirectional power flow. Systems with bidirectional power flow ability and more than one source of power require even more complex EMSs, each designed with a goal in mind, an optimization objective. Variables to be optimized include parameters such as: efficiency, cost, energy source life time, emissions, and overall system volume.

Energy management systems can be broadly classified into two categories, rule-based (heuristic) EMS and optimal EMS. Rule based EMS obey one or more predefined rules of operation. For example, a charge sustaining battery hybrid will likely be controlled by a heuristic EMS with the rule being that the battery bank's SOC be fixed to a certain value. The SOC of the battery bank at the beginning of a trip should not be different from the SOC at the end of the trip. Clearly this offers a direct, intuitive and easy to develop system. Although not an optimal approach in itself, rules for heuristic EMS will typically be chosen to optimize a certain parameter. For example, a charge sustaining vehicle may optimize battery lifetime by not allowing the battery to be overly depleted or overly charged.

State machine control is another rule-based control technique that is widely available in the literature. Although documented to suffer from unwanted oscillations or "chatter" [40] when operating at the threshold between two states, it is perhaps the easiest to simulate and implement. It was the EMS of choice in the fuel cell/battery/supercapacitor hybrid developed in [40]. Three states (modes) were implemented: a charge state, a discharge state and a recovery state. In the charge state, the main power source, the fuel cell in this case, supplied power to the load and the secondary sources. In the discharge state, when the load power was high, both the primary and secondary sources supplied power to the load. In the recovery state, the regenerative braking energy from the load was used to recharge the secondary sources.

Optimal EMSs can be classified into two categories: offline or global optimization and online or real-time optimization. Offline optimization methods rely on the prior knowledge of the driving cycle while online optimal EMS attempts to optimize parameters while the system is running and with no prior knowledge of the driving cycle. Dynamic programming [47–49], linear programming [50], genetic algorithm [7, 51–53] and game theory [54] are examples of offline optimization methods.

Researchers typically employ a two phase EMS design process, first by using an offline optimization method to optimize certain variables given prior knowledge of the driving cycle and then using an online optimization method to improve the results further. In [50] the researchers combined a two stage offline-online strategy in which linear programming algorithms were chosen for offline optimization with PID control for the online optimization. The same work was repeated using a dynamic programming algorithm in [47] for the offline optimization phase. The authors in [55] combined a dynamic programming offline optimization method with an online optimal control based on neural networks and reported a 66% improvement in battery life when compared to rule-based control applied to a battery/supercapacitor hybrid electric vehicle (HEV).

Optimal fuzzy logic is the term coined for control techniques that combine offline optimization methods with fuzzy logic online control. Fuzzy logic control is a heuristic control method that requires accurately defined membership functions. The offline optimization method is used to decide on the degree of hybridization and the fuzzy controller membership functions. The training sets provided by the offline optimization method replace the experimental calibration process that is often required for fuzzy logic control.

Multi-objective optimization using evolutionary algorithms is a rapidly evolving area of research [52]. It is often applied to standardized driving cycles for road vehicles, such as the urban dynamometer driving schedule (UDDS) which is a driving cycle that is developed by the US Environmental Protection Agency [56].

2.5 Summary

In this chapter, we presented a review of the literature on current propulsion systems employed in the railway sector. Diesel-electric technology was briefly introduced, followed by a discussion of railway electrification and catenary-electric technology. Regenerative braking, improved acceleration, and the elimination of emissions at the point of use were some of the advantages of electrification discussed. A brief overview of some of the challenges that arise in electrified railway systems was presented along with a brief overview of the history of electrification in North America.

The application of hybrid energy storage technology in railway systems was discussed. Discontinuous electrification and the application of hydrogen fuel cell technology were discussed in great detail. Before delving into the technical aspects of both technologies, we first presented a review of all the successful attempts to hybridize trains that were published in the literature.

Later in the chapter we discuss some of the technical aspects of clean hybrid technology. An overview of the intrinsic characteristics of lithium-ion batteries, supercapacitors, and hydrogen fuel cells was presented, which was followed by a discussion of hybrid powertrain architectures. The importance of a vehicle's duty cycle in sizing potential ob-board ESS was discussed, followed by a review of the possible EMS as found in the literature.

The following chapters discuss the work done to produce a computer model that simulates hybrid electric powertrains of railway vehicles. Matlab and Simulink were used to conduct such simulations. Although the goal of this research, stated broadly, is to assess the technical feasibility of the proposed on-board clean hybrid electric solutions for railway systems, including freight locomotives, due to restrictions regarding data availability, we could only simulate passenger railway vehicles. However, the conclusions drawn could also apply to freight railway vehicles.

Chapter 3

Methodology

3.1 Overview

The work presented in this thesis relied on a two-phase simulation process. The first phase is a trip simulation that guides the second phase as illustrated in Figure 3.1. This simulation is a high-level equation of motion solver which was developed using Matlab / Simulink as the computation platform. The simulator models the train as a single rigid body with a fixed mass and then solves the equation of motion of that mass. It takes inputs that describe the track infrastructure, and the vehicle constants and solves the resultant equation of motion to calculate the actual train speed, tractive effort required, power and energy demand. The control mechanism employed in the first phase relies on a simple two-state logic (on/off) which generates the velocity profile.

The second phase of the simulation is the detailed powertrain simulation phase. In this part of the simulation, detailed models of the prime mover, ESS, traction motors and power electronic converters are included in the simulation. Proportional-integral-derivative (PID) controllers in the second phase of the simulation attempt to force the vehicle to follow the velocity profile generated by the first phase of simulation.

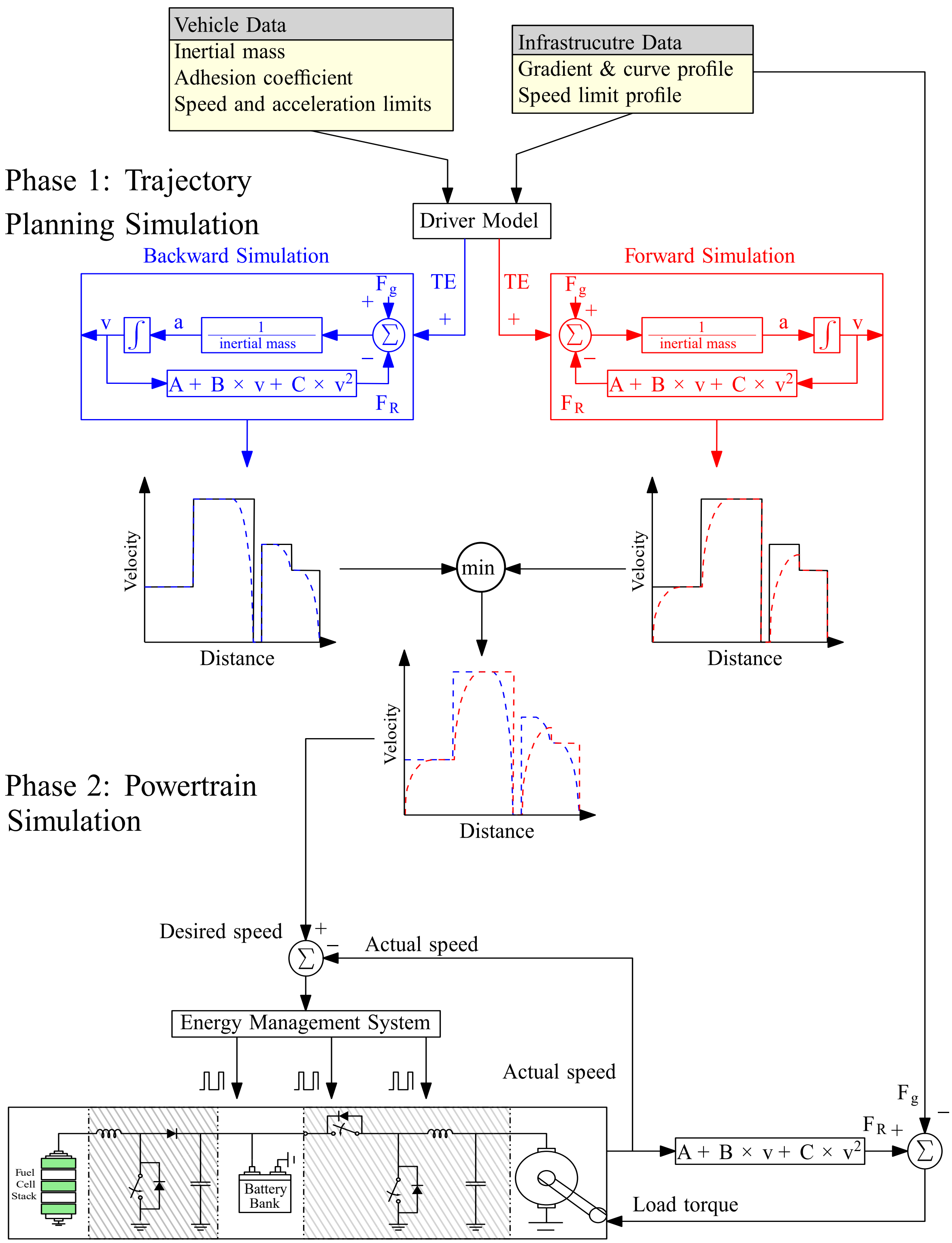

Figure 3.1: This flowchart illustrates the overall process used to conduct a hybrid powertrain simulation for a specific trip. The first phase of the simulation combines a forward and a backward velocity profiles producing a fast-as-possible velocity profile. The second phase of the simulation takes the resultant velocity profile as an input. F_g, and F_R refer to the gravitational force and the rolling resistance force respectively.

3.2 Longitudinal Dynamics of Trains

Longitudinal train dynamics are the subject of focus in analyzing train trips, and is defined as the motion due to forces acting on rolling stock in the track direction. It includes the motion of the whole train and any relative movements between the railcars. The first motivation behind the study of longitudinal train dynamics was the need to increase the level of comfort of passengers by reducing longitudinal forces in passenger trains. There was also interest in studying longitudinal train dynamics by the freight rail industry. Auto-coupler tensile failure and fatigue cracking was the primary motivation for research in this case. From this research an understanding of the different forces and their magnitudes and an awareness of the need to limit these forces with appropriate driving strategies was developed.

Longitudinal forces acting on a train can be divided into two general categories; steady forces and impact forces. Steady forces arise from the steady application of traction power or braking, as well as retardation forces such as wheel-rail friction, air resistance, curve and grade forces. It is common practice to lump curve and grade forces into one combined force termed *compensated grade*. Impact forces are due to changes in locomotive power and braking settings, and fluctuations in grade. The steady forces considered are the propulsion forces and the retardation forces combined. The propulsion force is the tractive effort that is dependent on the power of the prime mover, the speed of the train, and the efficiency of the system. The retardation force is the sum of the rolling resistance, air resistance and compensated grade.

The longitudinal force reaching the wheel-rail contact that is generated by the prime mover on-board the train is known as the tractive effort. To move in a given direction, the tractive effort must exceed any retardation forces such as wheel-rail friction, air resistance and elevation. The maximum tractive effort a locomotive can produce to propel a stationary train is the starting tractive effort (TE_{starting}). The starting tractive effort is a function of the locomotive's weight ($W_{\text{locomotive}}$) and the wheel-rail adhesion factor (μ) as given by Equation 3.1, and it is independent of the locomotive's horsepower and speed. The factor of adhesion depends on the material from which the wheels and the rail are made, which is typically 30% for steel wheels on steel rail. In this mode of operation, the locomotive's power increases as it gains speed.

$$TE_{\text{starting}} = \mu \times W_{\text{locomotive}} \tag{3.1}$$

The horsepower of the locomotive will keep on increasing as the train picks up speed, until it levels at the rated horsepower as presented in Figure 3.2. This region of operation is termed the *constant power* region, and in it the tractive effort drops as the train picks up speed. The relationship is defined by Equation 3.2. Where P stands for the power of the prime mover in watts, η stands for the efficiency of the system, V stands for velocity in m/s, $F_{\text{T}}(N)$ and $F_{\text{R}}(N)$ stand for the tractive force and retardation force respectively.

$$TE(N) = F_{\text{T}}(N) + F_{\text{R}}(N) = \frac{P(Watts) \times \eta}{V(m/s)} \tag{3.2}$$

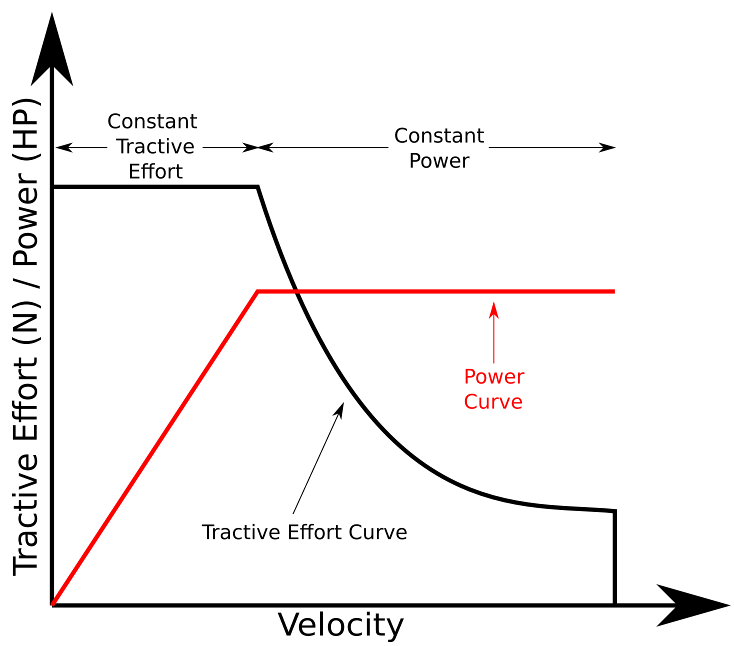

Figure 3.2: The relationship between a train's applied power, resultant tractive effort and its velocity

The retardation forces on a moving train are challenging to calculate, and are often approximated using experimental data. The resistance for train movement on straight and level track can be determined by the W. J. Davis formula in Equation 3.3:

$$F_{\mathrm{R}} = a + bV + cV^2 \tag{3.3}$$

- F_{R}= Train retardation force
- a = Rolling resistance component independent of train speed
- b & c = Drag coefficients based on the train's aerodynamics.
- V = Train velocity.

By inspecting the Davis equation we deduce that the resistance force increases with the speed of the train. Available tractive effort is typically not the controlling criteria for locomotives operating at low speeds. Adhesion must be large enough to overcome the train resistance, or else wheel spin will occur. As speed begins to increase, the available tractive effort also drops.

Gravity also plays a very significant role in a train's motion. Even the slightest elevations can have significant impact on a train's performance. This is mainly due to the large mass of railway vehicles. Trains that haul loads in the thousands of tonnes require a lot of horsepower to climb the slightest grades. For this reason, freight railroads in North America are generally limited to a grade of 2.5%. Typically, the train configuration used to pull a certain load across a certain track will depend on the horsepower-per-tonne factor of that particular track. Each track will have a ruling grade, which is the steepest grade along the entire track. Railroad engineers will normally calculate the amount of horsepower required to overcome the ruling grade for a certain load, the horsepower-per-tonne. A 1% grade will cause a 100 Newtons of downward force for each tonne.

Descending a grade safely is often a bigger challenge that ascending one. Due to the high mass of trains, even the slightest slope can lead to enormous longitudinal forces. The low steel-on-steel coefficient of adhesion which makes rail transportation such an efficient means of transport also makes it difficult to stop a moving train. Therefore it is of paramount importance to accurately calculate the expected levels of gravitational force that may act on a train on a certain track before deciding on the train composition. i.e the number of locomotives.

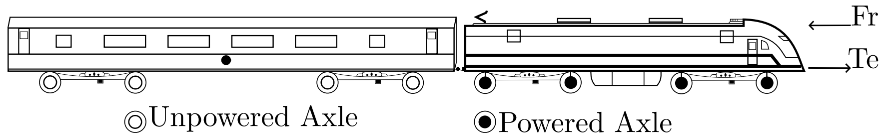

Figure 3.3: Forces acting on a train

A train's stationary mass is different from its effective mass (M_{eff}). This difference is due to the rotating machines on-board the train. A rotary allowance (RA) of about 5-15% increase in tare mass is typically assumed. The higher the number of motored axles in a locomotive, the higher the rotary allowance. This is due to the added kinetic energy of the rotating machinery inside the vehicle. Equation 3.4 shows how the effective mass is calculated given the rotary allowance.

$$M_{\text{eff}} = M_{\text{tare}} \times (1 + RA) + M_{\text{payload}} \tag{3.4}$$

Curve drag is another retardation force that should be considered. It is a function of the mass of the train, the radius of the curve and an experimentally determined constant. Often curve drag will not be explicitly mentioned, but is often combined with the gradient force to form a compensated grade force. Figure 3.3 illustrates the forces that determine a train's motion.

Tunnel resistance is a factor that is often accounted for when calculating retardation forces, but often not explicitly mentioned since tunnels cover a very small percentage of any given track. If the system under study is a metro system, tunnel resistance is continuous and is represented by the drag coefficients in the Davis equation, Equation 3.3.

3.3 Offline Trajectory Planning

The topic of this section deals with solving the equation of motion given certain constraints to generate a trajectory profile for the railway vehicle. In this section, we build on the principles governing a railway vehicle's motion as discussed in Section 3.2.

There are numerous software packages that compute velocity profiles for railway trips. Some are overly simplistic and do not account for train-wagon interactions, while some are very detailed accounting for the coupling between the railcars, the air-brake system dynamics, environmental conditions and their impact on adhesion, and many other factors [57]. These more detailed models are usually employed by railway operators and are licensed commercially. Simpler models often approximate the entire train as a single rigid body and can be used for research purposes [58].

Velocity profiles are determined from the route and train configuration and will typically be different under different optimization criteria. For example, the velocity profile generated using an algorithm for minimum trip time would typically not be the same as one developed for minimum energy consumption.

Route characteristics determine the maximum allowable speed at every section of the track. Using industry manuals on speed limits, which usually depend on track curvature and grade, a maximum allowable velocity profile can be generated. A railway vehicle's limited acceleration rates introduce additional speed constraints that are further limited by recommended acceleration/deceleration rates for safe and comfortable operation.

The control input in such a system is the engine power, which generates the tractive effort at the wheels. A train can operate in one of three modes, as illustrated in Figure 3.4: in powering mode where the tractive effort is positive, in coasting mode with zero tractive effort, or in braking mode when the tractive effort is negative (otherwise known as *braking effort*). The overall driving strategy or optimization target guides the algorithm developed to alternate between the possible modes of operation. To minimize trip time, a two mode operating scheme is employed, disregarding the option for coasting.

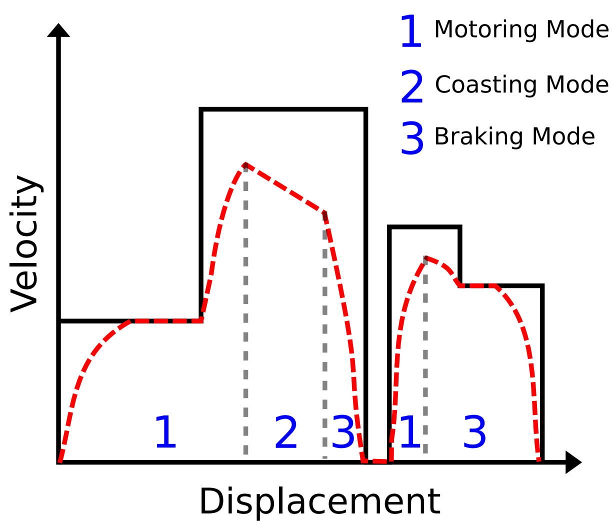

Figure 3.4: Railway vehicle trajectory profile, and the maximum allowable velocity profile are shown. The figure illustrates the three possible modes of operation.

Online trajectory planning is unnecessary in railway applications where the route is predefined. Online trajectory planning techniques are often complex to design, simulate and implement. They are usually employed in robotics applications. Offline trajectory planning techniques produce very good results without the extra computational power, time and cost that online techniques require. Figure 3.5 presents a more detailed illustration of the algorithm used to obtain the velocity profile in all the case studies presented in this thesis. The algorithm takes vehicle data and infrastructure data as inputs. Information about the railway vehicle such as its Davis equation coefficients (Equation 3.3), inertial mass, adhesion coefficient, speed and acceleration limits are some of the inputs to the algorithm. Other inputs relating to the infrastructure of the route such as its elevation profile, curve profile and speed limits on each section of the route make up the rest of the inputs to the algorithm. A forward and a backward velocity profiles are generated and the minimum of the two profiles makes up the demand velocity profile as shown in Figure 3.5.

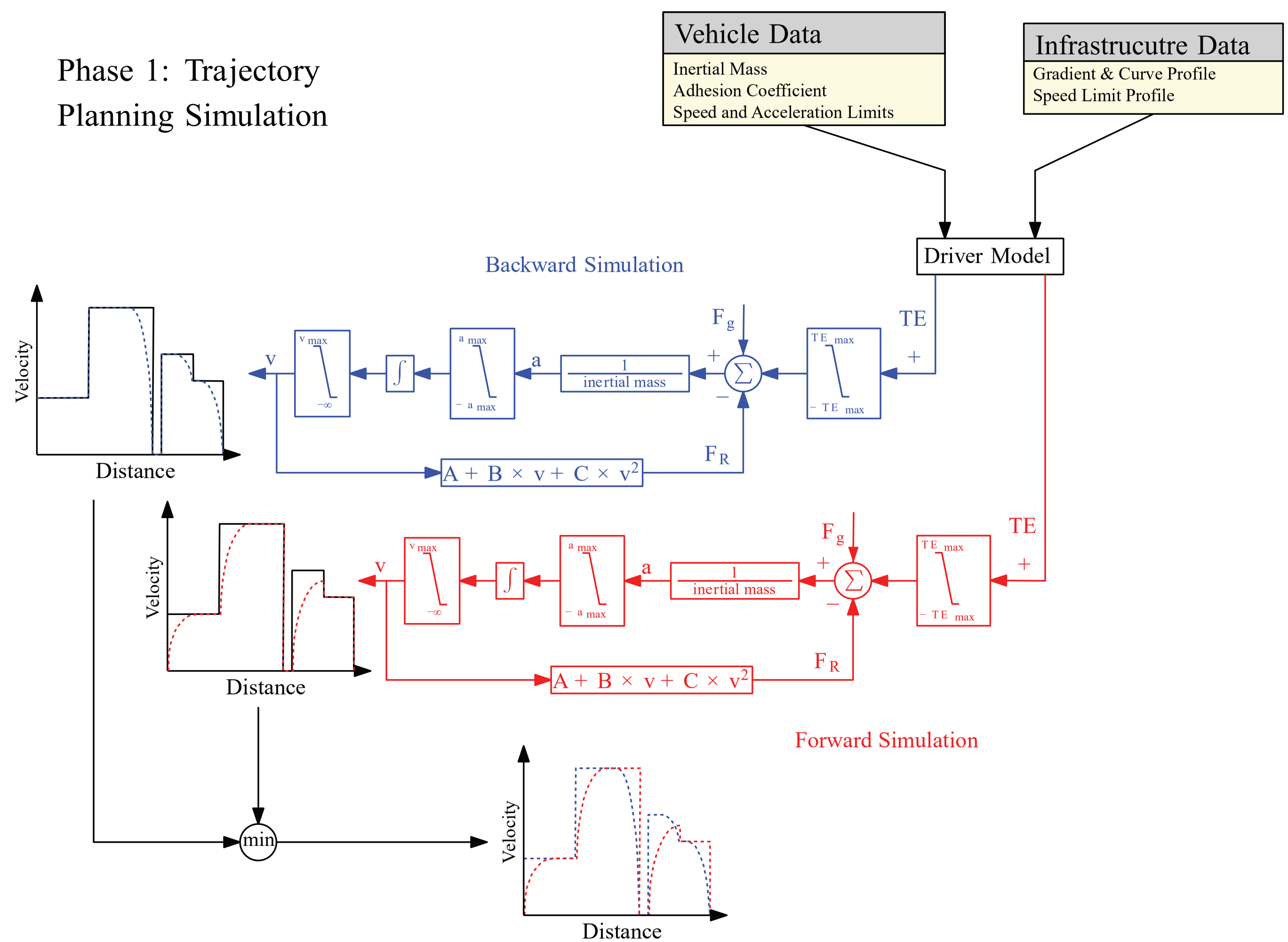

Figure 3.5: This flowchart outlines the trajectory planning algorithm used in the first phase of simulations in this study.

3.3.1 Preprocessing Gradient Data

Gradient or elevation data is typically given in discrete steps, which raises the need for interpolation of the data. The higher the resolution of the data points, the more accurate the interpolation is. However, it is not out of the ordinary for an elevation dataset to contain points spaced a few kilometers apart. The straight forward answer to this problem is to linearly interpolate the given dataset. However, pure linear interpolation produces sudden changes between the different linear segments which is unrealistic and poses a challenge for the PID controllers in charge of vehicle speed control, for these reasons a smoother interpolation method is needed.

As a solution, Matlab was used to interpolate the gradient profile data points. The first step of the interpolation is to increase the resolution of the data points by generating additional linearly spaced data points. A trade off exists when deciding on the spacing of the data points. The closer the data points, the better the fit, the more computation time is needed, and the bigger the file size. Data points of 20 meters spacing were generated via Matlab. The next step was to use a spline interpolation technique using the newly generated dataset. Figure 3.6 illustrates the preprocessing procedure adopted to result in a gradient profile that could work with Simulink. The result in Figure 3.6(c), is a gradient profile that is linear for the most part, but that has no abrupt changes, which is similar to real world scenarios.

It is a given than any attempt to produce a fit line will come at the cost of loss of accuracy as illustrated by Figure 3.6(c). Figure 3.6 presents a section of the Trehafod to Treherbert trip. Although we can observe that in the first 2 km the fit line is not passing through all the discrete points, this error is acceptable given that the R-square factor was calculated by Matlab to be 0.9986, and the Root Mean Square Error to be 0.3603 meters.

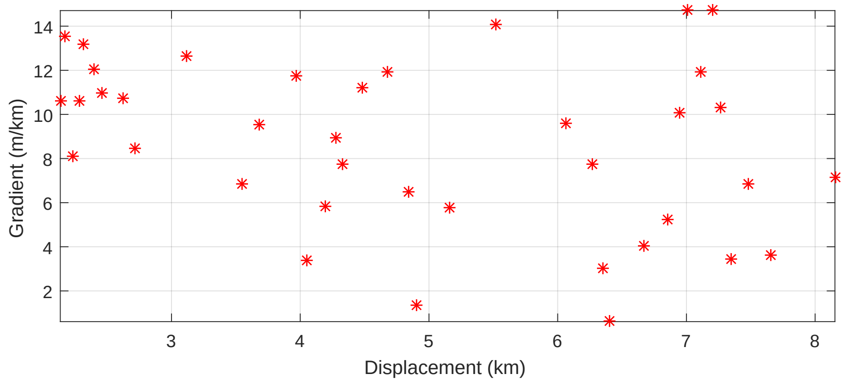

(a) Discrete gradient data points.

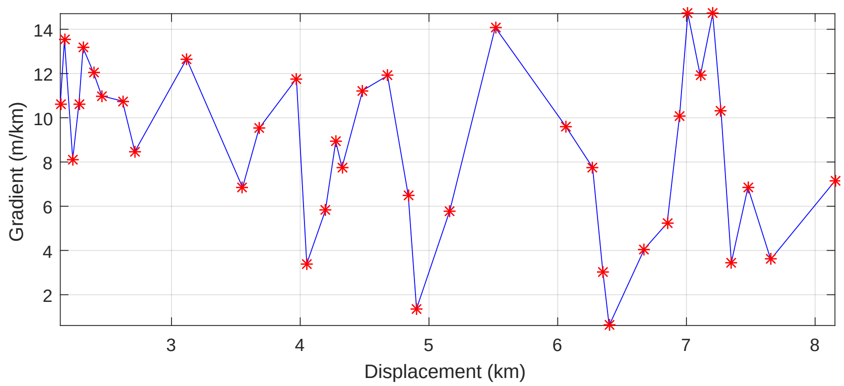

(b) Linearly interpolated gradient profile.

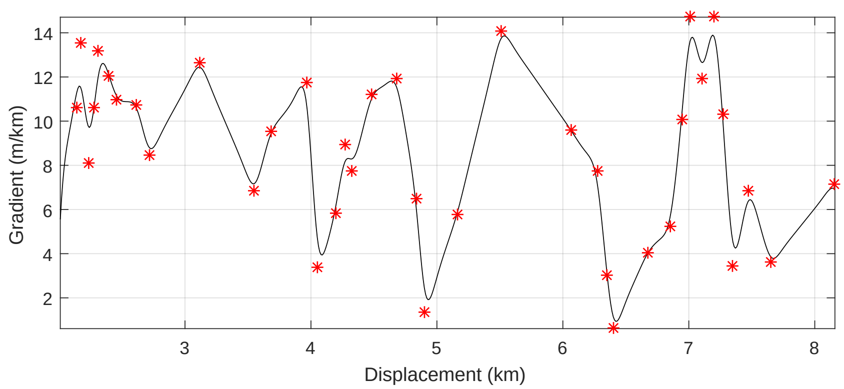

(c) Spline interpolation of the linearly interpolated gradient profile.

Figure 3.6: This figure illustrates the necessary preprocessing steps for the discrete gradient data points to be usable in Simulink.

3.4 Powertrain Simulation

Switch mode power supply (SMPS) systems, otherwise known as Power Electronic Converters, convert electrical power using semiconductor switching devices. Electrified transport heavily employs medium to high power SMPS systems for power conditioning purposes. Electronic semiconductor switching devices capable of handling high current magnitudes and voltage stresses enable the efficient and fast conversion of electric power.

In railway electrification, SMPS systems are often found on-board the motive unit or locomotive as well as inside the electrical substations that handle voltage step down from high voltage transmission to low voltage at the point of use. Depending on the electrification infrastructure, SMPS systems will convert DC to AC, AC to DC, DC to DC and AC to AC. This is achieved by altering the frequency and magnitude of the supply voltage.

All the power sources considered in this study are DC sources. This means that only DC to DC (DC/DC) SMPS will be considered. The simplest DC/DC converters are the buck converter and the boost converter. The buck converter steps down the voltage at its input to a lower voltage at its output. The boost converter does the opposite. In fact, since the design, modeling and control of SMPS is not the topic of this thesis, all the power electronic models used in this study will be ideal and lossless with large inductors and capacitors for low frequency simulation. This does not impact the overall result of the simulations since the dynamics of railway systems are inherently much slower than the dynamics of power electronic converters. SMPS systems are very efficient with efficiency levels in the range of 91%-95%. Therefore, assuming ideal converters does not greatly impact the simulation results.

Although electrical isolation of source and load through the use of transformers is common practice for safety and protection, it has negligible impact on power ratings and efficiency, and therefore all the converters considered in this study are non-isolated. That is because isolation is a matter of practical importance which is not the focus in this study.

There are two types of hybrid powertrains considered in this study, a fuel-cell/battery (FCB) series hybrid and a battery/supercapacitor (BSC) parallel hybrid. Some parameters were kept constant throughout the design of both systems so as not to bias the results and conclusions. The same permanent magnet direct current (PMDC) machine was used as a traction motor in all simulated case studies. The speed of the traction motors in a railway vehicle, and by extension the entire vehicle's speed, is a function of the voltage applied to the terminals of the traction motor. In essence, speed control is equivalent to voltage control. The option exists to use a lower voltage power source and a boost converter to give higher voltages at the motor terminals in order for the motor to be able to reach desired high speeds. However, since a boost converter only steps up voltage from the input side to the output side, it would be impossible to operate the motor at lower speeds that require voltages at the output of the converter that are lower than the voltage of the power source connected to its input. This would call for the use of a buck converter to supplement the boost converter, and a control mechanism to switch between the two converters depending on the desired speed. Given that the simulated powertrain must have bidirectional power flow ability, and if each direction requires a buck and a boost converter, a total of four converters per power source would be needed. For a dual power source hybrid vehicle, eight converters would be required.

As a solution, it was decided to use a higher voltage source and to step-down the voltage using a buck converter to a lower voltage at the output terminal connected to the traction machine. In motoring mode, when power flows from the ESS to the traction machine, voltage is stepped down through a buck converter and stepped up through a boost converter when the direction of power flow is reversed during regeneration mode. All the models operated at a 1500 V DC bus voltage which covered the entire speed range of the traction machine.

A fixed gear ratio of 3:1 was kept constant in all simulations, with the faster gear connected to the traction motor and the slower gear to the wheelset. All references to "battery" in this study refer to lithium-ion batteries only as they are the only battery chemistry considered since they are the most energy dense and the most suitable for traction applications.

Figure 3.7 is a graphical representation of the main steps taken to design, model and control a power electronic converter using Matlab and Simulink. The figure only highlights the general procedure with more details on the specific control of each converter to be presented in the following sections. The first step is the open loop design and simulation. In this step, circuit components are sized according to the converter's governing equations and open loop specifications. After the components are sized, the converter is then modeled and simulated in the Simulink environment using the SimPowerSystems library. Before proceeding to the next step, it is important to verify that the stead-state currents and voltages of the simulated converter match their corresponding theoretical values.

The second and third steps deal with system identification and linear approximation. SMPS are highly nonlinear systems and therefore challenging to model and control. All the models produced in this section were generated computationally and not analytically. While there are established large signal and small signal models for buck and boost converters, numerical methods provide faster and more reliable results. Matlab's Parallel Computing Toolbox was used in combination with Simulink's System Identification Toolbox to produce second order linear approximations of the proposed converters. The general procedure performed by Matlab and Simulink involves subjecting the open loop converter to an array of test control signals and storing the output, be it voltage or current. The software then attempts to create a linear second order transfer function that relates the test input signal to the output. For example, if we wish to control the output voltage of a buck converter, the control signal is the converter's duty cycle and the system output is the output voltage.

The last step in the closed loop control of a SMPS converter is finding the control parameters. PID control is simple, straightforward and easy to simulate. Finding PID parameters can be a tedious process, especially with an approximated system. PID controllers were then synthesized using Simulink's PID tuning ability. This greatly reduced the time normally required to tune PID controllers. It was discovered that the simulation results were less sensitive to changes in the power electronic converters if the PID controller had a very tight error tolerance.

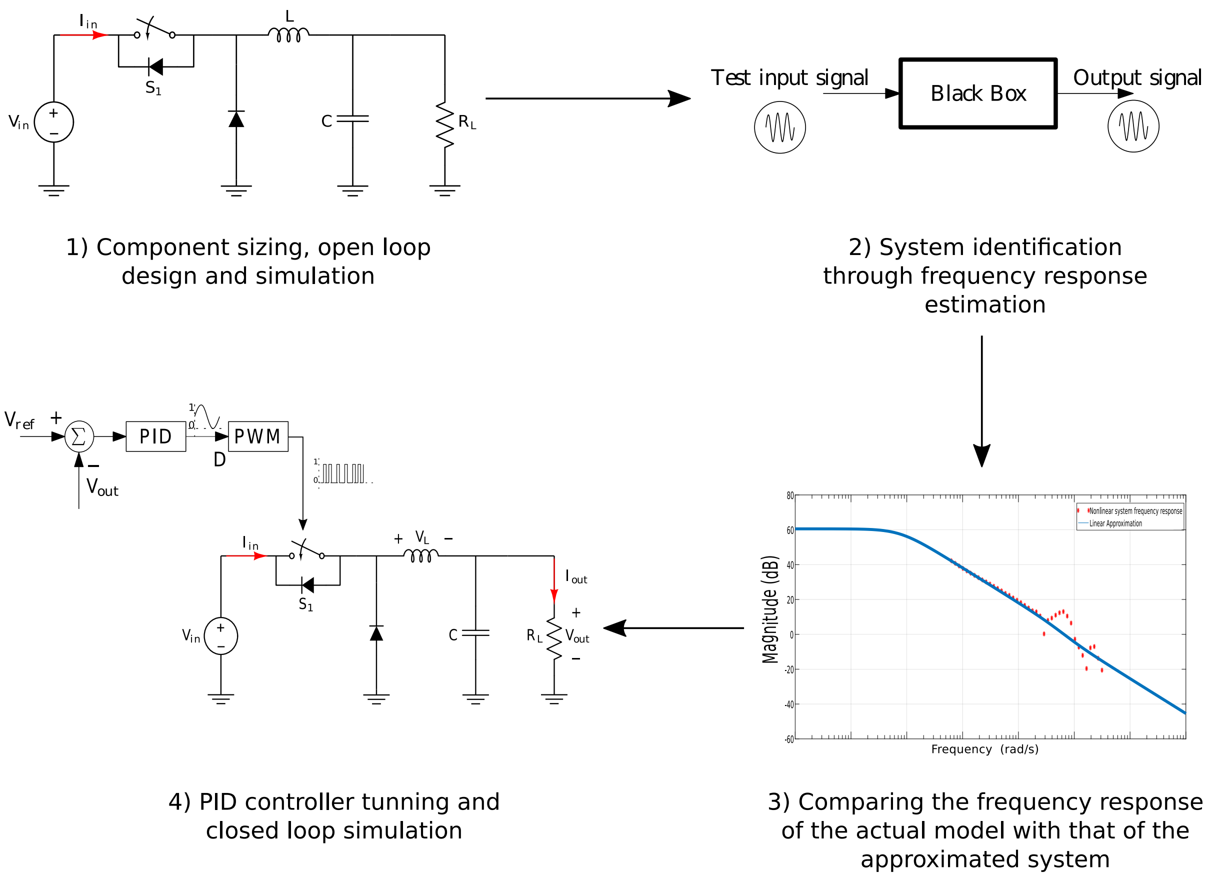

Figure 3.7: The steps required to design, model and control a simulated power electronic converter model in SimPowerSystems.

3.4.1 Buck Converter

A buck converter is a DC to DC converter which steps down the input voltage and steps up the input current. It is used to interface a high voltage source with a lower voltage load. The converter used in this study is an ideal converter with a single ideal switch, ideal diodes and ideal inductor and capacitor. The circuit layout is presented in Figure 3.8.

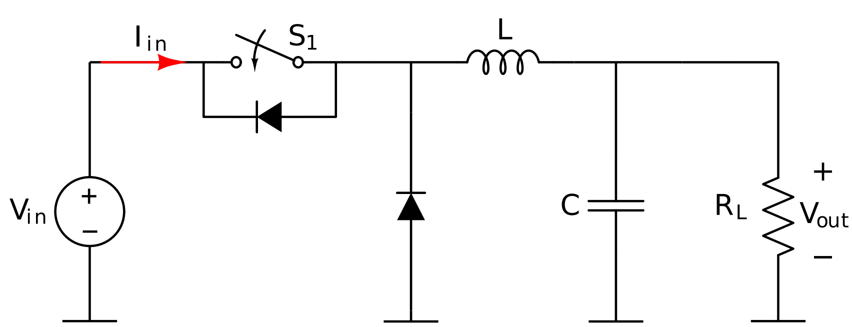

Figure 3.8: Circuit layout of a non-isolated buck converter with a purely resistive load.

Open-loop design and simulation Buck converters cover a limited range of output voltages. The value of the output voltage, V_{out}, depends on the switching duty cycle, D, and is governed by Equation 3.5. A switching duty cycle is defined as the ratio of the time during which a semiconductor switch in a power electronic circuit is turned ON to the time it is turned OFF. Given Ohm's Law, the output current, I_{out} can be found using Equation 3.6.

$$V_{out} = DV_{in} \tag{3.5}$$

$$I_{out} = I_L = \frac{V_{out}}{R} \tag{3.6}$$

For component sizing purposes, an operating point has to be carefully chosen to ensure proper operation over a wide range of duty cycles. Figure 3.9 shows the output voltage, V_{out}, as a function of switching duty cycle as governed by Equation 3.5.

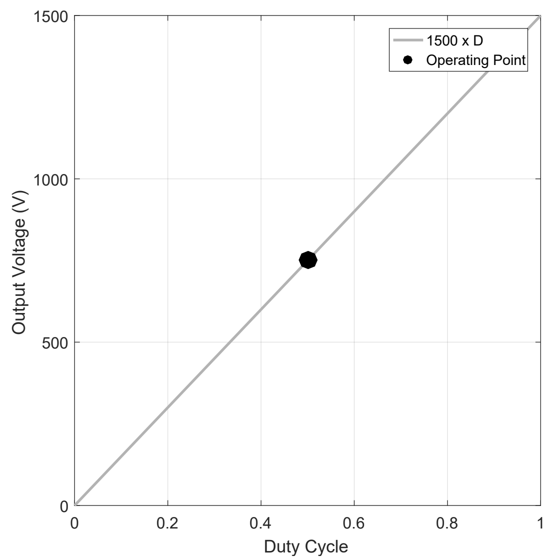

Figure 3.9: Output voltage as a function of switching duty cycle for a buck converter with an input voltage of 1500 V.

In all the simulations presented in this study, buck converters are used only during motoring modes to deliver power from the source to the load. The source voltage was kept at 1500 V in all of the simulations and is then stepped down to lower voltages depending on the desired motor speed.

The next step in the converter design is to size the inductor and capacitor. Both the output voltage ripple, Δv_{out}, and the input current ripple, Δi_{in}, are inversely proportional to the switching frequency f_s as suggested by Equation 3.7 and Equation 3.8 respectively. The output voltage ripple Δv_{out} is also inversely proportional to the output capacitor size C while the output current ripple Δi_{out} is inversely proportional to the inductor size L.

$$\Delta v_{out} = \frac{V_{out}(1-D)}{8LCf_s^2} \tag{3.7}$$

$$\Delta i_{out} = \Delta i_L = \frac{V_{out}(V_{in}-V_{out})}{V_{in}Lf_s} \tag{3.8}$$

This suggests a trade off between element sizes and switching frequency for any given ripple value. For example, a higher switching frequency f_s and a small inductor L will give the same ripple amount as a lower switching frequency f_s and a bigger inductor L, as governed by Equation 3.8. The same trade-off exists between the output voltage ripple, capacitor size and switching frequency f_s.

Parameters used in the simulation are included in Table 3.1, and the open loop output voltage is presented in Figure 3.10. Figure 3.10 shows that the open loop output voltage has a steady state value of 750 V as governed by Equation 3.5. It also shows that the open loop settling time of the output voltage is around 1 second, with a ripple component of 1 V as governed by Equation 3.7 and calculated in Table 3.1.

Table 3.1: Buck converter specifications.

V_{in}	1500	V
V_{out}	750	V
D	50%	
R	1	Ω
I_{out}	750	A
f_s	1000	Hz
Δv_{out}	1	V
L	0.1143	H
C	0.2286	F

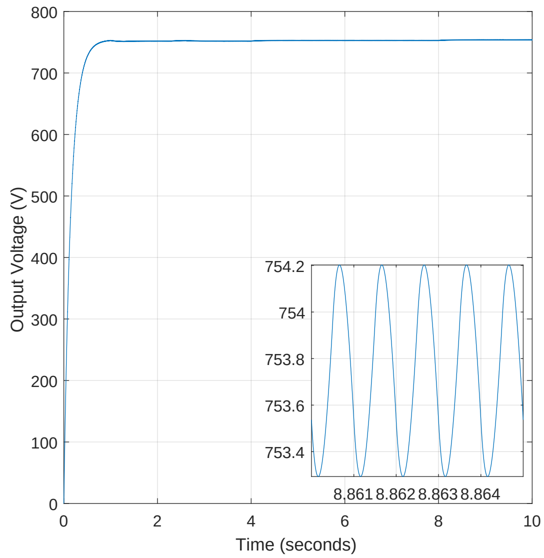

Figure 3.10: Open-loop output voltage V_{out} at the operating point shown in Figure 3.9 with a ripple amount Δv_{out} of 1 V. The inset plot highlights the ripple component.

In practice, the aim is to reduce component sizes and thus reduce cost by operating at a higher switching frequency f_s. For simulation purposes, however, higher switching frequencies translate to longer computation time. The Simulink model would have to run at least twice the switching frequency (Nyquist Frequency) to prevent undersampling and signal distortion. This is both computationally, and memory intensive. Therefore a low switching frequency of 1000 Hz was selected.

It is important to take note of two facts, the first is that if the inductor size is too small, the converter will enter a discontinuous conduction mode which produces undesirable results and further complicates the control problem. Discontinuous conduction mode is when the inductor current is held at zero for any portion of the sampling time. The critical inductance value at the boundary between continuous conduction mode and discontinuous conduction mode is L_{crit} and is governed by Equation 3.9. The second is that if the inductor and capacitor sizes are too large, they may store significant energy and distort the results of the simulation. This suggests a trade off, and that a tuning procedure has to be adopted.

$$L_{crit} = \frac{(1-D)R}{2f_s} \tag{3.9}$$

Linearized system identification The rotational speed of any electrical motor is a function of the voltage supply. A closed loop control system can be used to adjust the converter's output voltage depending on the desired speed of the electrical motor connected to the output of the buck converter. Classical linear control can only be used to control power electronic converters if the range of operation is bounded to a region where linear approximations of the nonlinear model can be made. By examining Figure 3.9, we can see that higher duty cycle values result in a linear rise in output voltage which simplifies the process of synthesizing a controller for this converter. An operating point at a 50% duty cycle was selected as shown in Figure 3.9. At this operating point, the output voltage V_{out} is 750 V.

Closed loop control of power electronic converters has been an active research topic ever since their inception. Classical linear control techniques produce reasonable results and are much easier to implement when compared to more sophisticated nonlinear control techniques. PID control is the industry standard for all non-sensitive applications. A PID controller acts on the error between a desired signal (input signal) and the actual signal (output signal) which is usually obtained through sensors. It aims to minimize this error to produce an output that matches the input. It does so by applying three control parameters to said error signal. These three control parameters are: the proportional parameter (P), the integral parameter (I), and the derivative parameter (D), hence the controller is termed PID. The proportional parameter acts on the current values of the error signal, while the integral parameter acts on the error history, and the derivative parameter on the future possible values for error.

For the purposes of this study, a simple PID controller was synthesized and found to produce accurate results over a wide range of output and input. The procedure as highlighted in Figure 3.7 treats the plant (system to be controlled) as a black box, and formulates a linear approximation depending on the test inputs and the corresponding outputs.

This process requires iteration with different test input signals, different in magnitude and in frequency. Each time a linear model is found, it is validated through simulation until an acceptable approximation is found. An acceptable approximation is one where the approximated system captures the dynamics of the actual system within 20% error margin. The buck converter used in this study is a second order system, and therefore it is best to approximate it with a second order linear system.

Figure 3.11 shows the bode plot of the buck converter and its linear equivalent model. While the approximated response is not an identical fit to the actual response, the results are acceptable given that the "goodness of fit" factor, a factor that determines how closely the approximated system matches the actual system, as calculated by Matlab was 97.17% [1]. This is also demonstrated by the open loop response in Figure 3.12. The approximated response is not expected to be an identical replica of the actual response. The most important aspect of comparison is by comparing the transient response of both systems, since any steady state error will be compensated by the controller. Equation 3.10 is the transfer function of the second order linearized model of the buck converter given the parameters defined in Table 3.1, where s is the complex variable of the Laplace transform.

$$\frac{V_{out}(s)}{D(s)} = \frac{-5350s + 4.231e7}{s^2 + 5249s + 3.976e4} \tag{3.10}$$

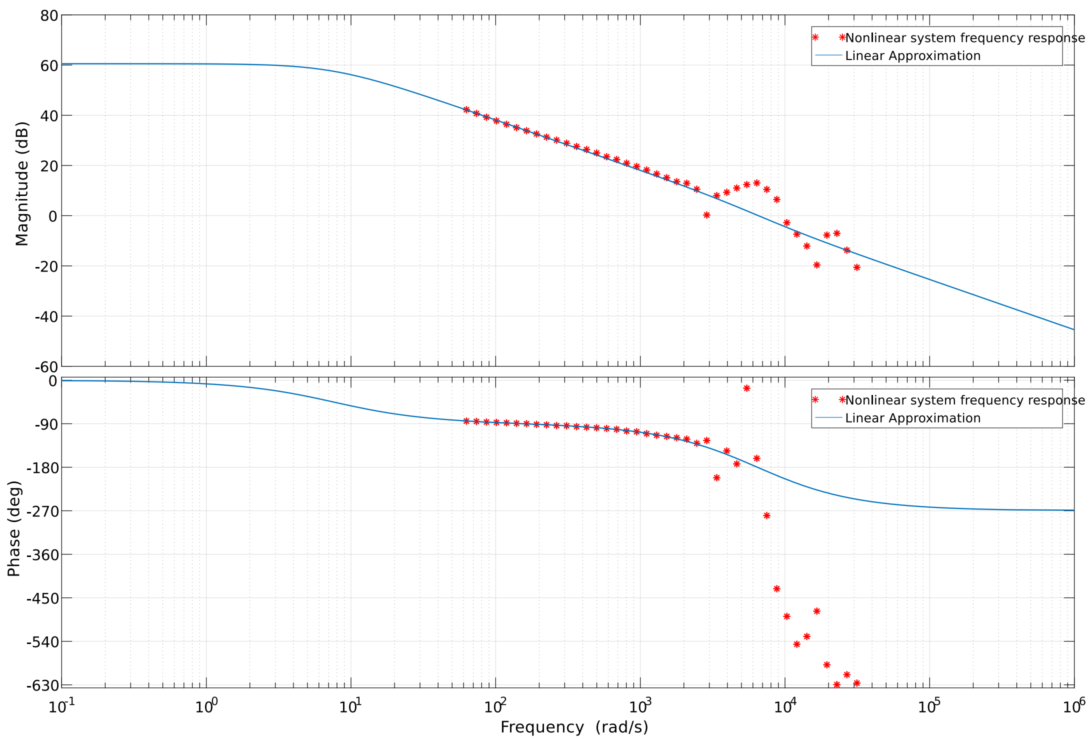

Figure 3.11: Open-loop frequency response of the buck converter given the parameters in Table 3.1, and the open-loop frequency response of the linearly approximated system.

[1]The "goodness of fit", also known as the Fit Percent, is the normalized root mean square error fitness value which is calculated using the following equation: $gof(\%) = 100(1 - \frac{||y-\hat{y}||}{||y-mean(y)||})$, where y is the validation data output from the actual system, $\hat{y}$ is the output of approximated system, and $||$ indicates the 2-norm of a vector.

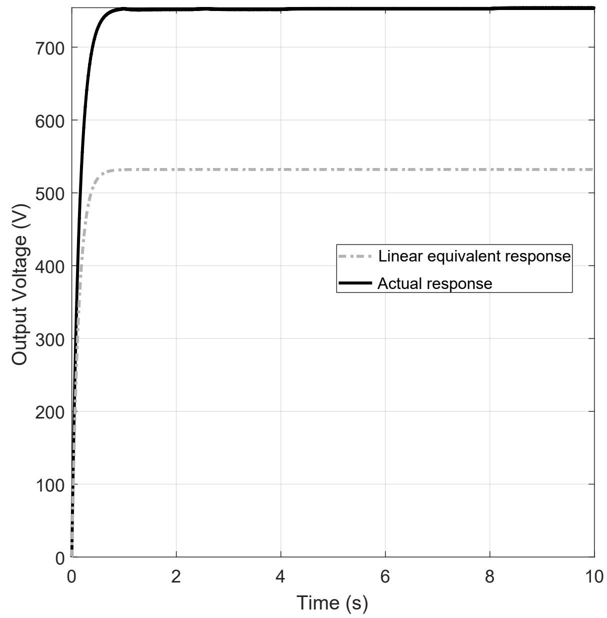

Figure 3.12: The open loop output voltage response of the buck converter in comparison to that of the linearized model.

Closed loop system and PID controller tuning Figure 3.13 outlines closed-loop control of the buck converter. The simple buck converter employed in this study is a second order system as it only contains two energy storage elements, the inductor and the capacitor. It has two state variables, the inductor current (input current) and the capacitor voltage (output voltage). The schematic of the closed loop PID control of the converter's output voltage is presented in the Figure 3.13.

After producing an acceptable linear approximation of the open-loop system, and validating the response of the linear approximation against the actual nonlinear system, the next step is to synthesize a controller. Simulink has a PID tuning tool that can be used with the linear approximation of the actual system.

There are trade offs when tuning a PID controller. Increasing the speed of the response (i.e. reducing the settling time) will most likely lead to an increase in overshoot and oscillations resulting in an under-damped system. The opposite is also true, an over-damped system will have a significant settling time but will not overshoot or oscillate. A settling time of less than 5 seconds is permissible given that railway systems are inherently slow. Once the PID controller has been tuned given the linearly approximated second order plant, it is then applied to the actual non-linear buck converter circuit. The closed loop response of both systems are then compared.

The output of the PID controller is an analog signal that corresponds to the duty cycle as illustrated in Figure 3.13. A pulse width modulation (PWM) block must be used to convert that duty cycle into switching signals that trigger the switch, S_1, ON and OFF. There are many techniques that perform Pule Width Modulations. The simple technique used in this study is one where the duty cycle analog signal is compared to a sawtooth waveform of the switching frequency, f_s, calculated earlier. Both signals must be amplitude restricted between 0 and 1, corresponding to a 0% duty cycle (always ON) and a 100% duty cycle (always OFF) respectively. Whenever the duty cycle signal is higher than the sawtooth waveform, the switch is turned OFF, and ON when the opposite is true. The result is a train of pulses of fixed frequency, f_s, but of varying duty cycle.

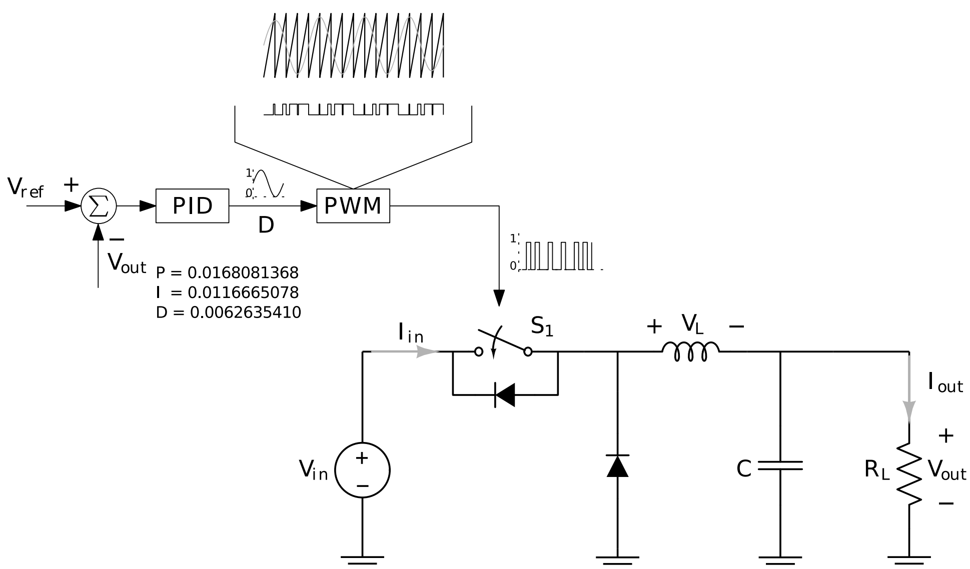

Figure 3.13: Closed-loop PWM control of the output voltage in a buck converter using a PID controller.

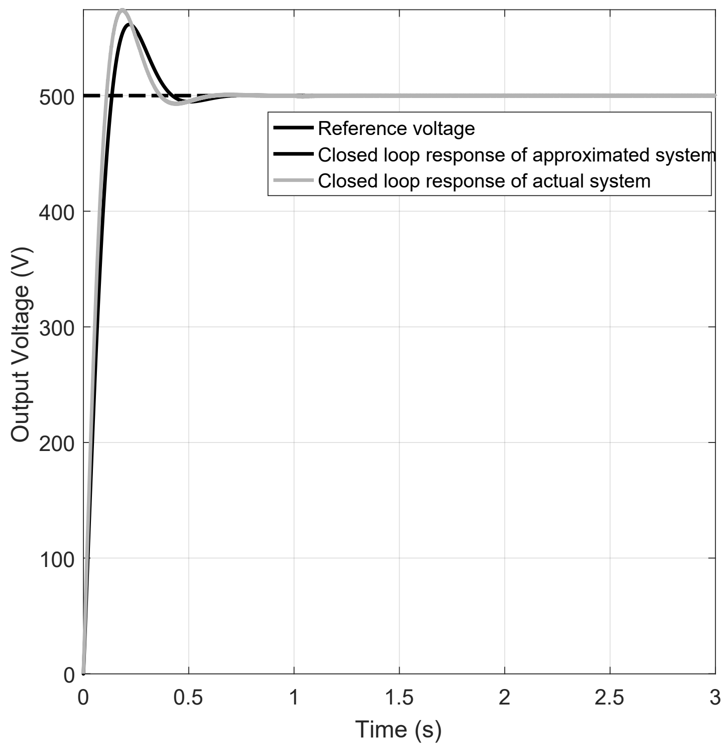

Figure 3.14: Closed-loop response of PID controlled buck converter.

3.4.2 Boost Converter

A boost converter is a DC to DC converter which steps up the input voltage and steps down the input current. It is used to interface a low voltage source with a higher voltage DC bus. The converter used in this study is an ideal converter with a single ideal switch, ideal diode and ideal inductor and capacitor. The circuit layout is presented in Figure 3.15.

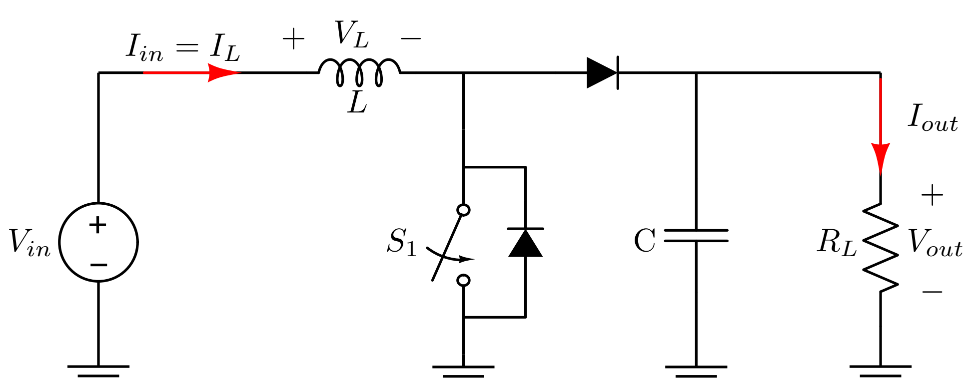

Figure 3.15: Circuit layout of a non-isolated boost converter with a purely resistive load.

Open-loop design and simulation Boost converters cover a wide range of output voltage as Figure 3.16 illustrates. The value of the output voltage, V_{out}, depends on the duty cycle, D, and is governed by Equation 3.11. For component sizing purposes, an operating point has to be carefully chosen to ensure proper operation even as parameters slightly change.

$$V_{out} = \frac{V_{in}}{(1 - D)} \tag{3.11}$$

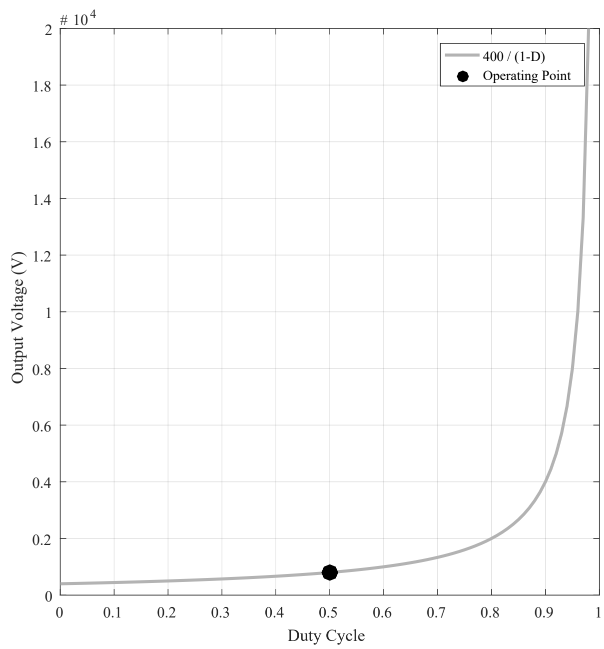

Figure 3.16: Output voltage as a function of switching duty cycle. The operating point at 50% duty cycle is highlighted.

In the FCB hybrid powertrain presented in Subsection 4.2.4 and Subsection 4.1.4, a boost converter is used to interface between a 400 V FC system and a 1500 V battery bank. In practice, both these values will change throughout a trip. Depending on the current draw from the FC, its voltage may drop. Although fuel flow rate control systems should exist to keep the FC's voltage constant, the boost converter must be able to adapt to input voltage fluctuations.

Similarly, the battery bank's voltage will not be constant throughout the trip. The battery's charge will deplete as it provides transient power to the traction system, and will recharge if energy is available from the FC or from regenerative braking.

For this reason, the use of closed loop control systems was necessary. As mentioned earlier, classical linear control can only be used to control power electronic converters if the range of operation is bounded to a region where linear approximations of the nonlinear model can be made. By examining Figure 3.16, we can see that higher duty cycle values result in an increasing rise in output voltage. The figure also highlights the selected operating point at 50% duty cycle. At this operating point, the output voltage V_{out} is 800 V.

The next step in the converter design is to size the inductor and capacitor. Both the output voltage ripple Δv_{out} and the input current ripple Δi_{in} are inversely proportional to the switching frequency f_s as suggested by Equation 3.12 and Equation 3.13 respectively. The output voltage ripple Δv_{out} is also inversely proportional to the output capacitor size C while the input current ripple Δi_{in} is inversely proportional to the input inductor size L.

$$\Delta v_{out} = \frac{V_{out}}{R} \times \frac{D}{C f_s} \tag{3.12}$$

$$\Delta i_{in} = \Delta I_L = \frac{V_{in} D}{L f_s} \tag{3.13}$$

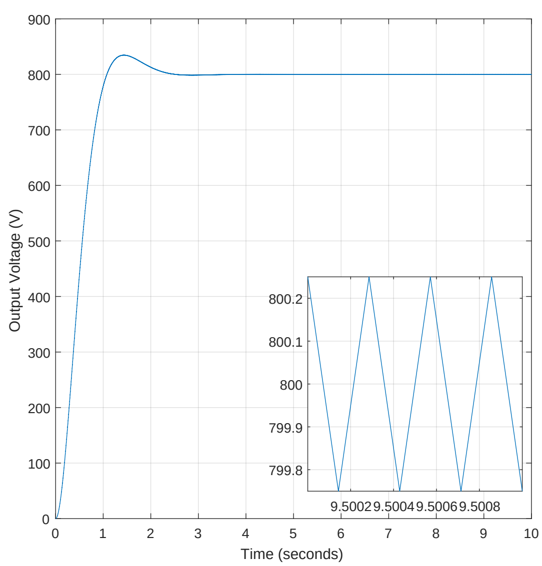

(a) Open-loop output voltage V_{out} at 50% duty cycle with a ripple amount Δv_{out} of 0.5 V

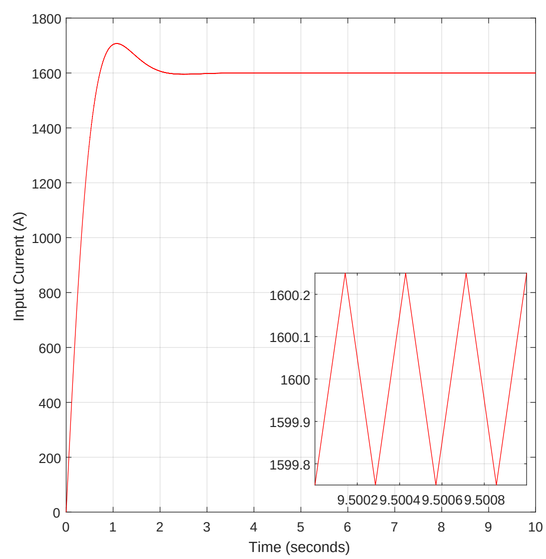

(b) Open-loop input current I_{in} at 50% duty cycle with a ripple amount Δi_{in} of 0.5 A

Figure 3.17: The open loop output voltage and input current of a simplified boost converter given the circuit parameters in Table 3.2.

This suggests a trade off between element sizes and switching frequency for any given ripple value. For example, a higher switching frequency f_s and a small inductor L will give the same input current ripple magnitude as a lower switching frequency f_s and a bigger inductor L, as governed by Equation 3.13. The same trade off exists between the output voltage ripple, capacitor size and switching frequency f_s. The minimum inductor size (L_{crit}) for continuous conduction is governed by Equation 3.14.

$$L_{crit} = \frac{V_{in} D(1 - D)}{2 I_{out} f_s} \tag{3.14}$$

In this study, boost converters have one function regardless of their location in the powertrain. They are either used to boost the FC voltage to charge the battery in a FCB series hybrid, or to boost the regenerated voltage during regenerative braking. Parameters used in the simulation are included in Table 3.2.

Table 3.2: This table contains the open-loop circuit specifications for the boost converter used in this research.

V_{in}	400	V
V_{out}	800	V
D	50%	
R	1	Ω
I_{in}	1600	A
I_{out}	800	A
f_s	3500	Hz
Δi_{in}	0.5	A
Δv_{out}	0.5	V
L	0.1143	H
C	0.2286	F

Linearized system identification Following the same process explained in the previous section, a linear approximation of the boost converter was synthesized and its frequency response is compared to the frequency response of the actual non-linear system as shown in Figure 3.18. According to Matlab, the "goodness of fit" was 83.7%. In a FC series hybrid, it is important to control the boost converter's input current which is also the FC's output current. Equation 3.15 is the transfer function of the second order linearized model of the boost converter given parameters defined in Table 3.2.

$$\frac{I_{in}(s)}{D(s)} = \frac{3222s + 8.338e4}{s^2 + 6.826s + 24.67} \tag{3.15}$$

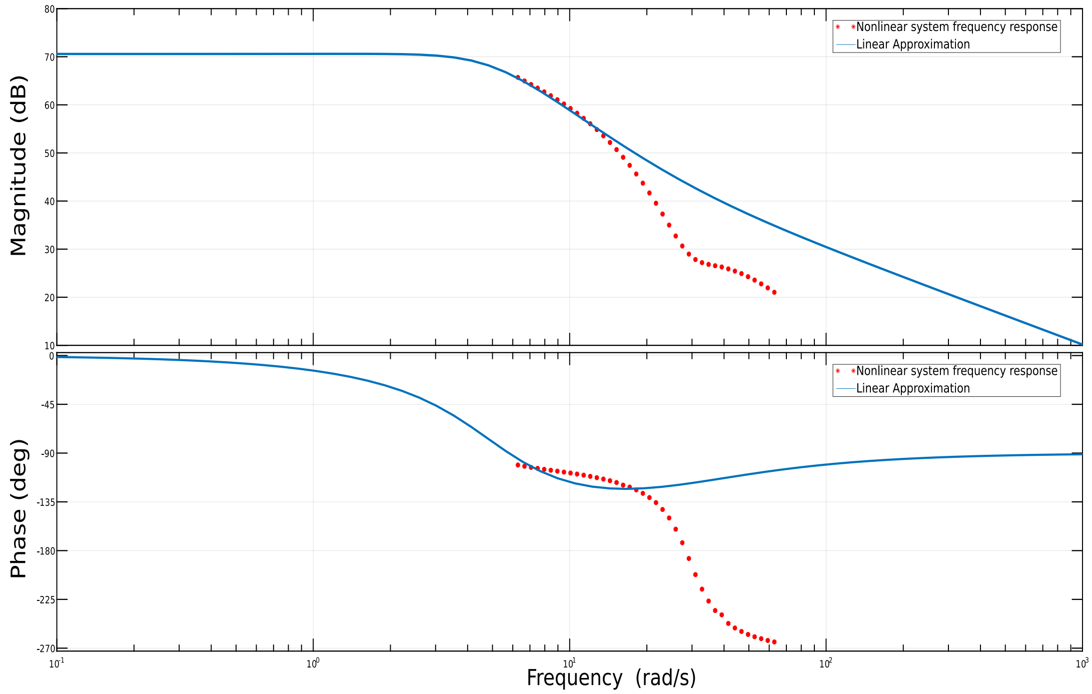

Figure 3.18: Open-loop frequency response of the boost converter given the parameters in Table 3.2, and the open-loop frequency response of the linearly approximated system.

Figure 3.19 shows how the open loop input current of the actual system and the approximated system compare. As mentioned earlier, the approximated response is not expected to be an identical replica of the actual response. The most important aspect of comparison is by comparing the transient response of both systems. Any steady state error will be compensated by the controller.

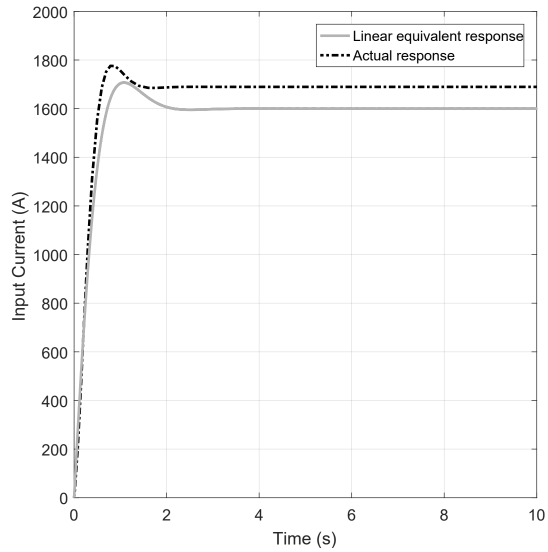

Figure 3.19: Open loop input current transient response at 50% duty cycle.

Closed loop system and PID controller tuning Figure 3.20 outlines closed-loop control of the input current in a boost converter. After producing an acceptable linear approximation of the open-loop system, and validating the response of the linear approximation against the actual nonlinear system, the next step is to synthesize a controller. Simulink has a PID tuning tool that can be used with the linear approximation of the actual system.

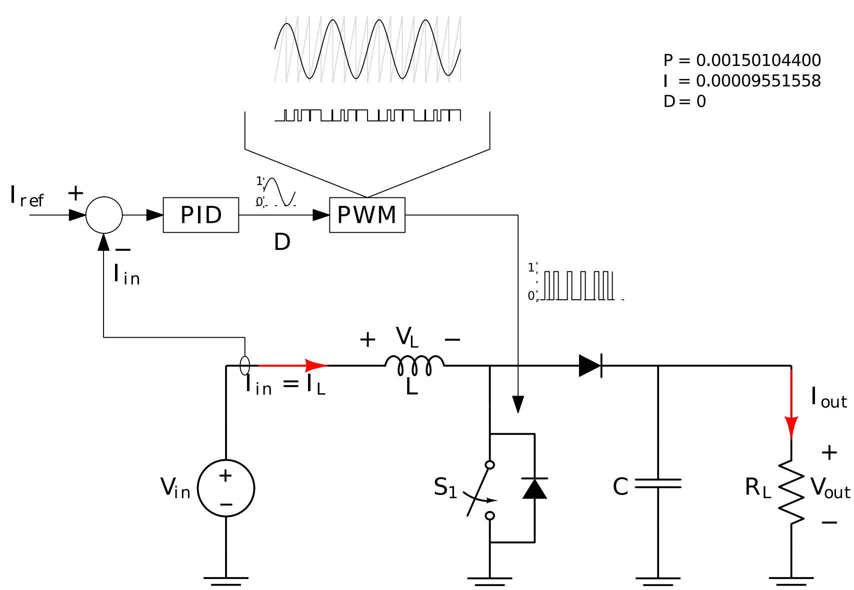

Figure 3.20: Closed-loop PWM control of the input current in a boost converter using a PID controller.

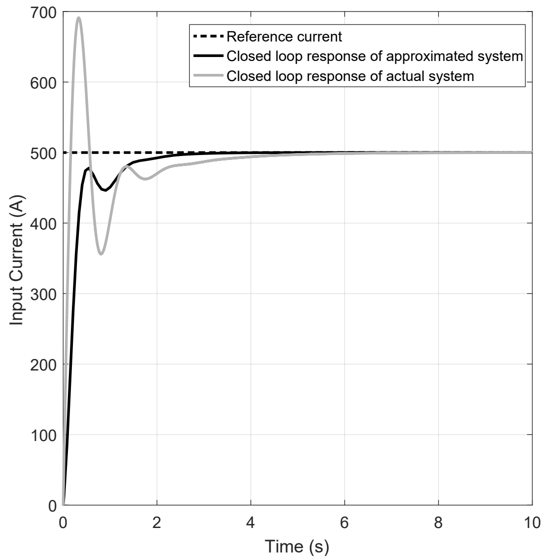

Figure 3.21: Closed loop input current transient response assuming a 500 A reference input current.

3.4.3 Bidirectional Buck and Boost Converter

The previous sections discussed the design, modeling and closed-loop control of buck and boost converters. The load interface converter used in this study is a bidirectional converter that is a combination of the buck and the boost converters. To be bidirectional, a converter much allow power flow in both directions. Through the use of switching devices and diodes, the direction of the electric current can be controlled. A bidirectional converter is needed to allow for energy regeneration during braking.

To simplify circuitry and therefore control, the power source has to be of sufficiently high voltage as to cover the entire rotational speed range of the traction machine without the need for a voltage boost. This would necessitate the use of a buck converter when power flow is from source to load. Operating at higher voltages is better than operating at higher currents for the same power levels to minimize the energy lost in the conductors.

This creates the need to use a boost converter when power is to flow from load to source, for example during regeneration. The boost converter would reverse the current direction in the circuit, and boost the voltage across the traction machine terminals to suitable levels for charging the ESS. Figure 3.22 illustrates the modes of operation of the converter employed in this study.

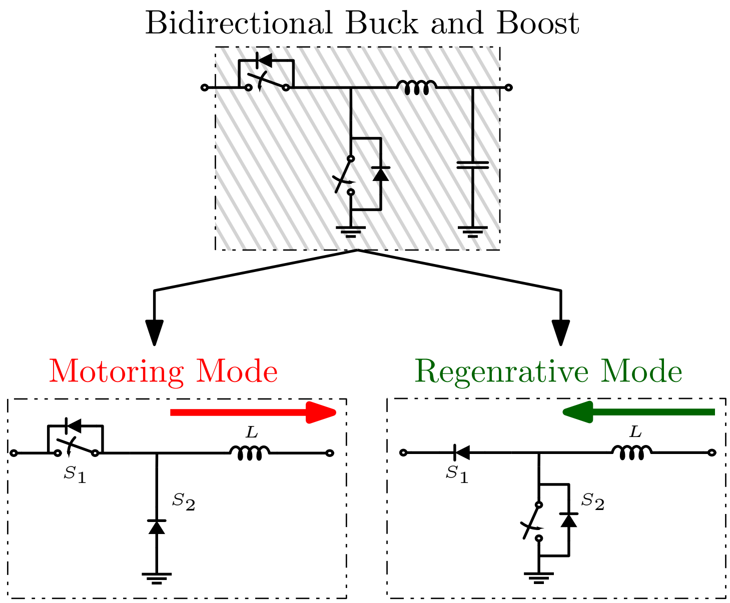

Figure 3.22: The circuitry of the bidirectional buck-boost converter which interfaces the energy source with the traction machine.

3.4.4 Online Deterministic State Machine Control

To simplify the design and simulation of the hybrid systems discussed in this study, a simple two state heuristic controller was implemented in Simulink. Since we do not aim to study or comment on the impact of control systems on energy consumption, it would be unproductive to spend time designing and simulating a more complex control system.

The two states that determine the operation of the power electronic converter and the direction of energy flow are: a 1) Motoring State, and a 2) Regenerative Braking State. As the names suggests, the motoring state is the state in which the energy flow is from storage device to traction machine, and the power electronic converter interfacing the source and the load is operating in buck mode. In this state, the source voltage of 1500 V is stepped down through a buck converter, and the duty cycle is decided by the PID controller. The opposite of that is the regenerative braking state, in which the energy flow is from traction machine to storage device, and the power electronic converter interfacing the source and the load is operating in boost mode.

As mentioned in section 2.4, state machine control is documented to suffer from unwanted oscillations or “chatter” when operating at the boundary condition between any two states [40].

It takes time for the PID controller to adjust the switching duty cycle of the converter to produce a zero velocity error between the actual velocity and the reference velocity profile. This time is termed the "settling time", referred to as t_s in Figure 3.23. This highlights the importance of choosing a critically damped (no overshoot) PID controller, otherwise the state machine control mechanism will alter the state of the controller unnecessarily producing undesirable results or oscillations as presented in Figure 3.23.

The boundary condition in this case is the zero error condition, if the speed error is positive indicating that the actual speed is less than the reference speed, the motoring state is invoked, otherwise the regenerative braking state is invoked. If the error oscillates around zero however, this will result in an uncontrollable system behavior. One solution to this problem is to introduce a delay in the state transition mechanism. This delay should be larger than the settling time to filter out oscillations due to any overshoot produced by the PID controller, but sensitive enough to realize when a change of state is needed. Another solution would be to introduce a boundary gap between the two states. It is therefore obvious that this control technique is not a robust one, but its main advantage is its simplicity. Figure 3.23 explains the operation of the control system.

Figure 3.23 illustrates how the chosen control mechanism functions. In it we see how the acutual vehicle speed attempts to match the reference speed. The figure is of a vehicle that starts in regenerative braking mode and transitions to motoring mode when the actual speed becomes lower than the reference speed. After the state of the control system changes, it takes some time, t_s, for the power source to deliver enough power for the vehicle to accelerate, matching the actual speed to the reference speed. Towards the end of the trip, the vehicle transitions from motoring mode to regenerative braking mode. In motoring mode, the vehicle will attempt to follow the reference speed profile by adjusting the magnitude of power delivered to the traction motors. If the vehicle continues to accelerate and no power is being supplied, then the direction of power flow must be reversed to absorb energy from the system. The figure also illustrates the oscillations that may occur at boundary conditions as mentioned earlier.

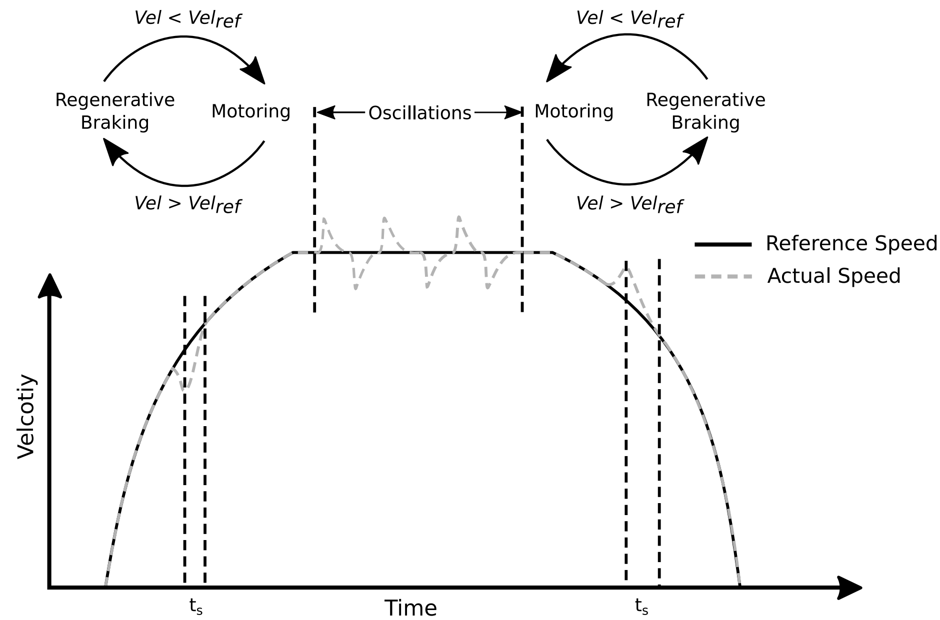

Figure 3.23: The impact of a two-state state machine deterministic controller on the vehicle velocity as compared to the provided reference velocity profile.

3.4.5 Combined Simulink Model

Producing a locomotive powertrain model and simulating an actual train trip is a complex task. So far, all the subsections of this chapter discussed all the different components of the Simulink model. Section 3.2 presented an overview of the longitudinal dynamics of railway vehicles which was later combined with concepts mentioned in Section 3.3 to produce a velocity trajectory profile given a certain railway-consist (train) and a defined route. In Section 3.4 we discussed the need for power electronic converters on-board the railway vehicle, and presented an overview of the design, modelling and control of a buck and a boost converter. We also mentioned how the two converters were combined into one simplified converter that allowed bidirectional power flow. Other powertrain components such as the traction machine, lithium-ion battery bank, supercapacitor bank, and FC system models were not explicitly defined in the body of this thesis since the study relied on models present in the literature and readily available in the SimPowerSystems library in Simulink. Section 3.5 and Section 3.6 discuss how all the different subsystems are integrated in a combined Simulink model.

3.5 Battery - Supercapacitor Parallel Hybrid Powertrain Description

BSC Parallel Hybrid Powertrain The parallel hybrid architecture chosen for this study allows both power sources to react independently to changes in load. Essentially, it allows for complete control for the power split between the two sources. If a series hybrid architecture was chosen, one source will always be feeding the other which would not allow the independent evaluation of each source.

For an unbiased transient response, L_{bat} and L_{sc} have the same value. This would allow us to estimate how each source reacts to changes in load. As illustrated in Figure 3.24, each power source is connected to a separate bidirectional buck-boost converter. Control signals to switches S_1 and S_3 are synchronized so that both switches turn on and off at the same time. The same is applied to switches S_2 and S_4. This guarantees that both sources are either in motoring mode or in regenerative braking mode without the option for one source to be in one mode and the other in another mode. This prevents one source from feeding the other, which allows to judge the ability of each source to respond to transient load changes based solely on its intrinsic characteristics, and simplifies the control system design.

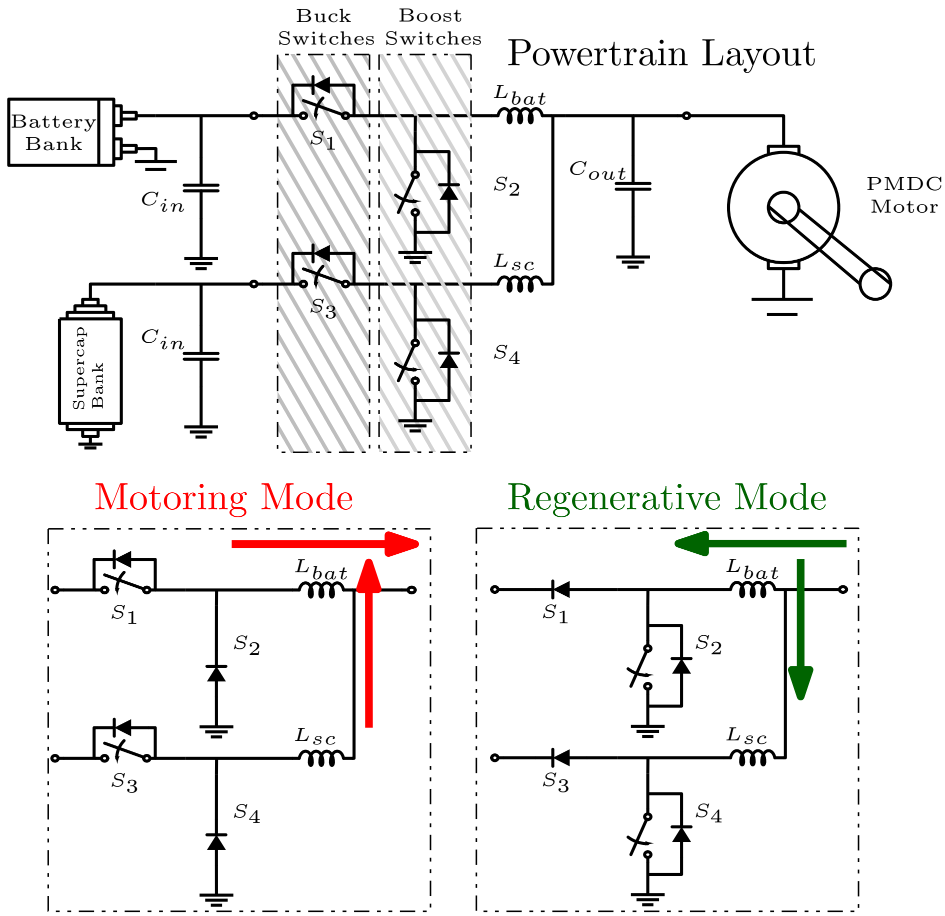

Figure 3.24: BSC parallel hybrid powertrain architecture.

The combined model All of the different subsystems discussed earlier have to be combined into a single Simulink model. Figure 3.25 presents an illustration of the combined model. The traction machine's rotational speed and torque are stepped up or down according to a predefined gear ratio. Rotational speed is then converted to translational velocity through the wheelset attached to the gearbox. This translational velocity is then used to calculate the retardation force F_R using the Davis equation described in Equation 3.3.

The distance traveled (location) can be calculated by integrating the translational velocity. The location is used to find the corresponding velocity limit and elevation magnitude provided in distance coded lookup tables. The output of the elevation lookup table is the gravitational force F_G which is added to the other retardation forces resulting in a net retardation force F_{net}. The net retardation force is converted to load torque on the traction machine.

The output of the velocity profile lookup table is the desired velocity at each section as calculated using methods discussed in Section 3.3. This output is then compared to the actual speed of the vehicle and an error signal is produced. Two PID controllers act on that error signal and produce a PWM signal of a duty ratio corresponding to the desired motor speed. The error signal is also used to determine the direction of power flow, either motoring mode or regenerative braking mode. The power electronic converters will then operate to deliver power to the traction machine, resulting in an increase in the vehicle's speed. It is then integrated to produce displacement that is then fed to the lookup tables to find the elevation and velocity limits. The simulation is terminated once the train reaches its destination.

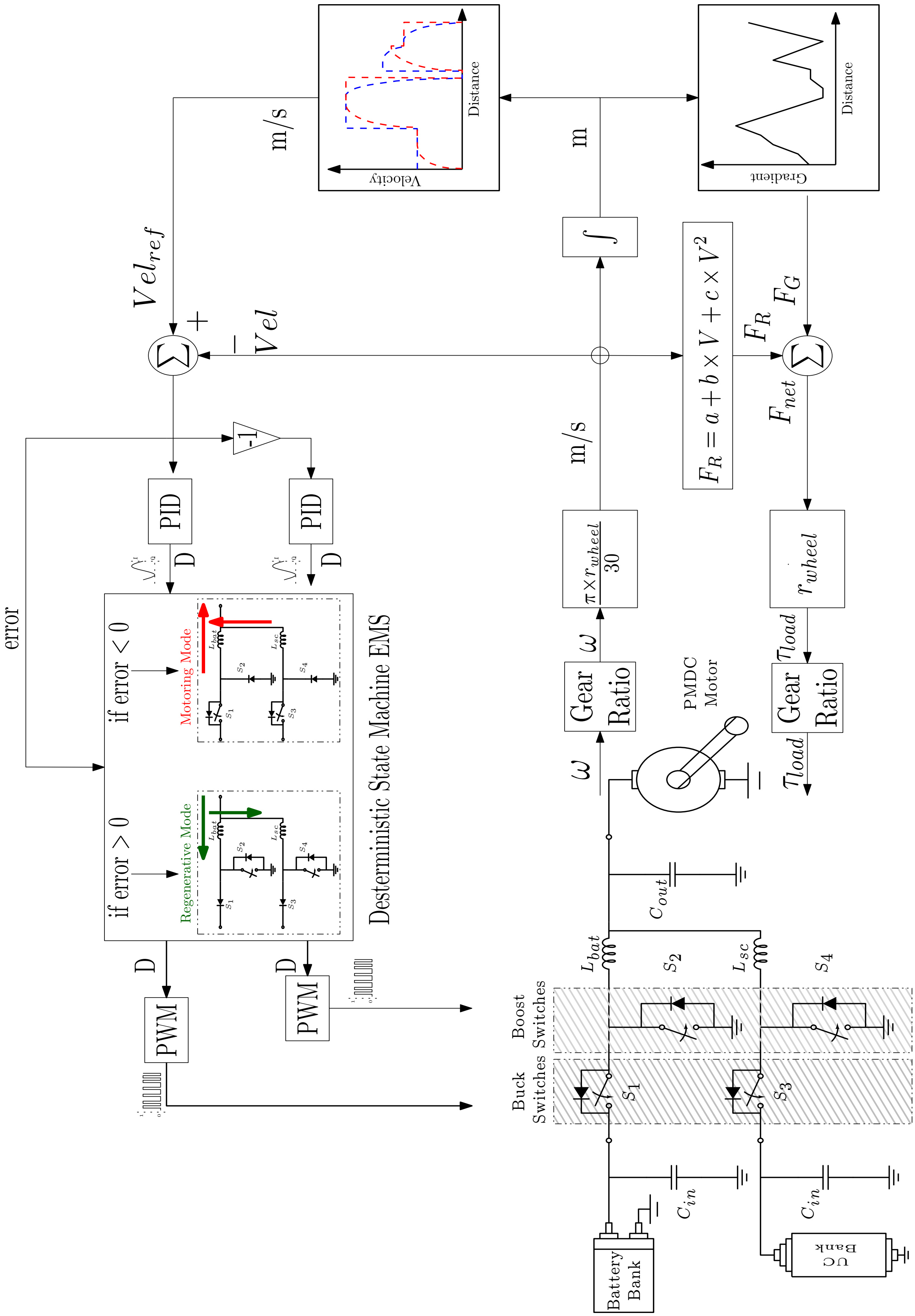

Figure 3.25: The combined battery / SC parallel hybrid powertrain Simulink model.

3.6 Fuel cell - Battery Series Hybrid Powertrain Description

The FCB series hybrid powertrain As explained earlier in Subsection 2.4, there are advantages and disadvantages for every type of powertrain architecture. In series hybrids one of the power sources acts as a buffer between the prime-mover and the load. This series architecture does a better job of maintaining the battery SOC whilst meeting all the required power transients [59].

FCB series hybrids have been studied in a wide array of traction applications, ranging from railway [60] and collection trucks [61] to lighter duty experimental setups [62, 63].

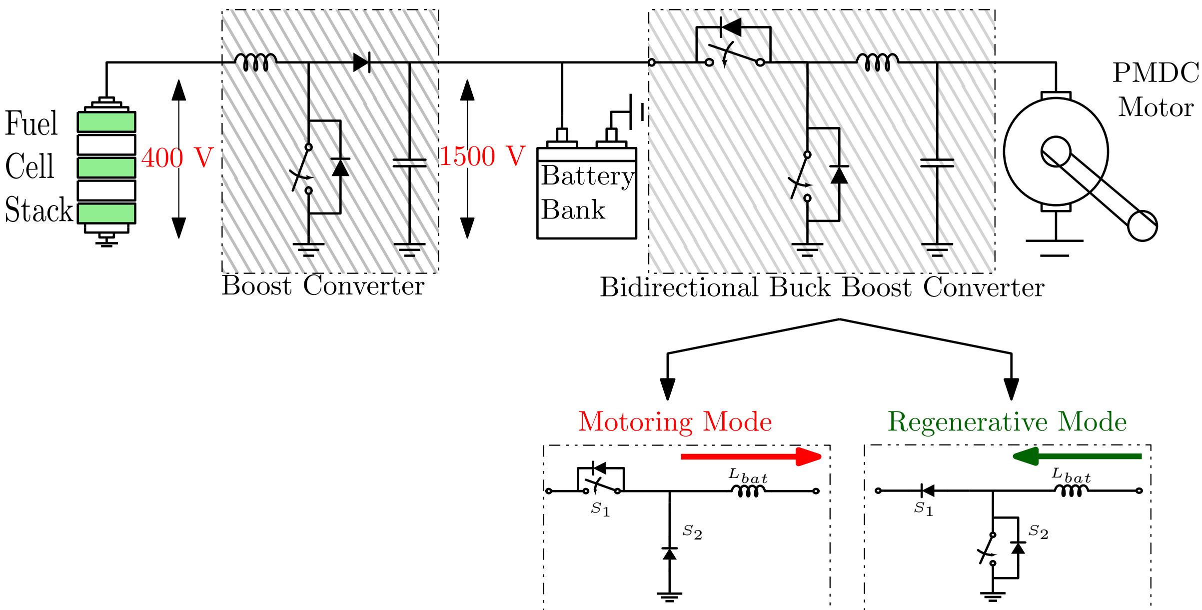

Figure 3.26: FCB series hybrid powertrain architecture.

The combined model As mentioned in Section 3.5, all of the various subsystems have to be combined into one Simulink model that represents a FCB series hybrid train. Figure 3.27 illustrates how all the different subsystems were interconnected into one Simulink model in this study.

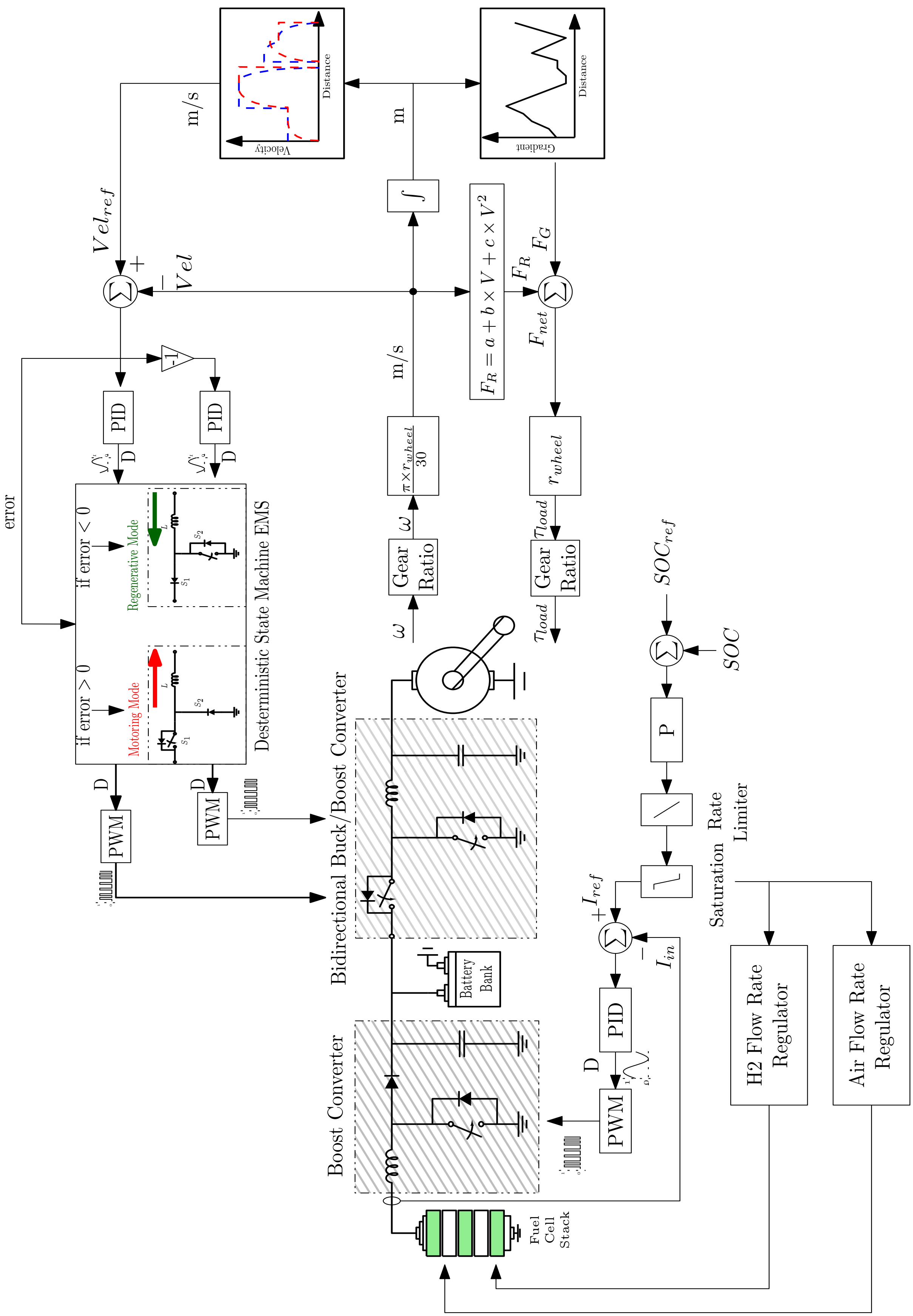

Figure 3.27: The combined FCB series hybrid powertrain Simulink model.

3.7 Numerical Optimization Process

As mentioned in Section 1.1, one of the main goals of this thesis is to make an attempt at optimizing the sizing mix of the on-board ESS. Normally, we would need to identify the exact parameters that are to be optimized before attempting to optimize the on-board ESS mix. Instead, this thesis will present how the mix of the on-board ESS impacts certain key parameters. These parameters include figures of merit such as fuel economy and battery SOC depletion.

The first step in any optimization problem is to identify limits or boundary conditions. In this study, two physical boundary conditions exist: a mass boundary condition and a volume boundary condition. All possible solutions must satisfy both conditions, meaning that they must fall within the unshaded region. Note that the optimal solution for a given application must lie within this region.

Since this problem is too complex to be solved analytically, computational means were employed. Iterating the simulation at different ESS sizing ratios and logging the results of each simulation at a sufficiently high resolution can help in identifying trends and optimal regions. The results can be interpolated to find the estimated fuel economy at any point.

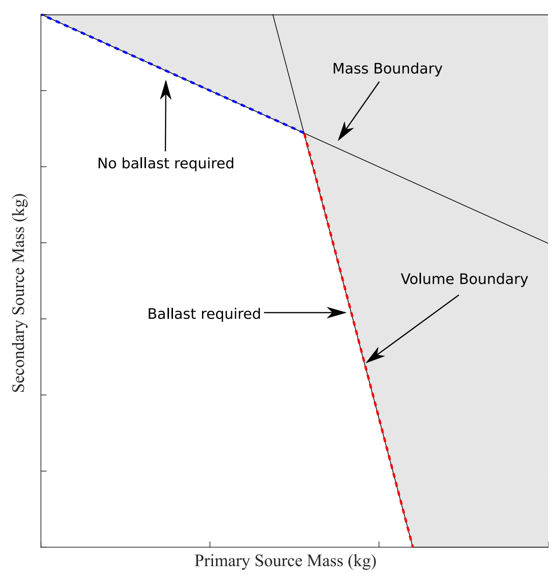

Figure 3.28: A graphical representation of the optimization problem that appears when deciding on the hybridization mix.

Chapter 4

Results and Discussion

This chapter of the thesis presents the results obtained from the simulations conducted on Matlab / Simulink. The chapter is divided into two sections that present the results for each of the two case studies considered. The first case study is a 28 kilometer round trip from Trehafod to Treherbert in the UK. The trainset is made up of two British Class 150 diesel motive units (DMUs). The second case study is a much longer 864 kilometer round trip from London's King's Cross Station to Newcastle. The trainset in the second case study is the Intercity 125. It is made up of two British Class 43 locomotives hauling 6-8 passenger carriages that can carry approximately 600 seated passengers.

Each section is further divided into four subsections that 1) describe the train, 2) describe the route, 3) discuss the results for the battery/ultracapacitor hybrid study, and 4) discuss the results for the fuel cell / battery hybrid study.

Since there exists an infinite number of ESS sizing combinations, each with its own set of results, only a selected set is presented. A detailed set of single trip results for a specific sizing combination as a representative example of all the simulations conducted is presented and discussed. This is then followed by a discussion of results obtained if the train were to repeat the trip continuously over a 15-16 hour operational day. Finally, the results of the overall optimization study are presented and discussed.

4.1 British Class 150: Trehafod to Treherbert

4.1.1 Train Description

British Class 150 is a DMU that runs on a 200 kW diesel engine. Typically, two or three of these units will form a trainset. Each DMU has one powered bogie and one trailing bogie as shown in Figure 4.1. The case considered in this study is one where a trainset is formed of two DMUs that can carry 200 - 250 passengers. Table 4.1 contains the DMU specifications.

The space available for hybrid ESS installation was assumed to be 3.5 tonnes at 4000 Liters. This assumption was based on the combined mass and volume of the diesel engine and fuel compartment. Whenever mass and volume are discussed in this chapter, they refer to per-wagon mass and volume. For example, the mass constraint mentioned earlier is for a single DMU, and not for the entire trainset which is comprised of two DMUs. Also, when ESS mass is discussed, it refers to mass per DMU or locomotive and not for the entire trainset.

Table 4.1: The specifications of British Class 150 DMU.

Physical Specs	
Length	20.06 m
Width	2.816 m
Height	3.774 m
Wheel Diameter	0.834 m
Mass	35.8 tonnes
Fuel Capacity	1500 L
Davis Equation (kN)	$2.089 + 0.0098v(m/s) + 0.0065v^2(m/s)$
Performance Specs	
Maximum Speed	120 km/h
Maximum Engine Power	213 kW

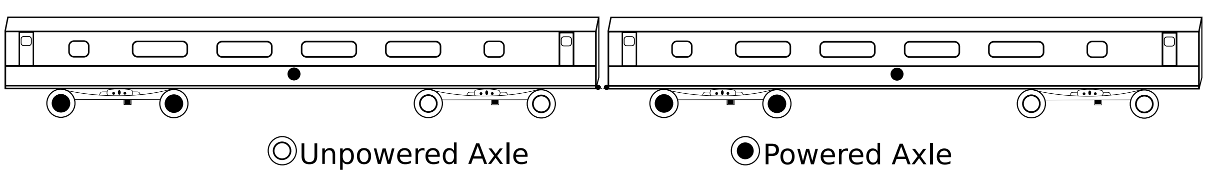

Figure 4.1: Class 150 train consists of two Class 150 DMU.

4.1.2 Route Description

The route chosen for this study is the 14 kilometer route from Trehafod to Treherbert in the UK. It is a standard short route that is typically found in urban areas. It has an uneventful elevation profile. As the train leaves the Trehafod station, it almost steadily gains elevation till it reaches the destination at Treherbert. The elevation change in 14 kilometers is 100 meters (see Figure 4.2), or about 7.14 meters altitude gain for every kilometer traveled. This corresponds to a gradient of less than 1%, which is acceptable for railway operation.

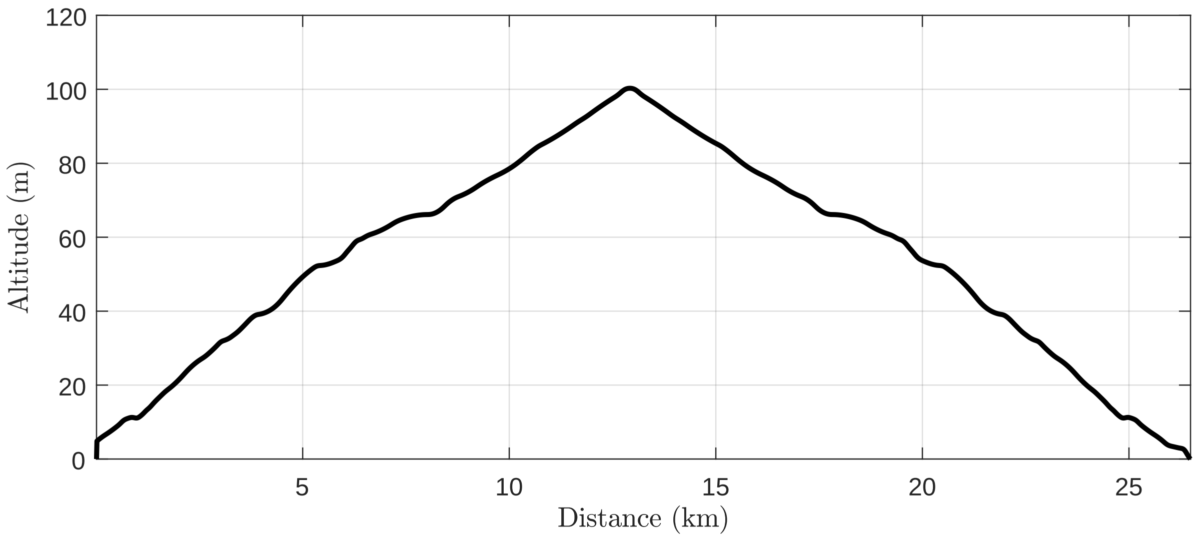

Figure 4.2: Trehafod to Treherbert altitude profile.

Figure 4.3 shows the velocity profile for the trip. The Simulink simulator works by solving system equations with time as the independent variable. Therefore, if we allow the velocity profile to reach zero, meaning that the vehicle comes to a full stop at designated stations, the simulator would freeze. As a solution, we generate a velocity profile that does not go to zero, but instead to 1 m/s for a period of time that would correspond to the equivalent delay of a complete stop. By examining the figure, we can see that the train makes 9 stops between Trehafod and Treherbert resulting in a one way trip time of approximately 23 minutes. Although the train is capable of a 120 km/h top speed, it barely reaches 80 km/h assuming a fast-as-possible trajectory as computed using methods discussed in Section 3.3.

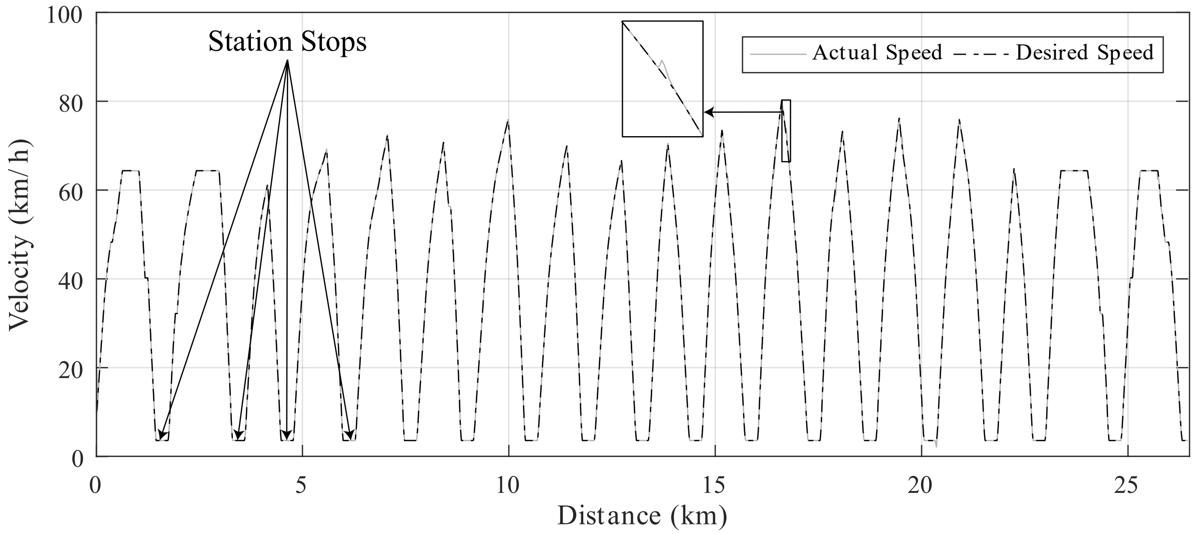

Figure 4.3: British Class 150 Train Velocity Profile: Trehafod to Treherbert. The inset plot highlights the perturbation that occurs when the system changes the mode of operation from Motoring mode to Regenerative braking mode.

4.1.3 Battery - Supercapacitor Parallel Hybrid

In this section, the results of the BSC power train simulation for the given case study are presented and discussed. The results of this section are highly dependent on how much power each source can contribute. Since neither on-board power sources are restricted to a certain maximum power output, they can contribute up to their maximum potential, making the mass of each source the deciding factor. Assuming a 3500 kg 4000 L space, a variety of ESS combinations can exist. For illustration purposes, we focus on a case where the battery bank is 500 kg in mass and the SC bank is 1.5 tonnes. 18,630 *UPF454261* lithium-ion batteries are arranged in 46 parallel branches of 405 series-connected cells each giving a terminal voltage of 1500 volts. The SC bank is made up of 5,786 *BCAP3400* SCs arranged in 11 parallel branches of 526 SCs each.

Figure 4.4 presents the power demand profile during the 45 minute round trip from Trehafod to Treherbert on the British Class 150 DMU assuming a 500 kg battery bank and a 1.5 tonne SC bank in each DMU. Motoring mode is defined as the mode of operation when the power drawn from the power sources is positive; by contrast regenerative mode is the mode of operation when it is negative. The first time the system switches from motoring to regenerating is at approximately minute 23. The first thing to be noticed is that the battery power is capable of handling almost all of the transient power requirements when the vehicle is moving up hill in motoring mode. As the battery loses charge and thus voltage, power from the overhead catenary is used to assist in propulsion. Power is not drawn from the SC bank since its voltage is linearly related to its SOC. Due to the very small energy density of SCs, if power is drawn from the SC bank, its terminal voltage would drop drastically affecting the vehicle's speed. Although the SC bank loses charge slightly in the motoring mode, it appears that its main function is to absorb the regenerated power.

With the presence of a SC bank, the need for frictional braking was drastically reduced. Figure 4.4 shows the times during which a mechanical brake was required to prevent the vehicle's speed from overshooting its desired value. We can see that the braking power needed is small when compared to the amount of regeneration power that is absorbed by the SC bank or the battery bank.

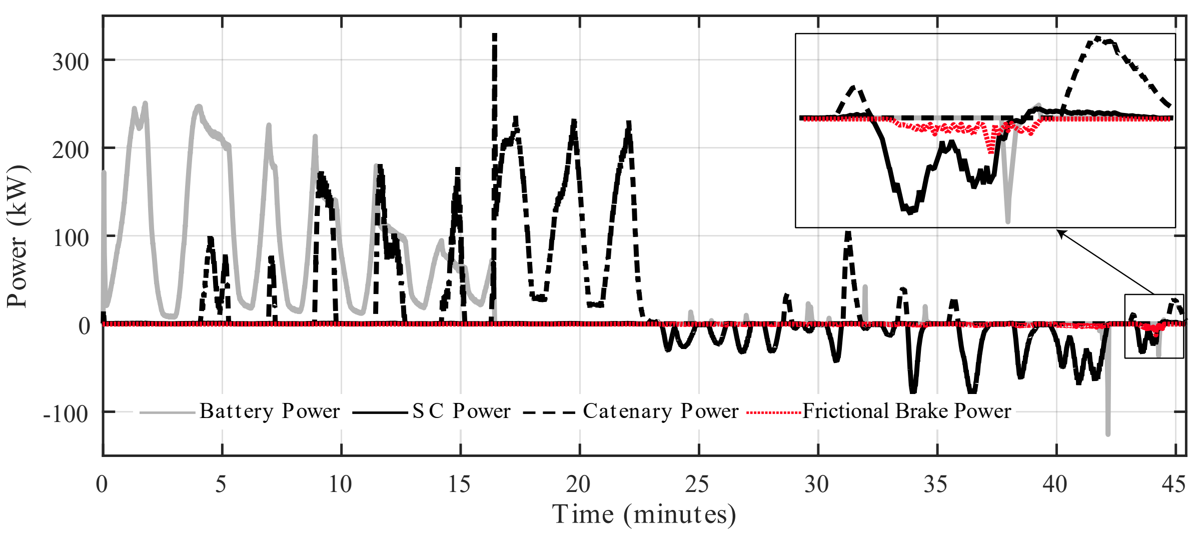

Figure 4.4: Trehafod to Treherbert trip power profile. The battery bank mass in each DMU was 500 kg, and the SC bank was 1.5 tonnes. The inset plot highlights how the magnitude of the frictional braking power compares with the magnitude of the regenerated power as absorbed by the SC or the battery bank.

It is important to examine how the SOC of the on-board ESS changes as the trip progresses. Figure 4.6 presents SOC percentage change of on-board ESS as a function of trip time for the chosen case study. The battery bank's SOC was 70% depleted in approximately 18 minutes. The battery bank's SOC depletion was limited to 70% because excessive depletion of lithium-ion batteries has an adverse impact on their lifetime. The energy regenerated was approximately

5.5 kWh as demonstrated by Figure 4.5, which is about 12.2% of the net energy consumed.

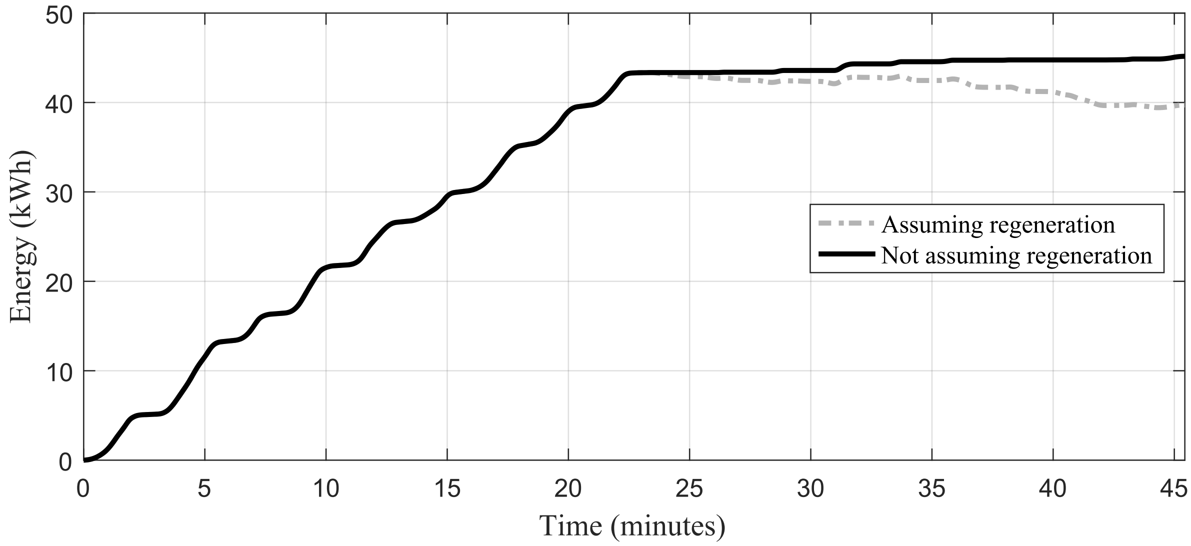

Figure 4.5: Trip energy consumption assuming regenerative breaking versus without regenerative braking. The battery bank mass in each DMU was 500 kg, and the SC bank was 1.5 tonnes.

The 1.5 tonne SC bank (7 Wh/kg) has the potential to hold 10.5 kWh of energy, making the 5.5 kWh regenerated energy approximately 52.3% of full SC charge. However, the SC bank only gained 45% reaching its maximum charge. The difference between the two percentages is attributed to powertrain inefficiencies including SC self discharge phenomenon.

If no SC bank was present, and we assume that the battery bank could absorb power at the required rate, then a 5.5 kWh energy returned to the battery bank would constitute an approximate SOC gain of 5.5% assuming a fixed battery bank of 500 kg at an energy density of 200 Wh/kg. It is important to note that the energy stored in the SC bank can be used to recharge the on-board battery bank.

By comparing Figure 4.6 with Figure 4.4, we observe that the more depleted the SC bank is, the less the need for frictional braking. Before the end of the trip, when the SC bank is at 80% charge, we observe an exponential increase in frictional brake power.

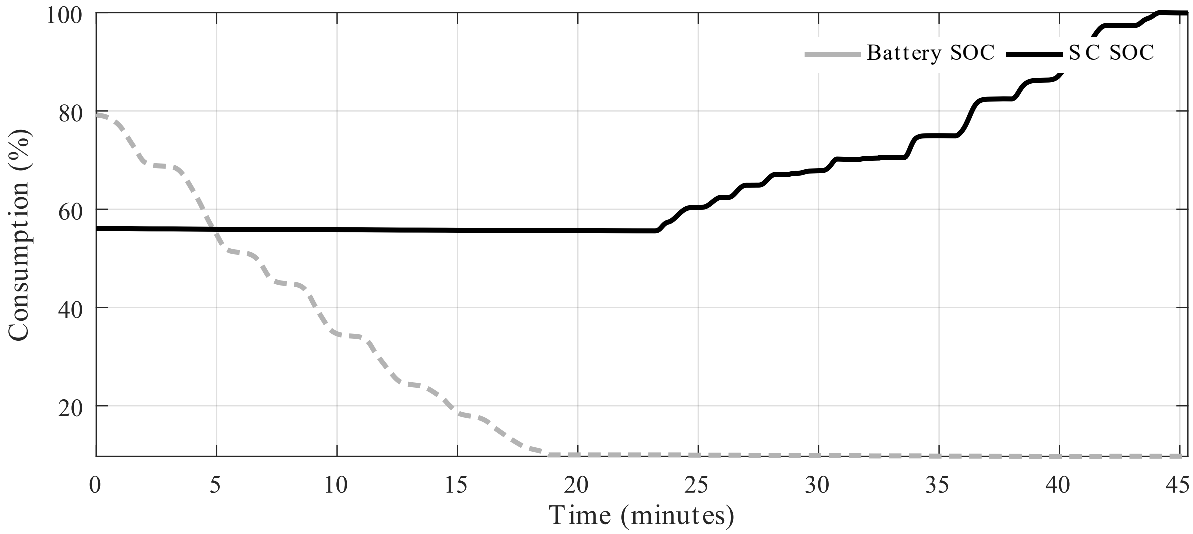

Figure 4.6: The battery bank's SOC, and the SC SOC as a percentage change. The battery bank mass in each DMU was 500 kg, and the SC bank was 1.5 tonnes.

The mean trip powertrain efficiency for this simulation was 91%. The powertrain efficiency is the ratio between the electrical power supplied by the source to the mechanical power supplied by the traction motor. This is an expected value since it represents the efficiency for the PMDC traction machine, the power electronics, and other powertrain inefficiencies. Figure 4.7 illustrates how the powertrain efficiency changes with trip time. By inspecting Figure 4.7 along with Figure 4.4 we can deduce that the powertrain is more efficient when operating in motoring mode than when operating in regenerative braking mode.

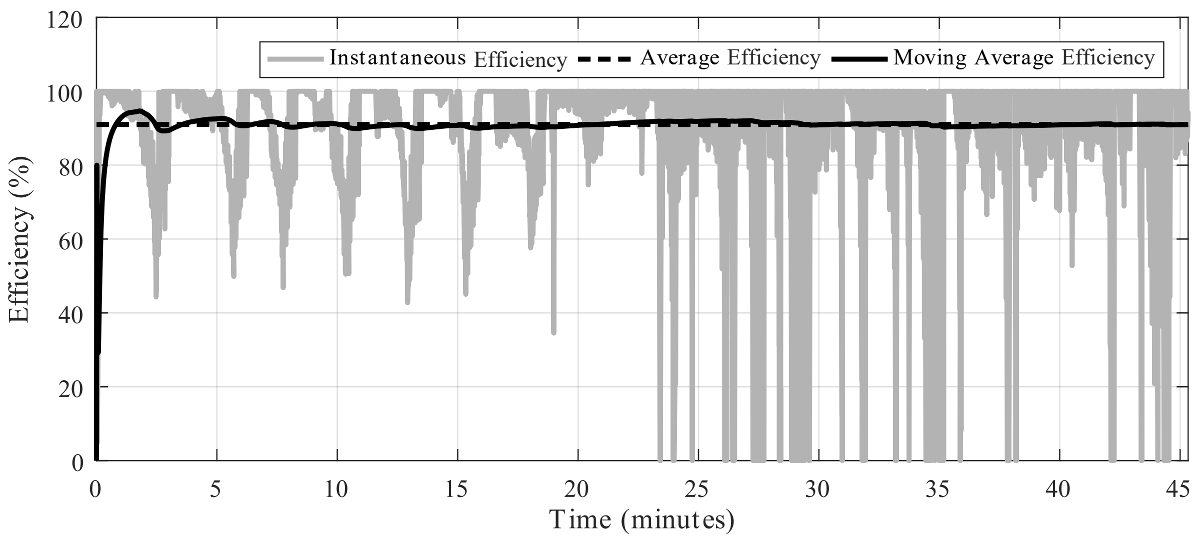

Figure 4.7: Powertrain efficiency excluding the FC stack efficiency. The average powertrain efficiency was 91%. The battery bank mass in each DMU was 500 kg, and the SC bank was 3 tonnes.

ESS Optimization study In this section we demonstrate how the energy storage mix on-board the locomotive impacts certain key parameters such as the maximum regenerated energy, net SOC change, and range of travel in kilometers without the need to recharge.

Figure 4.8 presents a two dimensional view of the ESS optimization problem that arises when deciding on energy storage allocation. The first step is to determine the railway vehicle's physical constraints. The gray area in Figure 4.8 shows the ESSs combinations that are not allowed given said physical constraints. The mass constraint in this study was assumed to be 3500 kg, and the volume constraint to be 4000 L. The density of both the SC and the battery is more than one, which is why the volume constraint line and the mass constraint line do not intersect making the mass constraint the only practical physical constraint as shown in Figure 4.8. The discrete ESS combinations selected for simulation are shown as dotted points in the same figure. The lightest combination considered for simulation is one where the SC bank mass was 500 kg, and the battery mass was 100 kg.

As discussed earlier in Section 3.2, a railway vehicle's mass is essential for proper traction. Therefore, we can alter the composition of the on-board ESS as long as we do not change the vehicle's mass. This may necessitate the used of ballast. The ballast is assumed to be made of steel, and to have a density of 8.17 kg/L. The further the ESS mix is from the mass constraint line, the more ballast is needed. The use of ballast may not be necessary in BSC hybrids due to their density. Intuitively, ESS combinations that lie on the mass constraint line result in more range of travel than the ones that do not since they use all available mass for energy storage. The use of ballast is expected to reduce the overall powertrain cost and therefore is included in the study.

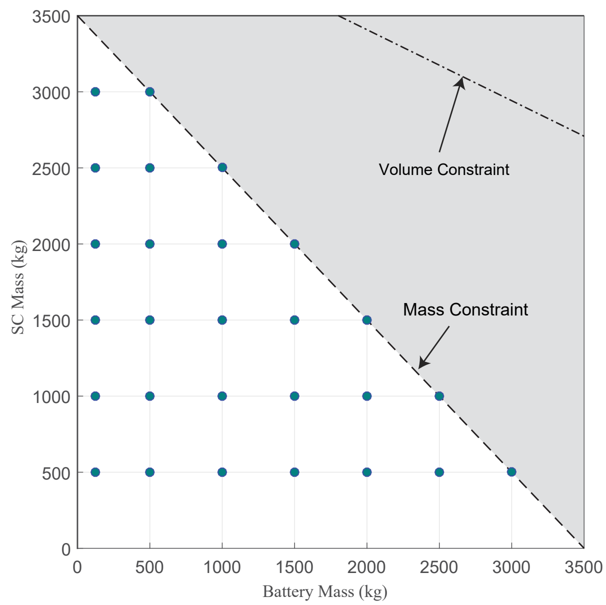

Figure 4.8: A two dimensional illustration of the ESS sizing optimization problem that highlights the cases considered for simulation. The ESS in this study is a BSC hybrid, and the physical constraints are for a British Class 150 DMU. The dotted circles represent the ESS cases selected for simulation.

Figure 4.9 presents the maximum range of travel in kilometers on a single charge as a function of the on-board battery mass. It was found that the maximum range of travel on a single charge was much more dependent on the on-board battery storage than on the on-board SC storage. This is mainly due to the higher energy density of lithium-ion batteries in comparison to SCs.

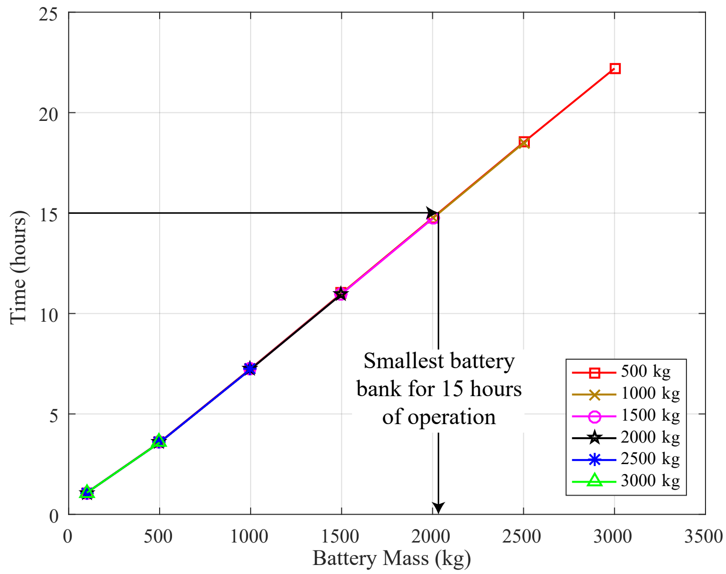

Figure 4.9: Maximum range of operation in kilometers travelled without recharging on 70% of the battery bank's charge as a function of the on-board battery bank mass for different SC masses (legend).

Energy savings due to regeneration as a function of SC mass are presented in Figure 4.10. The smallest increment of battery bank mass considered was 100 kg, leading us to conclude that the battery mass threshold for maximum regeneration is less than 100 kg given that the regenerated energy is almost fixed for all battery sizes over 100 kg.

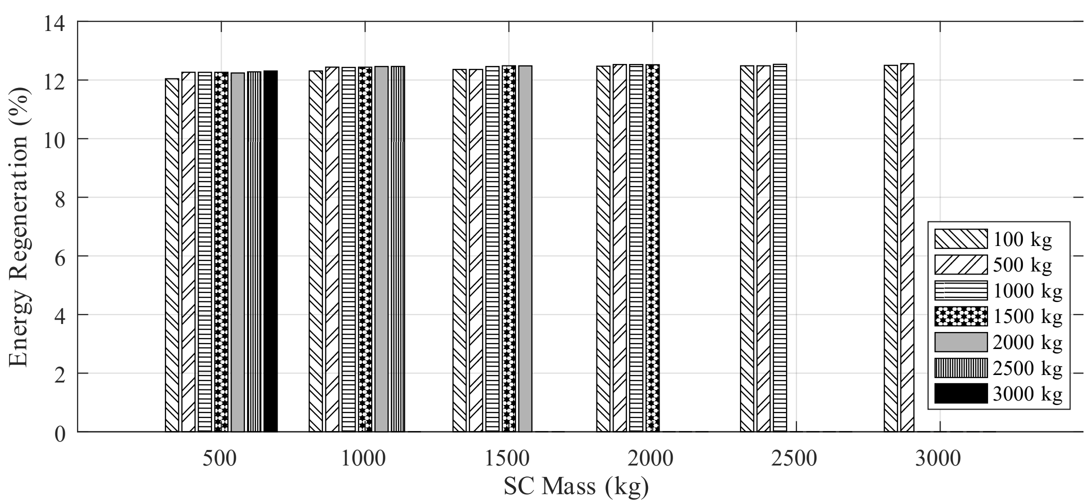

Figure 4.10: Energy regenerated as a percentage of net energy consumed as a function of the on-board ESS mix for a BSC hybrid British Class 150 DMU.

4.1.4 Fuel Cell - Battery Series Hybrid

In this section, the results of the FCB power train simulation for the given case study are presented and discussed. We begin by discussing single-trip plots followed by a discussion of plots generated for longer periods of operation. The results of this section are highly dependent on how much power each source can contribute. Note that the results with each locomotive fitted with a 20 kW FC will not be the same as results with each fitted with a 100 kW FC. A sensitivity analysis of how the power of the FC stack impacts key trip parameters is presented at the end of this section. For our trip analysis, we assumed that each DMU was powered by a 80 kW FC.

Figure 4.11 presents the power demand profile during the 45 minute round trip from Trehafod to Treherbert on the British Class 150 DMU assuming a 80 kW FC system in each DMU and a 3 tonne battery bank. The first thing to be noticed is that the battery power is free to fluctuate while the FC power is constant throughout the trip. The power from the FC system is controlled by a proportional controller that acts to sustain the charge of the battery bank. The fact that the FC is supplying full power through-out the trip means that the battery bank is below required charge levels throughout the trip.

With the absence of a SC bank, the job of storing regenerated energy falls to the battery bank. Figure 4.11 shows the times during which a mechanical brake was required to prevent the vehicle's speed from overshooting its desired value. We can see that the braking power needed is small when compared to the amount of regeneration power as presented in Figure 4.11.

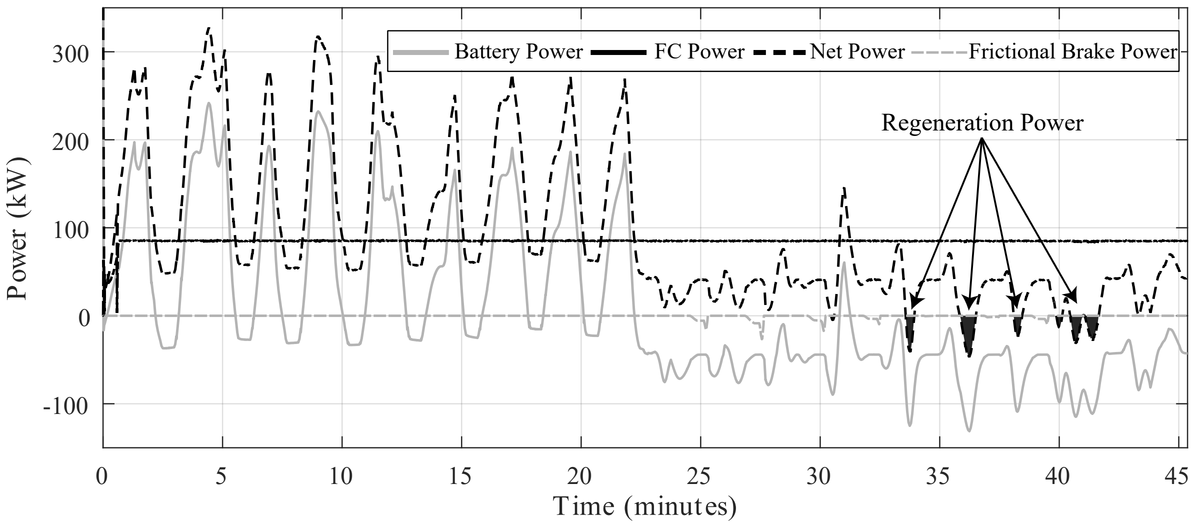

Figure 4.11: Trip power profile. The average FC power was limited to 80 kW in each DMU and the battery bank mass in each DMU was 3000 kg.

Figure 4.12 presents percentage change in the amount of hydrogen stored on-board the train as a function of trip time, assuming that each DMU is carrying 3 hydrogen tanks. In the same figure, battery SOC change is plotted. The small change in the battery bank's SOC can be attributed to its size at 3 tonnes and to the fact that the FC system is constantly charging the battery. We will demonstrate how battery size and SOC fluctuation are linked in later sections. Unlike the SOC plot, the hydrogen consumption plot cannot increase as hydrogen is not being regenerated.

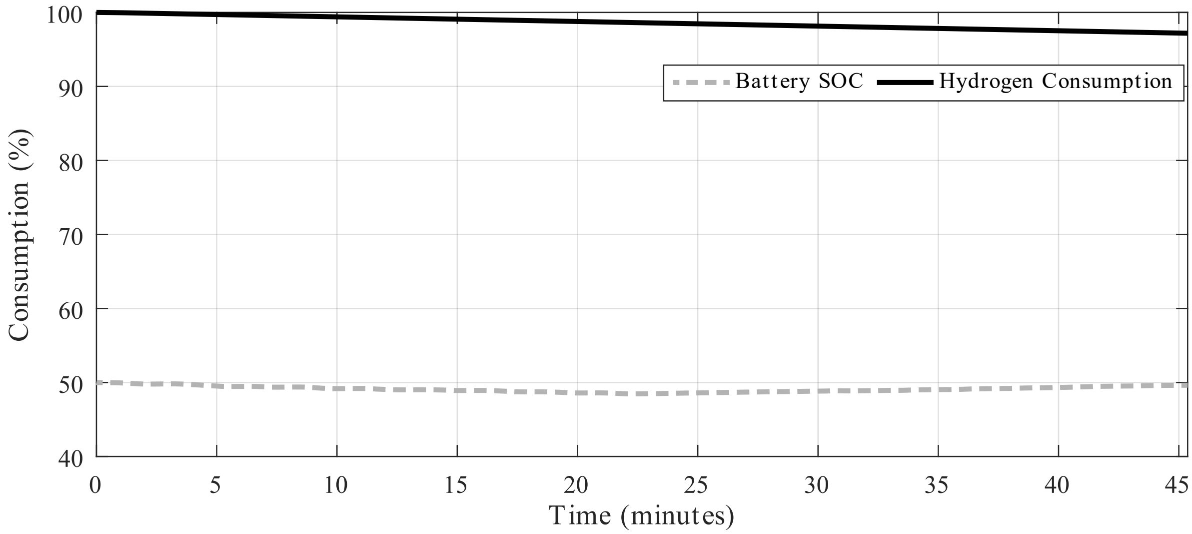

Figure 4.12: The battery bank's SOC, and the hydrogen consumption as a percentage change. The average FC power was limited to 80 kW in each DMU, the battery bank mass in each DMU was 3000 kg, and the hydrogen storage was limited to 3 tanks.

The mean trip powertrain efficiency for this simulation was 84.35%. This is an expected value since it represents the efficiency for the PMDC traction machine, the power electronics, and other powertrain inefficiencies. Figure 4.13 illustrates how the powertrain efficiency changes with trip time. Similar to the previous study, the powertrain is more efficient when operating in motoring mode than when operating in regenerative braking mode as Figure 4.13 illustrates.

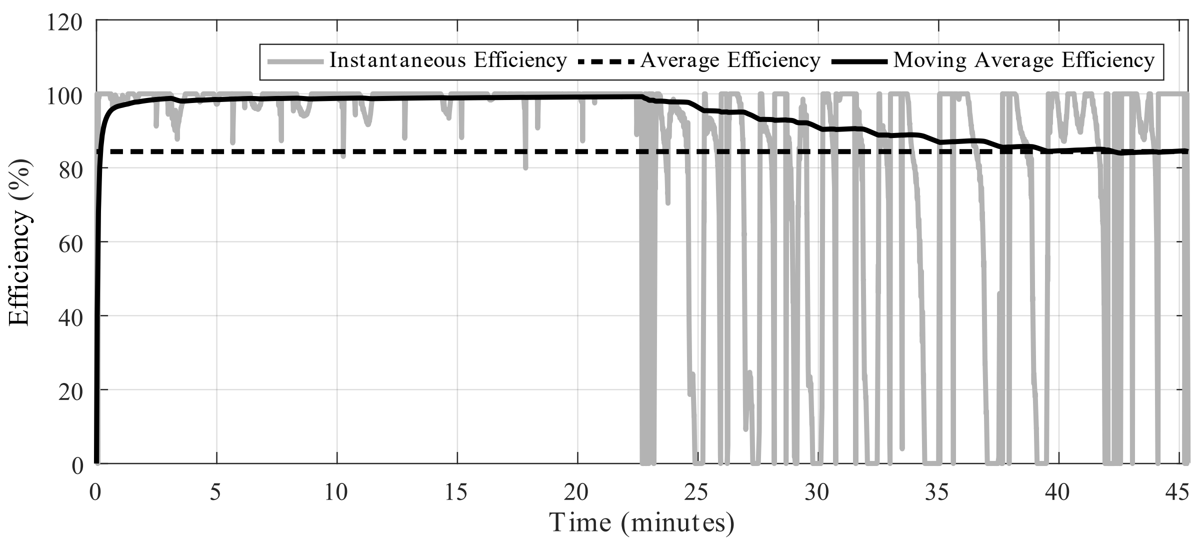

Figure 4.13: Powertrain efficiency excluding the FC stack efficiency. The average powertrain efficiency was 84.37%. The average FC power was limited to 80 kW in each DMU and the battery bank mass in each DMU was 3000 kg.

The above efficiency calculation does not account for the efficiency of the fuel cell system. This efficiency is an electromechanical efficiency. It is very important to include the efficiency of the FC system in our calculations. The electrochemical efficiency of the FC system for the chosen trip averaged at 64% as Figure 4.14 illustrates. This is perhaps the maximum achievable FC system efficiency. The FC system operated at such a high efficiency because it was supplying steady power. If the FC system was allowed to fluctuate more aggressively, its efficiency would drop dramatically. The overall efficiency of the entire system including the efficiency of the FC system is therefore 54%, a value that is similar to what is to be expected from a diesel-electric railway vehicle.

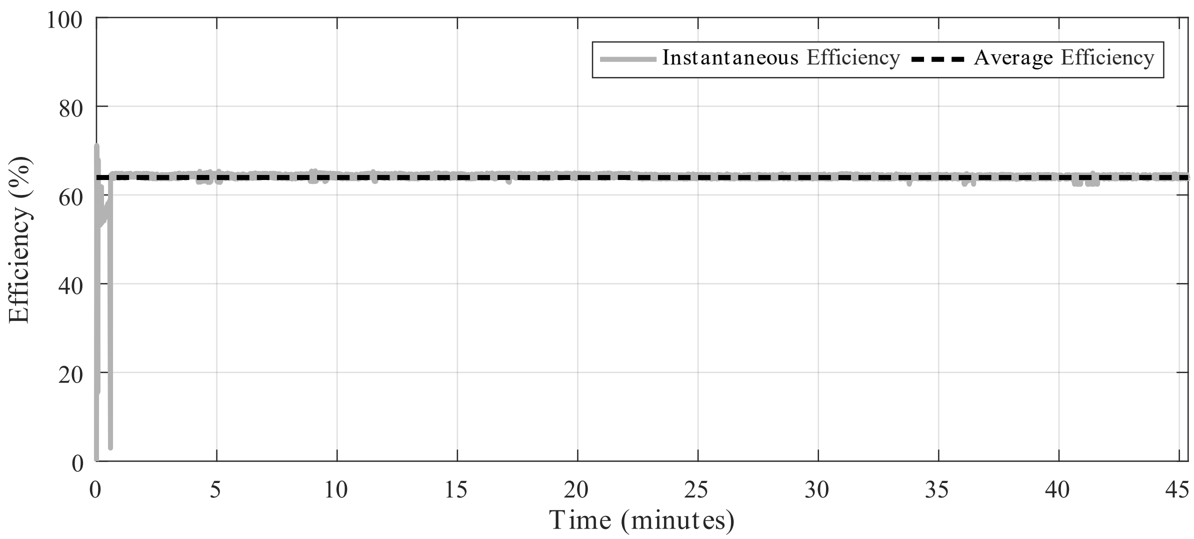

Figure 4.14: Fuel cell instantaneous and average efficiencies. The average FC power was limited to 80 kW in each DMU giving an average efficiency of 64%, the battery bank mass in each DMU was 3000 kg, and the hydrogen storage was limited to 3 tanks.

Fifteen hour work day A single-trip analysis cannot be the only analysis upon which feasibility decisions are made. After all, trains usually operate for hours every day which calls for the examination of performance parameters given a wider window of operation. The assumption that each DMU is powered by a 80 kW FC system is extended to this part of the study. This section assumes 15 hour work day.

By extending the window of operation to 15 hours, a total of 20 consecutive trips can be examined. For example, Figure 4.15 shows us that the 3 tank per DMU scenario presented in the previous section would be more than 50% depleted by the end of the 15 hour work day. It also shows that if each DMU carried just one tank of hydrogen, a tank refill would be needed after approximately 8 hours, almost twice a day. However, the fuel economy is independent of the number of tanks on-board the train. It depends on other factors, primarily the control system, battery bank size and SOC, and FC power limit. A 100 kW FC consumes more hydrogen than a 80 kW FC depending on the restrictions set by the control system. For this case, the fuel economy was found to be 0.112 tanks per hour or approximately 0.5 kg of hydrogen per round trip (55.6 km/kg).

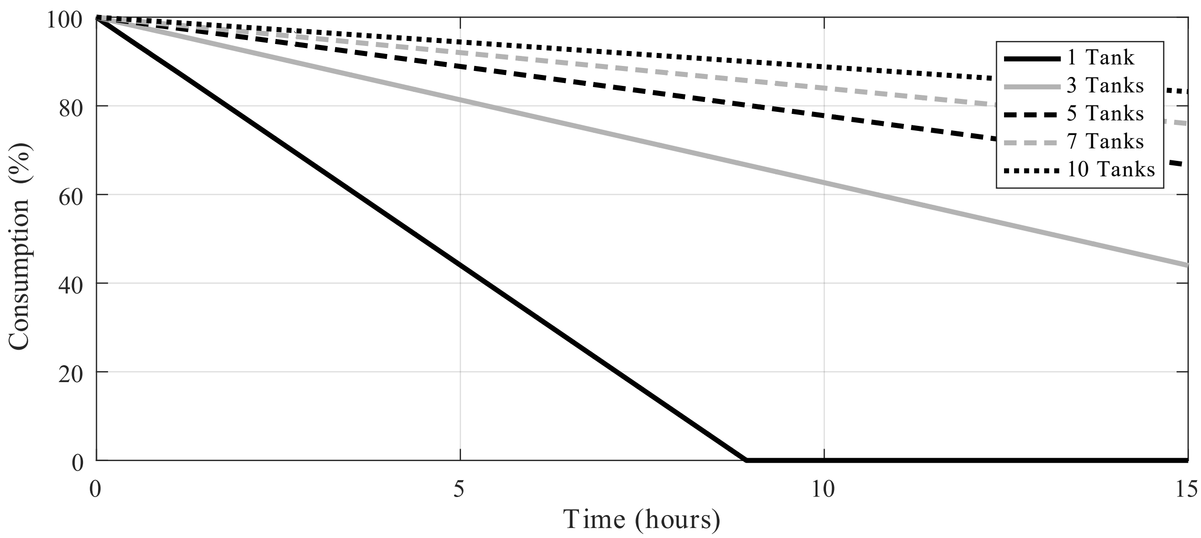

Figure 4.15: Hydrogen consumption for a per DMU storage of 1 tank, 3 tanks, 5 tanks, 7 tanks and 10 tanks after 15 hours of operation.

Extending the window of operation allows us to make better informed decisions on how the battery SOC changes. As Figure 4.16 demonstrates, the battery SOC change is linear and bounded. As long as the SOC does not reach any of its bounds at 0% or 100%, it linearly decreases or increases depending on the FC power limit and the bank's mass.

From the figure we can deduce that for a FC power limit of 80 kW in each DMU, any battery bank of mass less than 500 kg would need to be charged during the 15 hour operational window. It can be argued that a lighter, easily depleted bank can also be easily swapped, eliminating the time needed for charging.

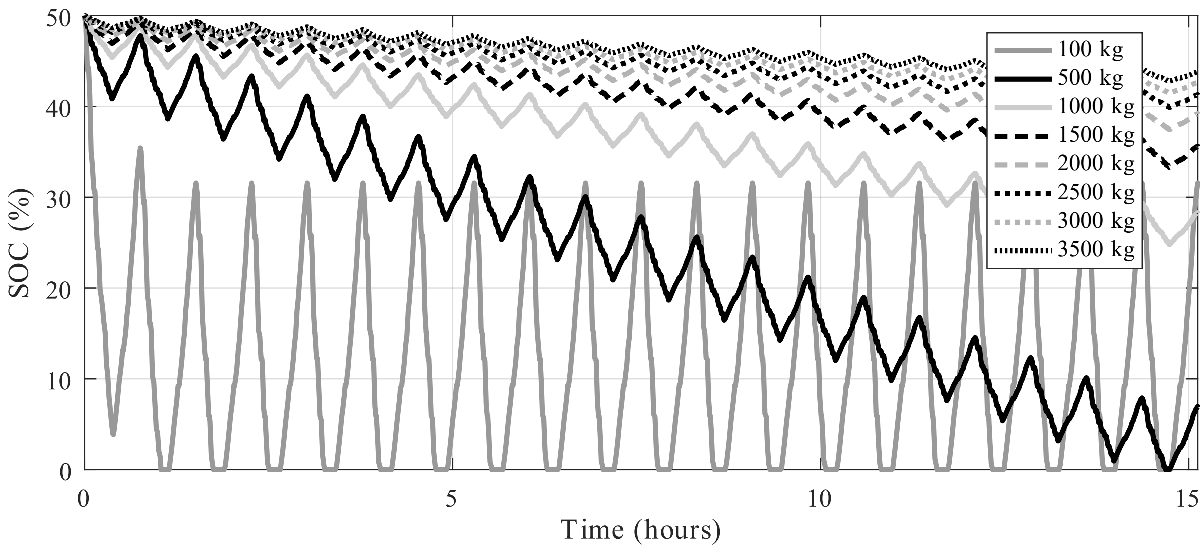

Figure 4.16: Battery SOC for a per DMU battery storage of 100 kg, 500 kg, 1 tonne, 1.5 tonnes, 2 tonnes, 2.5 tonnes, 3 tonnes, and 3.5 tonnes for 15 hours of operation.

We do not aim to answer the question of which is the better use of available space on-board the DMU. We only aim to present a set of feasible scenarios. For example, if cost is to be minimized, a choice between a higher number of tanks combined with a smaller battery bank versus the opposite would have to be made. This choice depends on the answer to the question of which is costlier, refueling a hydrogen tank or recharging a battery bank. The answer could be different if the aim is to minimize emissions. Life-cycle analysis of the manufacturing process of lithium-ion batteries, hydrogen tanks, and PEMFCs would determine which manufacturing process emits the most GHG. WTW analysis of hydrogen generation as compared to electricity generation for battery bank recharging would answer the question of which combination will do the most harm to the environment on the long run.

ESS Optimization study Similar to the BSC study discussed earlier, in this section we demonstrate how the energy storage mix on-board the FCB DMU impacts certain key parameters such as number of continuous operational hours, regenerated energy, and net SOC change. Again, this section assumes a 80 kW FC on-board each DMU although it will be demonstrated later how the results are fairly insensitive to the size and power limit of the FC stack. Figure 4.17 presents a two dimensional view of the ESS optimization problem that arises when deciding on energy storage allocation. The gray area in Figure 4.17 shows the ESSs combinations that are not allowed given the physical constraints mentioned earlier. The discrete ESS combinations selected for simulation are shown as dotted points in the same figure. The lightest combination considered for simulation is one where the hydrogen storage is 1 tank, and the battery mass is 100 kg.

Figure 4.17 also shows the mass constraints for each source for a 15 hour operational day. Any combination enclosed between the volume constraint line, the mass constraint line, the minimum battery mass constraint, and the minimum hydrogen mass constraint is a combination that would allow continuous operation for 15 hours while obeying the physical constraints. That region is our feasibility set. Simulation results will further determine how the energy storage mix on-board the DMU within that region impacts certain key parameters.

The low density of hydrogen makes using it in fixed mass applications a challenge. The more the hydrogen, the lighter the vehicle, and the more ballast is needed. This is not a problem with batteries. The more batteries the heavier the vehicle.

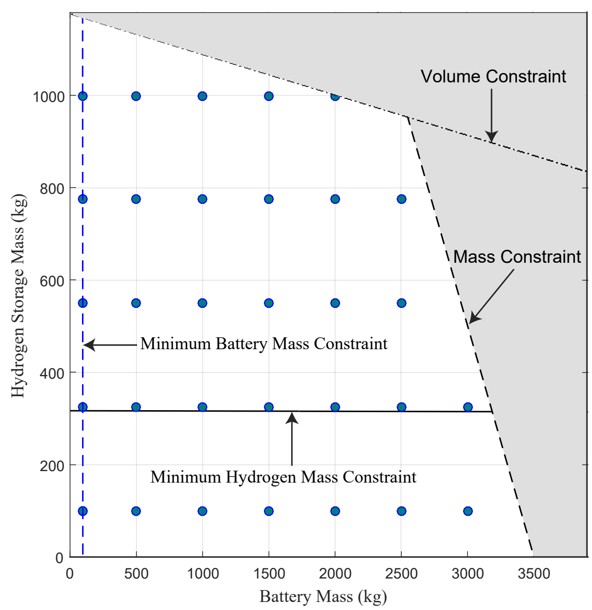

Figure 4.17: A two dimensional illustration of the ESS sizing optimization problem that highlights the cases considered for simulation. The ESS in this study is a FCB hybrid, and the physical constraints are for a British Class 150 DMU. The dotted circles represent the ESS cases selected for simulation.

Figure 4.18 presents the maximum hours of continuous operation without refueling as a function of the on-board hydrogen storage. It was found that the maximum range of travel without refueling was much more dependent on the on-board hydrogen storage than on the on-board battery storage. This is mainly due to the higher energy density of hydrogen in comparison to lithium-ion batteries.

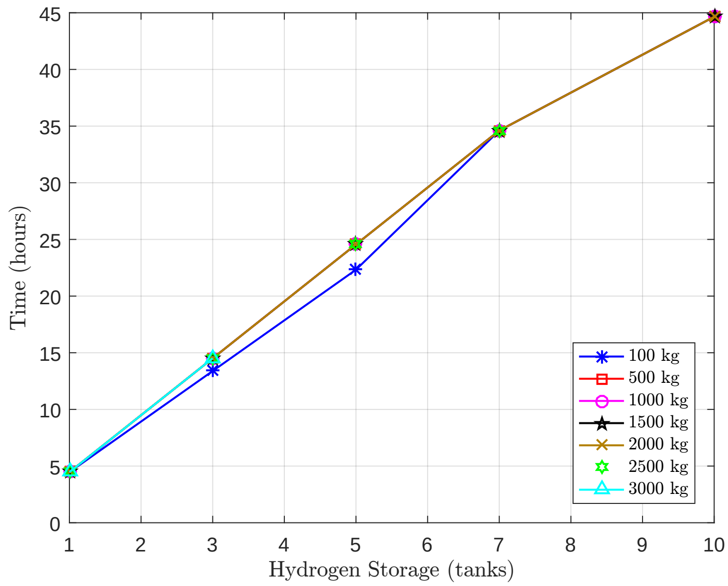

Figure 4.18: Maximum number of hours of operation without refueling as a function of the on-board hydrogen storage mass for a FCB hybrid British Class 150 motive unit for different battery bank masses (legend).

Figure 4.19 presents the percentage change in the battery bank's SOC per operational hour as a function of battery mass for different hydrogen tank numbers assuming that each motive unit had a 80 kW FC system as the prime mover. The figure shows that the battery bank's SOC is independent of the on-board hydrogen storage. Since the energy supplied by the battery bank is fixed, increasing the battery bank's mass by a factor decreases the hourly SOC change by the same factor as presented in the figure.

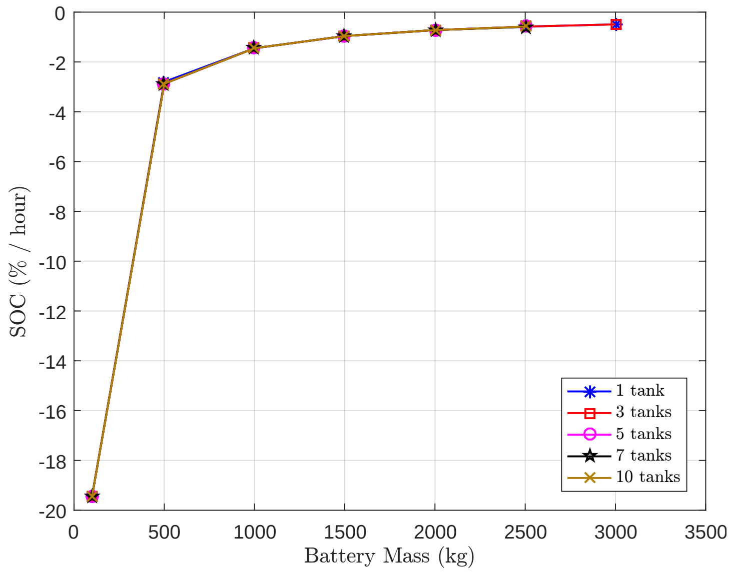

Figure 4.19: The battery bank's rate of loss of charge as a function of its mass for different hydrogen tank numbers assuming that each motive unit had a 80 kW FC system as the prime mover.

Energy savings due to regeneration as a function of battery mass for different hydrogen storage combinations are presented in Figure 4.20. We can observe that for all the ESS combinations considered, energy regeneration is fixed at approximately 12.2%. The smallest increment of battery bank mass considered was 100 kg, leading us to conclude that the battery mass threshold for maximum regeneration is less than 100 kg.

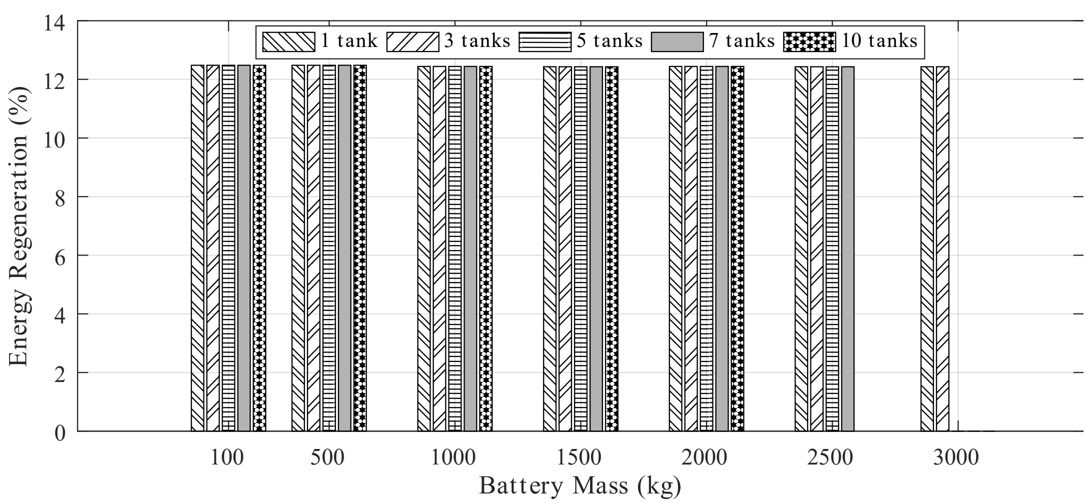

Figure 4.20: Energy regenerated as a percentage of net energy consumed as a function of the on-board ESS mix.

Sensitivity to FC power per DMU So far in our analysis, we have assumed a fixed FC maximum power of 80 kW. The FC system can adjust its power according to the battery bank's SOC but cannot exceed 80 kW. We now investigate how sensitive are the key trip parameters discussed earlier to changes to the maximum allowable FC power.

Figure 4.21 presents the results of the SOC sensitivity study. In this study, the battery bank's SOC was recorded at different battery masses and FC system powers. The 100 kg battery bank has a negative net SOC change for FC powers that are approximately less than 22 kW. Not only does it have a positive net SOC change for FC powers higher than 22 kW, the net change is relatively constant for most of the power range. This suggests that the battery bank is relatively insensitive to FC system power that are above a certain threshold. This is a testimony to the control system's robustness.

The wide gap between the 100 kg line and the 500 kg line as compared to the gaps between all the other lines suggests that at a certain battery mass threshold, the SOC change is somewhat insensitive to additional increases in the bank's mass. It also shows that anything over 500 kg will not have a significant net SOC change.

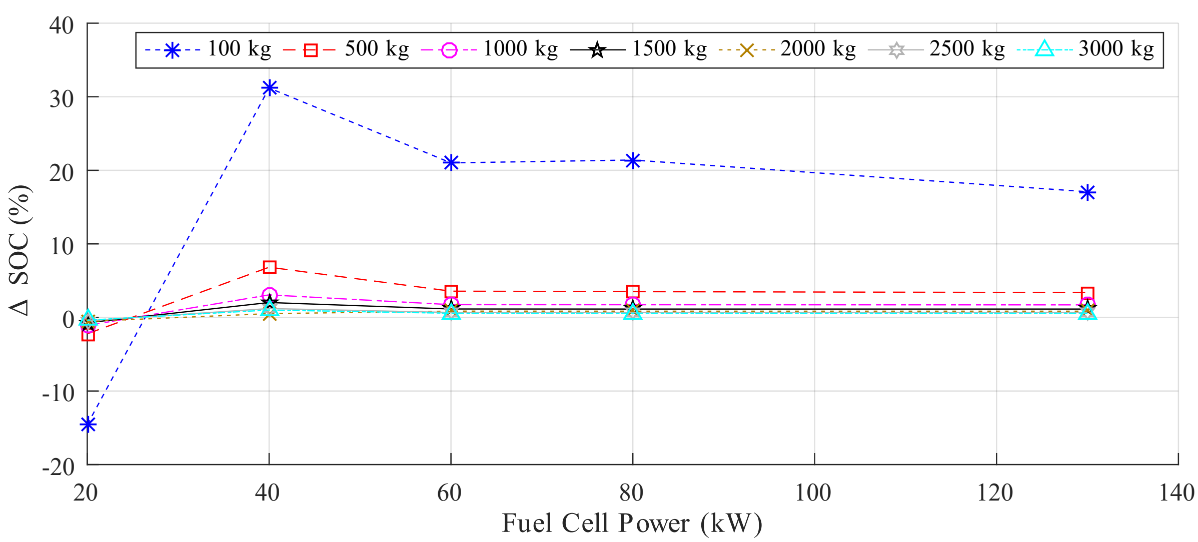

Figure 4.21: Battery bank SOC change per trip sensitivity to bank's mass (legend) and FC system power limit.

The efficiency of the FC system is a strong criteria when it comes to feasibility decisions. For this reason, Figure 4.22 is perhaps one of the most important figures. This is especially the case when the difference between the highest and the lowest efficiencies is almost 35%.

The figure shows that at lower FC powers, the FC system efficiency is higher than at higher powers. This is because higher power FC systems are more responsive to transients given the control system employed. A 130 kW system needs only to supply full power for 15% of the time needed for a 20 kW system to deliver the same energy. This means that the lower power FC system would be delivering rated power at maximum efficiency for longer periods of time (see Figure 4.14), while higher power systems would turn on and off more often as they supply too much power, which reduces the system's average efficiency.

As mentioned earlier, FC systems are most efficient when operating at rated power. Given that all the simulations presented in this thesis relied on the 100 kW Honda FCX stack, with lower powers being examined through limiting the power output of the same stack, efficiency levels should drop as lower FC powers are examined. By examining Figure 4.22 we can observe that this is true only when the FC power increases from 20 kW to 40 kW for battery masses of over 500 kg. For battery masses of 500 kg and lower, the trend reverses, and the stack efficiency drops from a higher value at 20 kW to a lower value at 40 kW. This is because the smaller the battery bank is, the more aggressively its SOC will fluctuate given the same testing conditions (trip). Aggressive fluctuations in battery SOC will force to the FC system to react accordingly. A higher power FC system will react even more aggressively as it supplies a lot of power for a very short time.

By examine the same figure, we can also observe that the stack efficiency drops dramatically after 40 kW for all battery masses, suggesting that the best efficiency levels can be obtained for FC powers equal to or less than the average trip power which is somewhere between 40 kW and 60 kW.

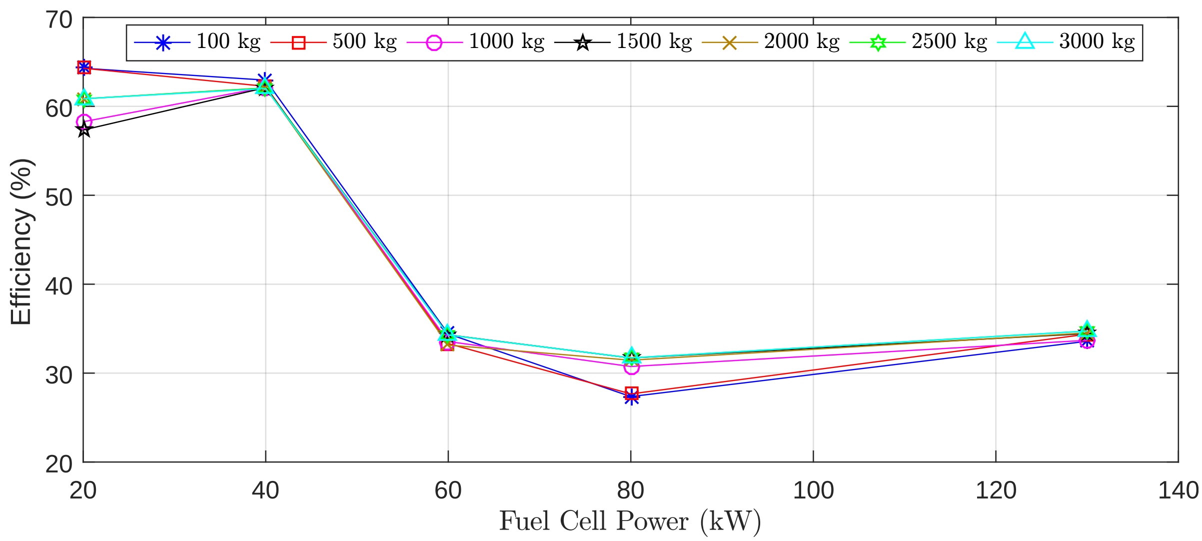

Figure 4.22: The sensitivity of the mean trip FC efficiency to changes in FC power and battery bank mass (legend).

Figure 4.23 shows how sensitive fuel economy in tanks per hour is to FC system power and battery bank mass. If there were no system to control the power output of the FC stack, and each stack was allowed to operate at its maximum power for the same time period, then the higher FC power would correspond to more energy delivered and more hydrogen consumed. This, however, is not the case. The system employed to control the power output of the FC system has one goal: to maintain the battery bank's SOC. This means that the FC system has to provide the average trip power.

For FC powers less than the average trip power, fuel economy increases with stack power. This can be observed as the FC power is increased from 20 kW to 40 kW. For FC powers higher than the average trip power, the power provided by the FC system will fluctuate according to the battery bank's SOC which should theoretically lead to higher fuel economies due to the reduced stack efficiency. However, if we observe Figure 4.23, we will see that for FC powers higher than 40 kW, the fuel economy fluctuates around an average of approximately 0.16. A reasonable generalized fuel economy is 0.16 tanks per hour, or 1 tank every 6 hours and 15 minutes as deduced from Figure 4.23. A more robust control system would not result in such fluctuations, some as extreme as 0.19 tanks per hour at 80 kW FC power.

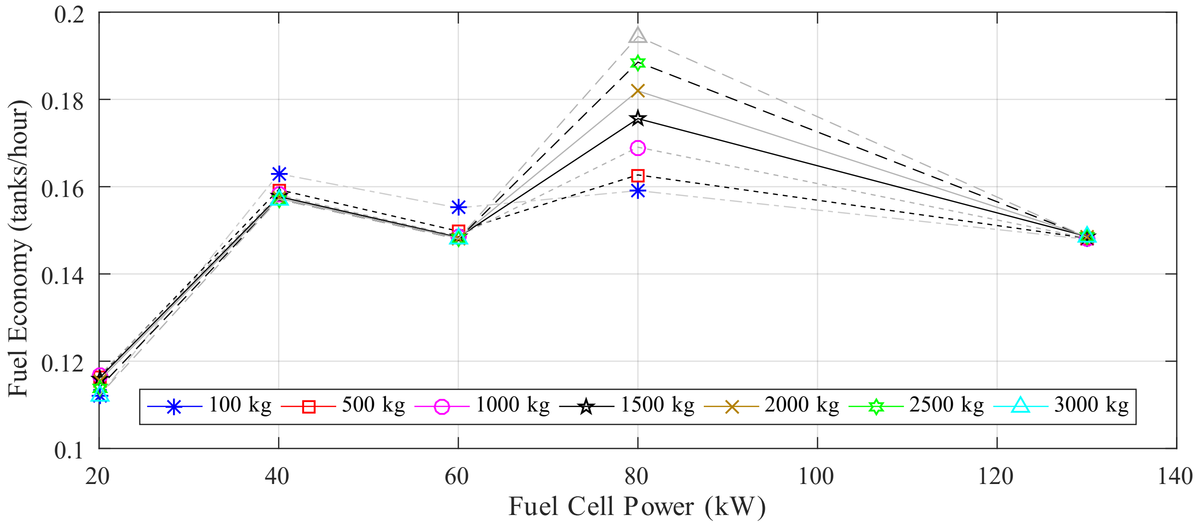

Figure 4.23: The sensitivity of the hourly rate of hydrogen consumption to changes in FC power and battery bank mass (legend).

Finally we examine how sensitive energy regeneration is to changes in battery mass and FC system power. We had previously shown that energy regeneration is not sensitive to increments in battery mass above a certain threshold value. It should come as no surprise that energy regeneration is not in any way dependent on the FC system, since FCs do not store regenerated energy. It also seems that the minimum required battery bank mass for full regeneration is below 100 kg.

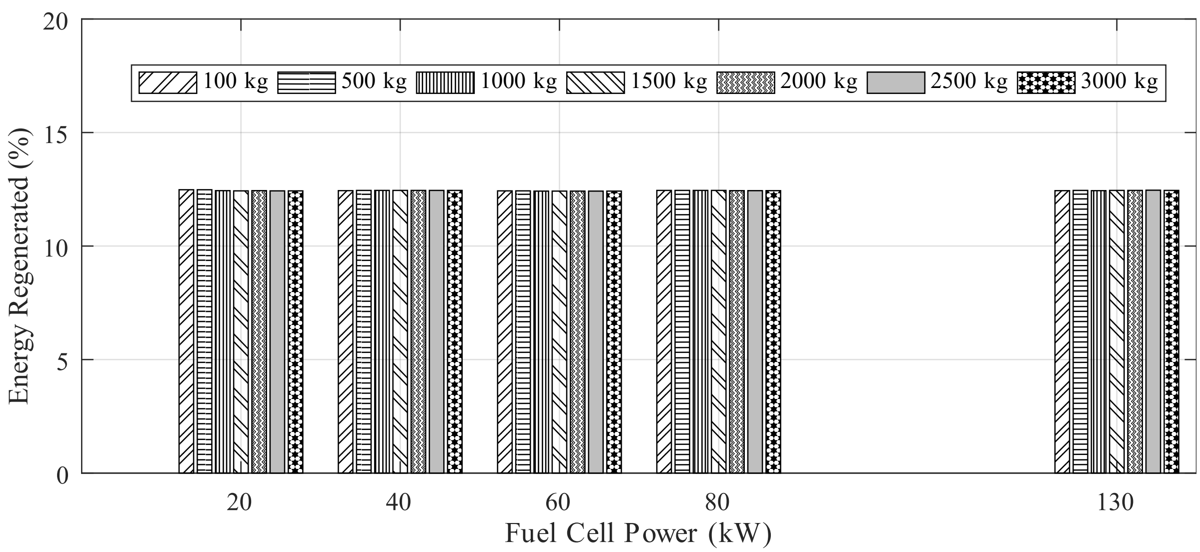

Figure 4.24: The sensitivity of the regenerated energy as a percentage of the net energy to changes in FC power and battery bank mass.

4.2 Intercity 125: King's Cross to Newcastle

4.2.1 Train Description

British Class 43 is a locomotive that runs on a 1600 kW diesel engine. Two of these units hauling 6-7 Mark 3 carriages form the Intercity 125 train. Each locomotive has two powered two-axle bogies as shown in Figure 4.25. The case considered in this study is one where a trainset is formed of two locomotives and can carry 600 passengers seated. Table 4.2 contains the train specifications. The specifications for the British Class 43 locomotive can be found in the appendix. The space available for hybrid ESS installation was assumed to be approximately 20 tonnes at 36000 Liters. This assumption was based on the combined mass and volume of the diesel engine at 12 tonnes, and the radiator and fuel compartment at 4 tonnes each.

Table 4.2: The specifications of the Intercity 125 train as a single rigid body.

Physical Specs	
Mass	404 tonnes
Rotational Allowance	15 %
Davis Equation (kN)	$3.22 + 0.1127v(m/s) + 0.0078v^2(m/s)$
Performance Specs	
Maximum Speed	200 km/h

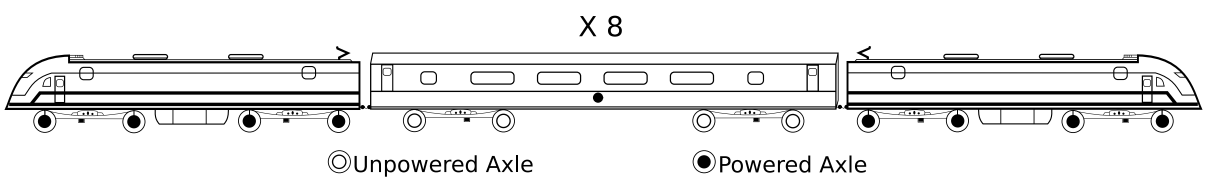

Figure 4.25: Intercity 125 train consist: two Class 43 locomotives hauling 8 Mark 3 carriages

4.2.2 Route Description

The route chosen for this study is the 432 kilometer route from London's King's Cross Station to Newcastle in the UK. It was the chosen route for our intercity rail study. As the train leaves the King's Cross station, it gains 40 meters in elevation only to end up 15 meters below London's altitude after 100 km. The net elevation change in 432 kilometers is less than 5 meters (see Figure 4.26), meaning that both stations are at approximately the same elevation level. Peak to peak elevation change is slightly over 80 meters with a maximum gradient of 10 meters per kilometer or 1%.

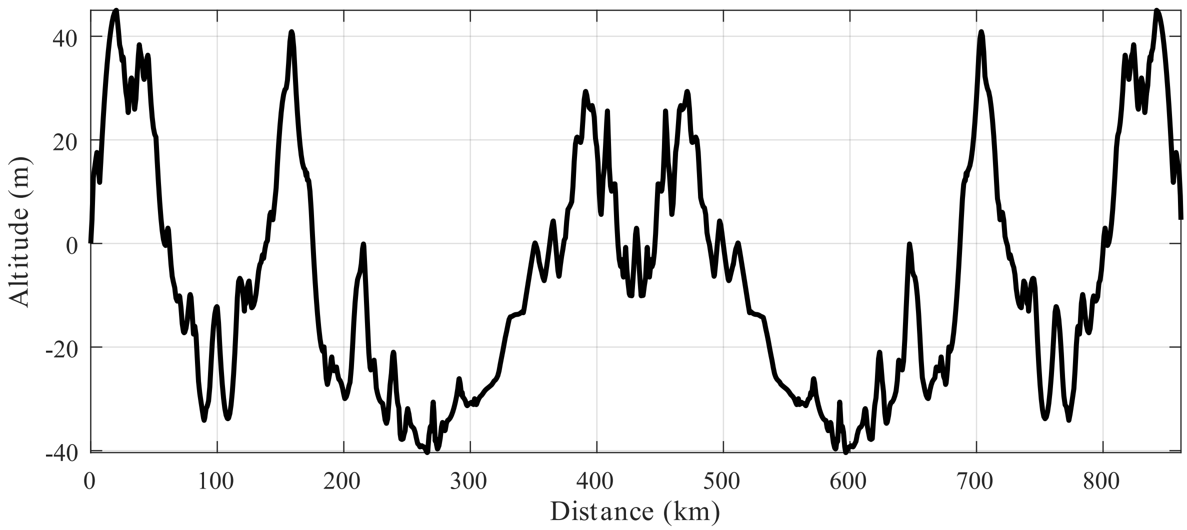

Figure 4.26: Intercity 125 Train Velocity Profile: London's King's Cross to Newcastle Round-trip.

As illustrated in Figure 4.27, the train makes 2 stops between King's Cross Station and Newcastle resulting in a one way trip time of approximately 160 minutes. Unlike the previous case study, in this case study the train is capable of reaching its top speed of 200 km/h assuming a fast as possible trajectory as computed using methods discussed in Section 3.3.

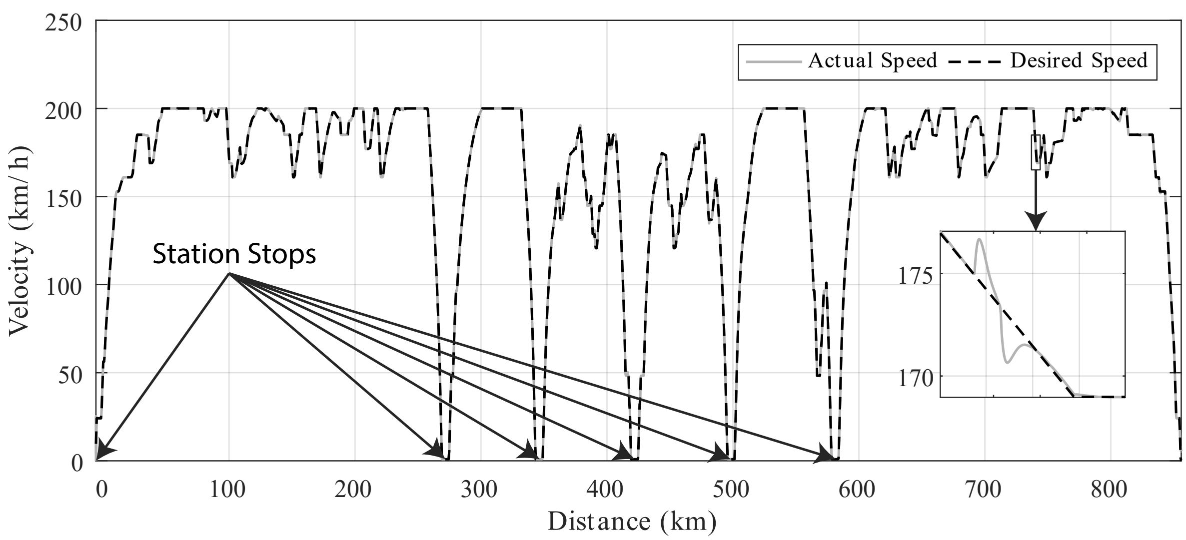

Figure 4.27: Intercity 125 Train Velocity Profile: King's Cross to Newcastle. The average FC power was limited to 400 kW in each Class 43 locomotive and the battery bank mass to 5 tonnes. The inset plot highlights the perturbation that occurs when the system changes the mode of operation from motoring mode to regenerative braking mode and back to motoring again.

4.2.3 Battery - Supercapacitor Parallel Hybrid

In this section, the results of the BSC power train simulation for the given case study are presented and discussed. Unlike the previous case study, this case study presents a trip that is long enough for single-trip analysis to be sufficient. Another reason for not examining longer durations is that the best range achieved relying on the on-board ESS was less than 100% of the full round trip. Similar to the previous BSC study, the results of this section are highly dependent on the mass of each source. A sensitivity analysis of how the ESS mix impacts key trip parameters is presented at the end of this section.

The results of the conducted simulations demonstrate that battery technology can be successfully employed in heavy vehicles just like they are in light vehicles. Figure 4.28 presents the power demand profile during the 318 minute round trip from London's King's Cross Station to Newcastle on the Intercity 125 assuming a 16.5 tonne battery bank in each locomotive and two and a half tonne SC bank. The trip shown in the figure was powered by two Class 43 locomotives, each containing a battery bank of 609,525 UPF454261 lithium-ion cells arranged in 1,505 parallel branches of 405 series-connected cells each, and a supercapacitor bank of 5,000 BCAP4500 SC units arranged in 9 parallel branches of 526 series-connected capacitors.

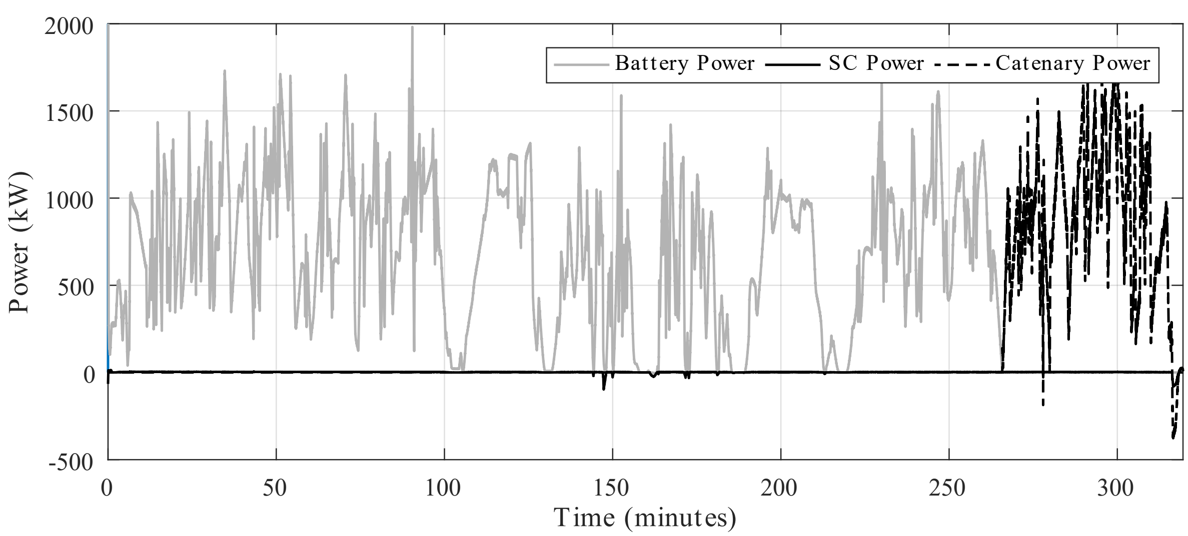

Figure 4.28: Intercity 125 Train Velocity Profile: London‘s King's Cross to Newcastle Round-trip.

Similar to the previous BSC case study, the battery bank is capable of providing all the transient power demand, making the SC bank unnecessary in motoring mode. On the other hand, the SC bank overtakes the battery bank when regeneration is needed. It is also noticeable that the train spends the majority of the trip in the motoring mode, making regeneration a less important feature. The figure also shows the point in time when the battery bank is depleted and the power from the catenary is required.

Examining an electric railway vehicle's fuel economy is essential to any feasibility study. At approximately $ 4.3 - 5 million USD per kilometer [64], on-board ESS must significantly reduce the required infrastructure for discontinuous electrification to be feasible. Figure 4.12 presents percentage change of the ESS stored on-board the train as a function of trip time. The first thing to be noticed is the almost linear fashion by which the battery bank loses its charge. Since batteries should not be overly charged or overly depleted as mentioned in Section 2.4, the battery SOC is only allowed to swing between 80% to 10% using only 70 % of its charge. Although the SC bank loses slightly over 20% of its initial charge, it is important to remember that for this example trip we used a very small SC bank.

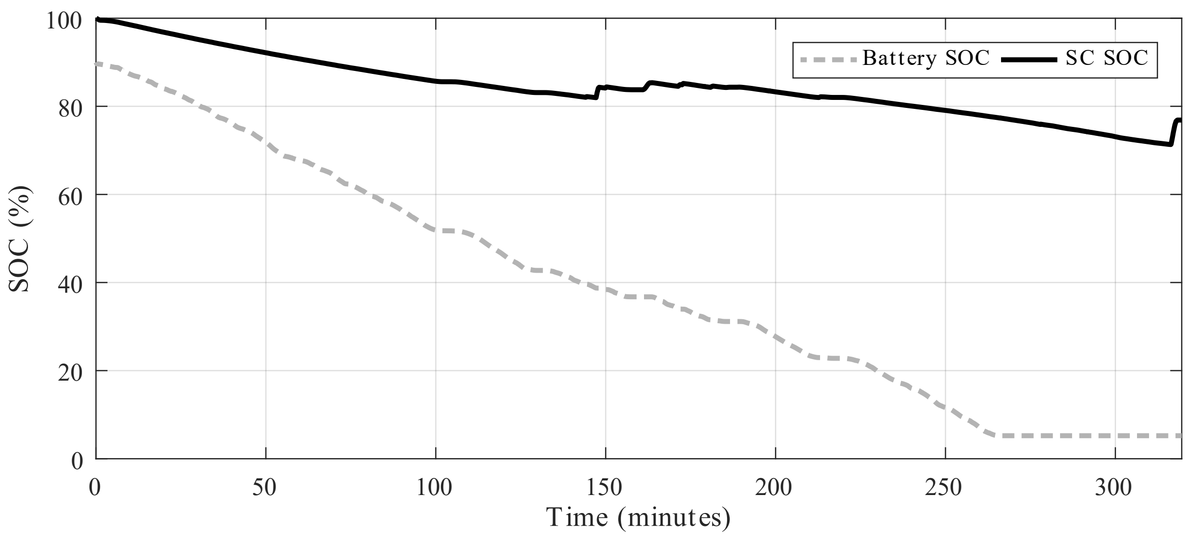

Figure 4.29: Intercity 125 Train Velocity Profile: London's King's Cross to Newcastle Round-trip.

The mean trip powertrain efficiency for this simulation was 86%. This is very close to the 84% efficiency obtained in the previous case study. This is expected since both models are made up of the same powertrain components. Figure 4.30 illustrates how the powertrain efficiency changes with trip time.

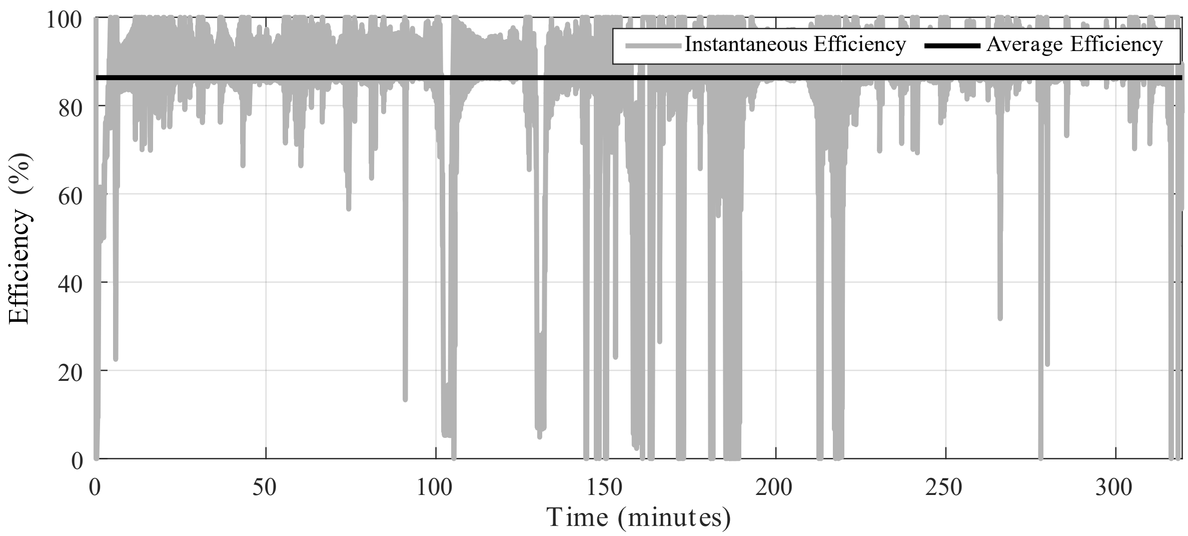

Figure 4.30: Powertrain efficiency which averaged at 86%.

ESS Optimization study In this section we demonstrate how the energy storage mix on-board the locomotive impacts certain key parameters such as the maximum catenaryless range of travel in kilometers, regenerated energy, and net SOC change.

Figure 4.31 presents a two dimensional view of the ESS optimization problem that arises when deciding on energy storage allocation. Following the same steps in the previous study, the first step is to determine the railway vehicle's physical constraints. The gray area in Figure 4.31 shows the ESSs combinations that are not allowed given given the volume and mass constraints of the vehicle. Similar to the Trehafod to Treherbert BSC study presented earlier, the volume constraint line and the mass constraint line do not intersect. The density of both the SC and the battery is more than one, which is why the mass constraint becomes the only physical constraint. A fact that is highlighted in Figure 4.31. The discrete ESS combinations selected for simulation are shown as dotted points in the same figure. The lightest combination considered for simulation is one where the SC bank mass is 2 tonnes, and the battery mass is 500 kg.

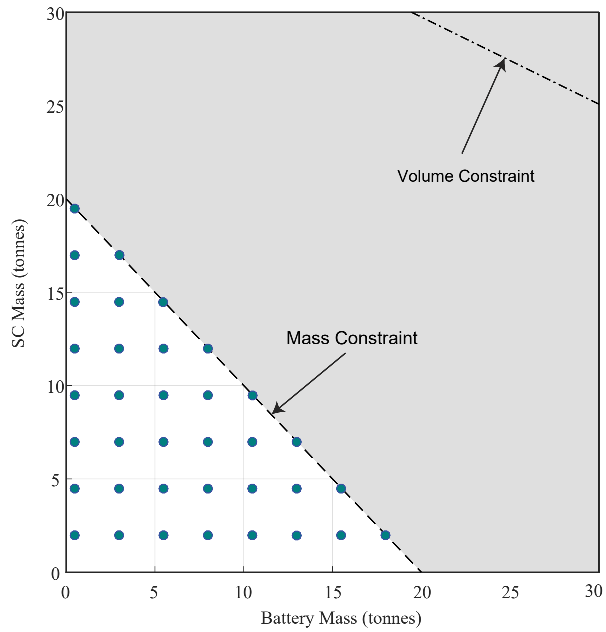

Figure 4.31: A two dimensional illustration of the ESS sizing optimization problem that highlights the cases considered for simulation. The ESS in this study is a BSC hybrid, and the physical constraints are for a British Class 43 locomotive. The dotted circles represent the ESS cases selected for simulation.

Figure 4.32 presents the maximum range of travel in kilometers without refueling as a function of the on-board battery mass. It was found that the maximum range of travel without refueling was much more dependent on the on-board battery storage than on the on-board SC storage. This is mainly due to the higher energy density of lithium-ion batteries in comparison to SCs.

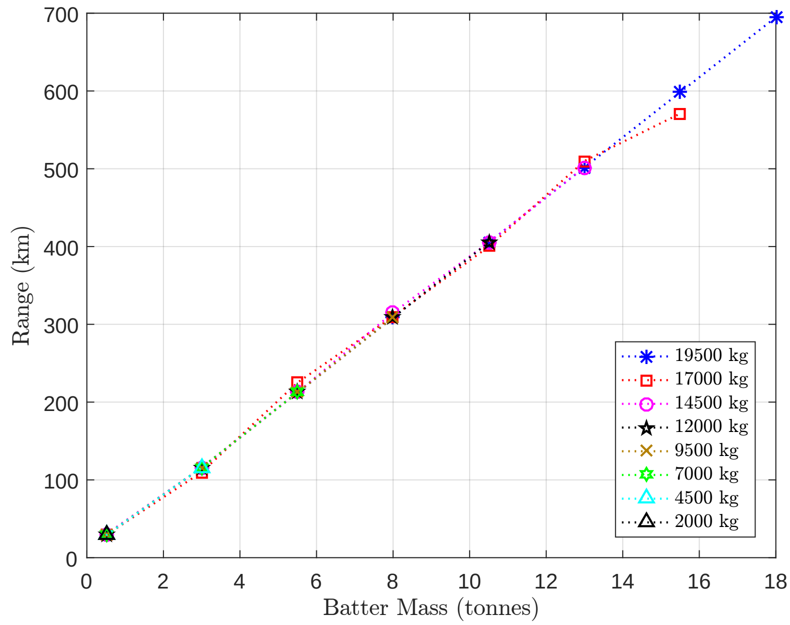

Figure 4.32: Maximum range of operation in kilometers traveled without recharging on 70% of the battery bank's charge as a function of the on-board battery bank mass for different SC bank sizes.

Energy savings due to regeneration as a function of battery mass are presented in Figure 4.33. The smallest increment of battery bank mass considered was 500 kg, leading us to conclude that the battery mass threshold for maximum regeneration is less than 500 kg.

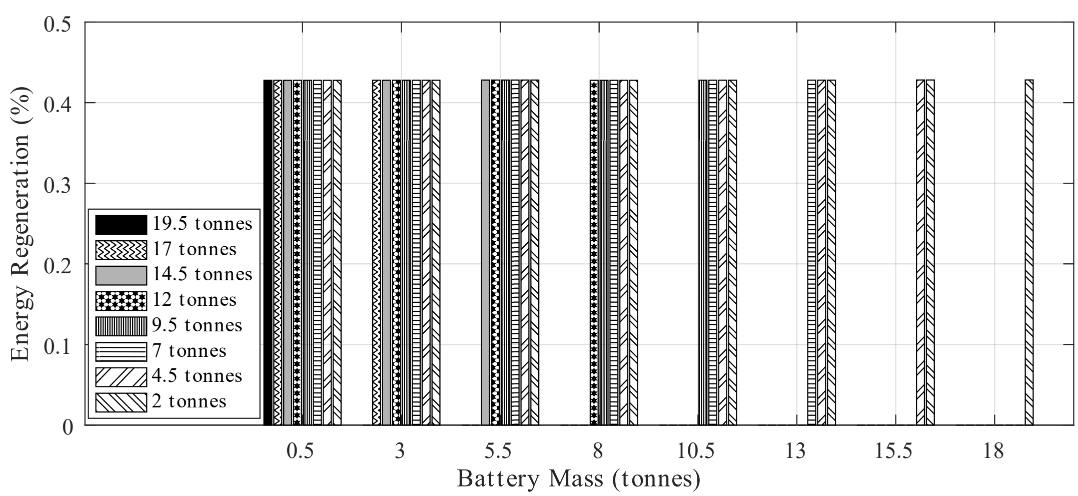

Figure 4.33: Regenerated energy as a percentage of net energy consumed as a function of the on-board ESS mix.

4.2.4 Fuel Cell - Battery Series Hybrid

In this section, the results of the FCB power train simulation for the given case study are presented and discussed. Similar to the BSC study, this case study presents a trip that is long enough for a single-trip analysis to be sufficient. Yet, analysis for longer durations are included for completeness purposes. All the results in this section assume that each British Class 43 locomotive is powered by eight 100 kW Honda FCX FC stacks and carries a 5 tonne battery bank to handle transient power demands. A sensitivity analysis of how the power of the FC stack impacts key trip parameters was not conducted. Instead, we extend the conclusions of the sensitivity analysis conducted in the Trehafod to Treherbert case study to this case study.

Figure 4.34 presents the power demand profile during the 318 minute round trip from London's King's Cross Station to Newcastle on the Intercity 125. Similar to the results presented in Subsection 4.1.4, the battery power fluctuates aggressively. The power from the FC system is controlled by a proportional controller that acts to sustain the charge of the battery bank. The fact that the FC power is fluctuating, although slightly, means that there is potential for FC stack downsizing.

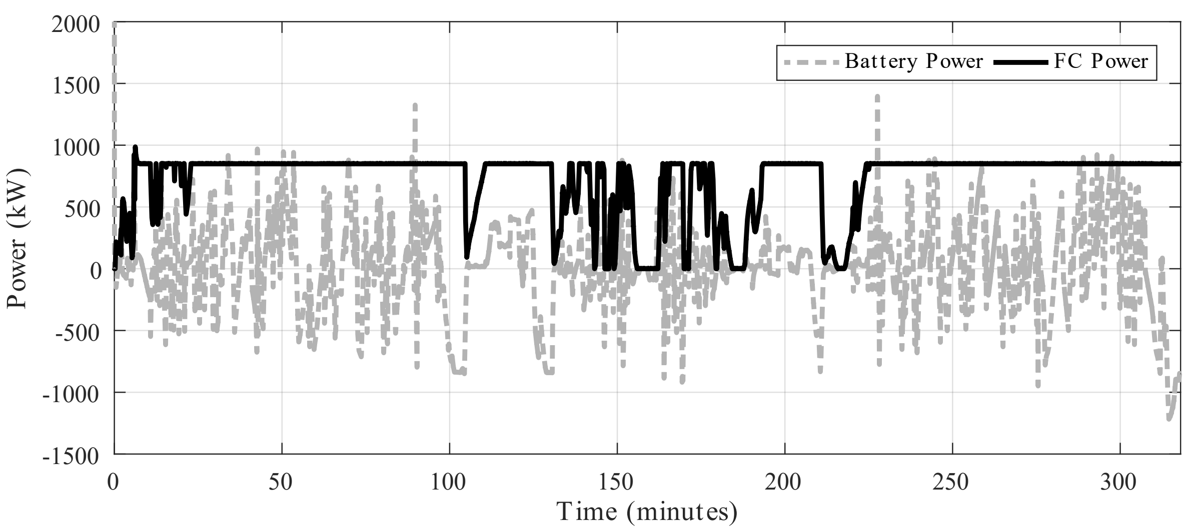

Figure 4.34: The power supplied by the FC system, and the battery bank. The average FC power was limited to 800 kW in each Class 43 locomotive and the battery bank mass to 5 tonnes.

For an in depth analysis, it is perhaps best to examine the power demand profile of each source at a much smaller time scale. Figure 4.35 presents the power demand profile of both sources starting at minute 144 to minute 154 in the 318 minute trip. In this time span, the power from the FC system fluctuates most aggressively as compared to the rest of the trip. A closer look at minute 146 reveals that a sudden power drop was encountered. By comparing both power demand plots at minute 146, we can observe how much faster the battery bank reacts. The fact that the FC system is turned off for the duration of slightly less than 2 minutes including a minute during which the battery power profile was negative shows us that the system was in regeneration mode from minute 146 to 147. At minute 147, the battery power profile is positive indicating that the system is in motoring mode, but the FC system was slow to react as intended.

Another region of interest is the region between minute 151 and 152. We can see that the FC system is providing constant full power while the battery bank's power makes a massive swing going up to 800 kW and down to -800 kW. This proves that there was a significant drop in power demand by the traction machines and all the FC power had to be dumped into the battery bank.

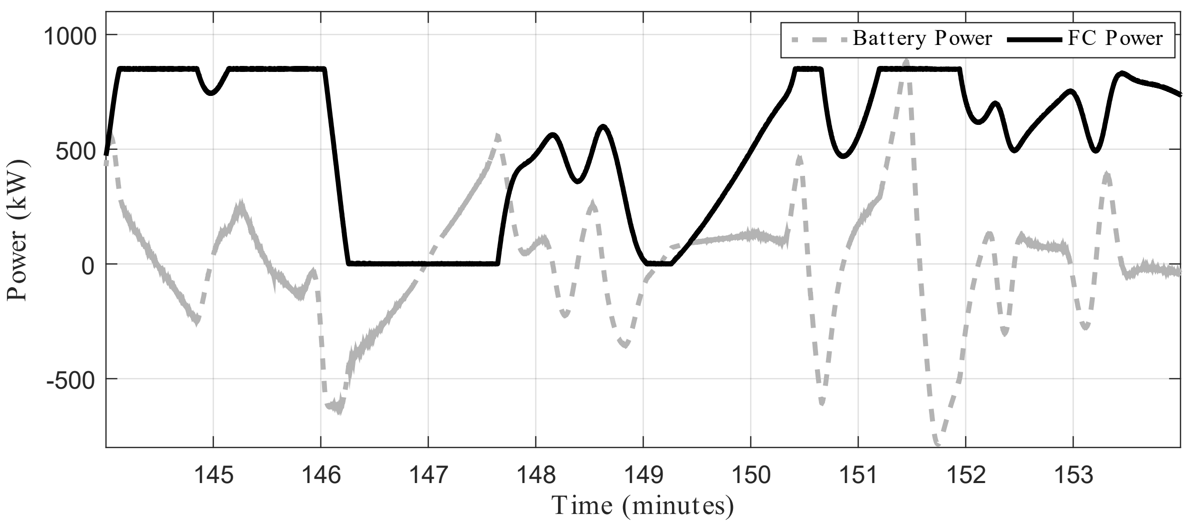

Figure 4.35: The power supplied by the FC system, and the battery bank for a 10 minute period starting at minute 144 to minute 154.. The average FC power was limited to 800 kW in each Class 43 locomotive and the battery bank mass to 5 tonnes.

Figure 4.36 shows how the powertrain efficiency was unaffected throughout all the conducted simulations presented in this thesis. The average powertrain efficiency of 86.5% is very similar to the values obtained for the BSC (Figure 4.30) study of the same case study, as well as the BSC and FCB (Figure 4.13) studies of the Trehafod to Treherbert case study.

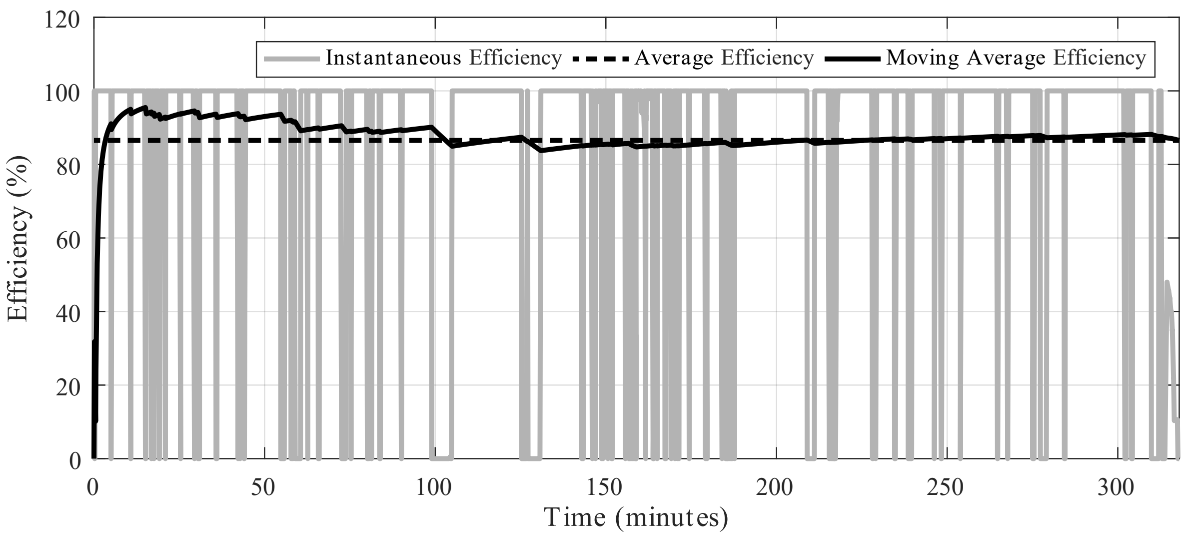

Figure 4.36: Powertrain efficiency excluding the FC stack efficiency which averaged at 86.521%. The average FC power was limited to 800 kW in each Class 43 locomotive and the battery bank mass to 5 tonnes.

FC hybrids have worse efficiency levels when compared to battery or SC hybrids. The overall efficiency of the system is the product of the powertrain efficiency and the FC system efficiency. As discussed earlier, the powertrain efficiency is almost fixed for all simulations at around 85%-86%. For this case study, the average FC system efficiency was observed to be 54.15%. If the efficiency of converting hydrogen and oxygen to electrical energy is 54.15%, and the efficiency of converting that electrical energy to mechanical energy at the wheel/rail interface is 86.5%, then the overall efficiency of the system is 46.8% which is almost half of the BSC system efficiency for the same case study.

Perhaps the most important aspect of any vehicle is its fuel economy. Figure 4.12 presents percentage change in the amount of hydrogen stored on-board the train as a function of trip time, assuming that each locomotive is carrying 86 hydrogen tanks. In the same figure, battery SOC change is plotted. The small change in the battery bank's SOC can be attributed to its size at 5 tonnes and to the fact that the FC system is constantly charging the battery. We will demonstrate how battery size and SOC fluctuation are linked in later sections. Unlike the SOC plot, the hybrogen consumption plot cannot increase as hydrogen is not being regenerated.

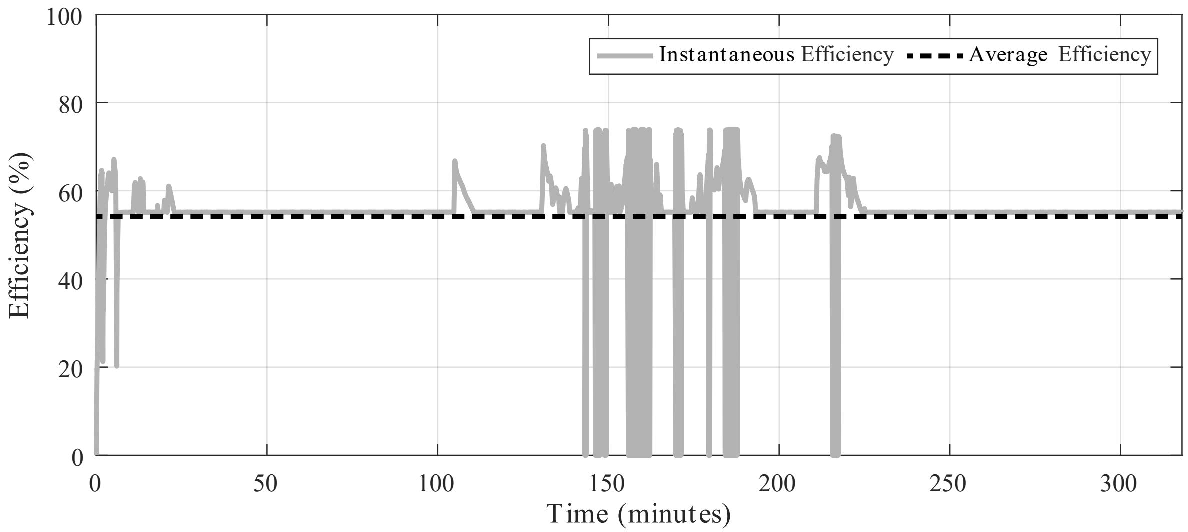

Figure 4.37: Fuel cell instantaneous and average efficiencies. The average FC efficiency for the trip was 54.15%. The average FC power was limited to 800 kW in each Class 43 locomotive and the battery bank mass to 5 tonnes.

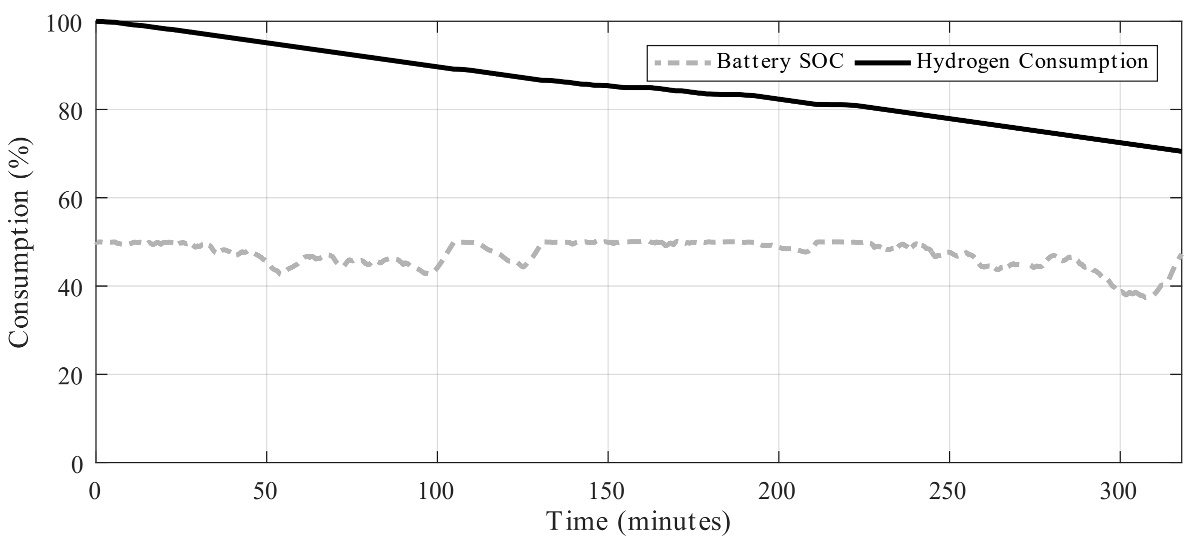

Figure 4.38: The battery bank's SOC and the hydrogen fuel economy as a percentage change. The average FC power was limited to 800 kW in each Class 43 locomotive, the battery bank mass to 5 tonnes, and the hydrogen tanks to 86.

Fifteen hour work day As mentioned earlier, single-trip analysis presents a restricted view of system performance. By extending the window of operation to slightly less than 16 hours, a total of 3 consecutive trips can be examined. For example, Figure 4.39 shows us that the 86 tank per locomotive scenario presented in the previous section would be approximately 35% depleted by the end of the 16 hour work day. The fuel economy is independent of the number of tanks on-board the train. It depends on other factors, primarily the control system, battery bank size and SOC, and FC power limit. For this case, the fuel economy was found to be 1.9 tanks per hour or approximately 56 kg of hydrogen per round trip per locomotive.

Extending the window of operation allows us to make better informed decisions on how the battery SOC behaves. As Figure 4.39 demonstrates, the net battery SOC change is linear and bounded. As long as the SOC does not reach any of its bounds at 0% or 100%, it linearly decreases or increases depending on the FC power limit and the bank's mass. From the figure we can deduce that for a FC power limit of 800 kW in each locomotive, a 5 tonne battery bank would lose 10% every 3 round trips.

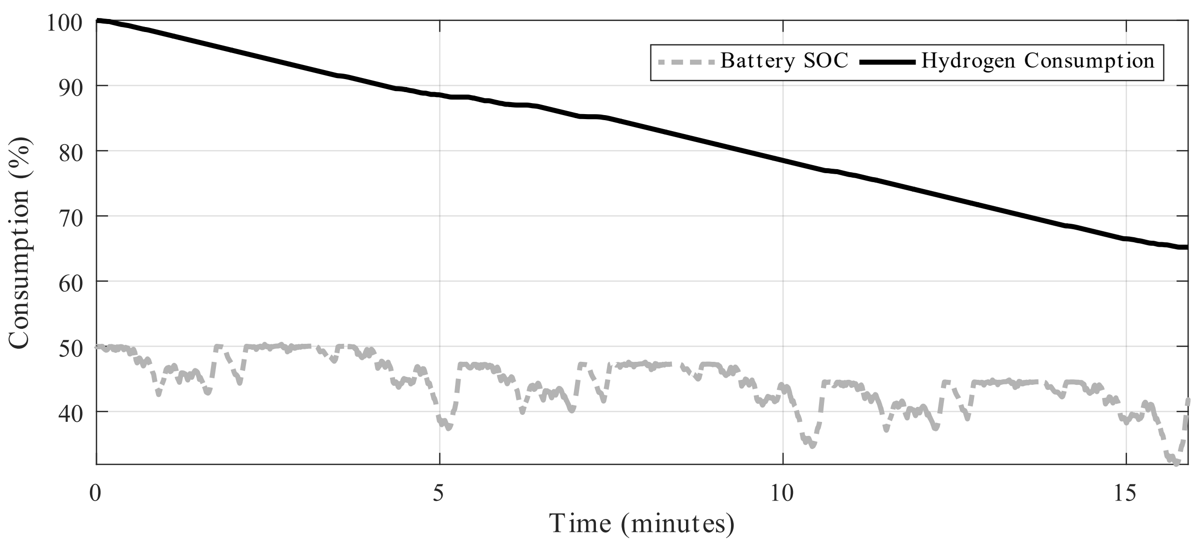

Figure 4.39: The battery bank's SOC and the hydrogen fuel consumption as a percentage change for 3 consecutive trips. The average FC power was limited to 800 kW in each British Class 43 locomotive, the battery bank mass to 5 tonnes, and the hydrogen tanks to 86.

ESS Optimization study In this section we demonstrate how the energy storage mix on-board the locomotive impacts certain key parameters such as the number of continuous operational hours without refueling, regenerated energy as a percentage of the net consumed energy, and net SOC change.

Figure 4.40 presents a two dimensional view of the ESS optimization problem that arises when deciding on energy storage allocation. he discrete ESS combinations selected for simulation are shown as dotted points in the same figure. The lightest combination considered for simulation is one where the hydrogen storage mass was 2.5 tonnes, and the battery mass was 1 tonne.

The use of ballast is necessary in FCB hybrids due to the low density of hydrogen. Only ESS combinations that lie on the mass constraint line do not require the use of a ballast. The further from the mass constraint line a combination is, the more ballast is needed.

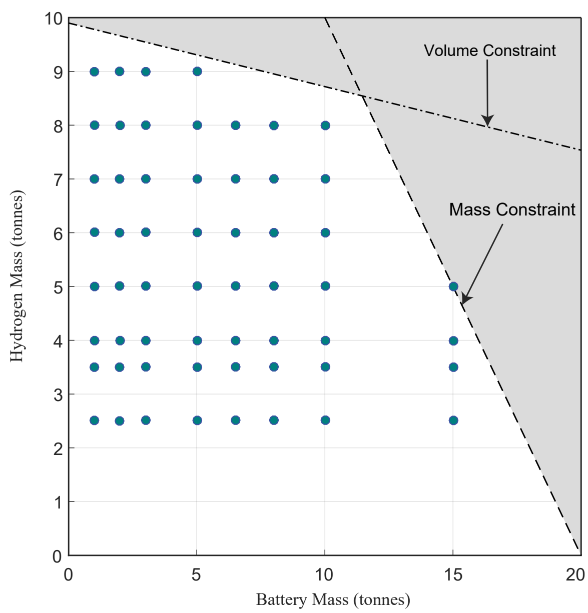

Figure 4.40: A two dimensional illustration of the ESS sizing optimization problem that highlights the cases considered for simulation. The ESS in this study is a FCB hybrid, and the physical constraints are for a British Class 43 locomotive. The dotted circles represent the ESS cases selected for simulation.

Similar to the conclusions made in the Trehafod to Treherbet FCB study presented earlier, Figure 4.41 highlights how the number of hours of continuous operation (range of travel) is a function of the on-board hydrogen mass. This is mainly due to the higher energy density of hydrogen gas in comparison to lithium-ion batteries.

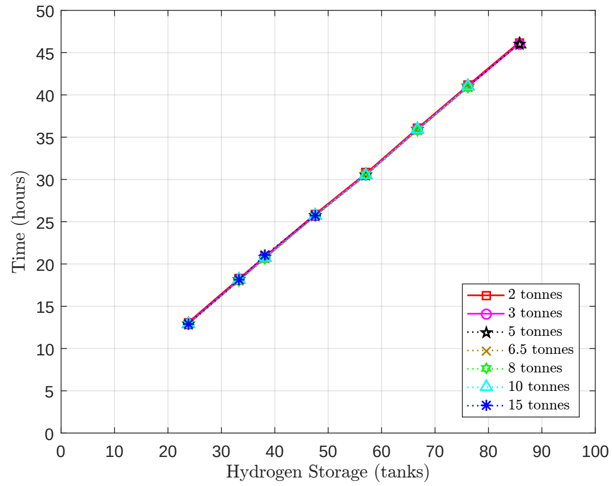

Figure 4.41: Number of hours of continuous operation without refueling as a function of the on-board hydrogen storage mass.

Figure 4.42 presents the percentage change in the battery bank's SOC per operational hour as a function of battery mass assuming that each motive unit had a 800 kW FC system as the prime mover. The figure shows that the battery bank's SOC is independent of the on-board hydrogen storage. Since the energy supplied by the battery bank is fixed, increasing the battery bank's mass by a factor decreases the hourly SOC change by the same factor as presented in the figure.

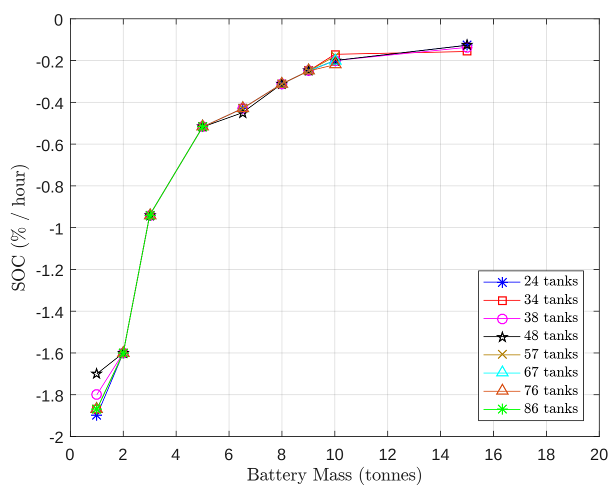

Figure 4.42: The battery bank's rate of loss of charge as a function of its mass.

Energy savings due to regeneration as a function of battery mass are presented in Figure 4.43. The smallest increment of battery bank mass considered was 100 kg, leading us to conclude that the battery mass threshold for maximum regeneration is less than 100 kg.

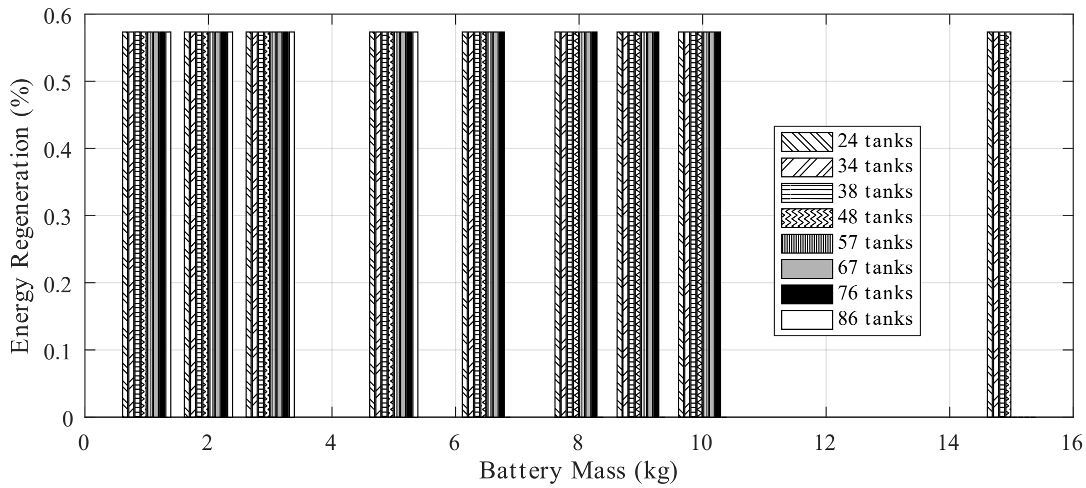

Figure 4.43: Regenerated energy as a percentage of net energy consumed as a function of the on-board ESS mix.

Chapter 5

Conclusions and Recommendations

Stated broadly, the goal of the research work presented in this thesis was to assess the technical feasibility of various clean power sources stored on-board moving railway vehicles. In particular, battery/supercapacitor hybrids versus fuel cell/battery hybrids were examined. Two case studies that present the extremes of trip length were chosen. Simulink models for the different powertrains were built and simulated. The discretization of component volumes and corresponding masses enabled the production of a set of feasible solutions. Results of model simulation at the chosen discrete points were plotted, which enabled the examination of the impact of component sizing on key trip parameters. It is important to remember that all the simulated case studies assumed a fast-as-possible velocity profile. This assumption has a significant impact on energy consumption, most notably on the ability to regenerate energy.

Lithium ion batteries proved to be very capable in handling all the required transient power demand. In regeneration, supercapacitors outperformed lithium-ion batteries and almost eliminated the need for frictional brakes. A study to measure the potential financial savings from reduced mechanical brake wear and tear versus the cost of installing supercapacitor banks is therefore recommended. The studies conducted lead us to conclude that maximizing battery storage on-board a railway vehicle maximizes the range of catenaryless operation. In fact, it has been demonstrated that complete elimination of the overhead electrification infrastructure is possible if a sufficient number of batteries are used, moreover, space on-board was not the limiting factor.

For a fixed mass BSC ESS, volume restriction was not a problem. The most volume restricting ESS combination occupied less than 50% of the available volume. The more batteries, the less supercapacitors, and the less volume occupied. Energy regeneration was unaffected by ESS sizing mix over a specified minimum. Overall, energy regeneration was insignificant for the longer trip, but that is case specific.

Although very inefficient when compared to lithium-ion batteries and supercapacitors, hydrogen fuel cells still managed to outperform other sources when it came to range extension. However, they proved unable to handle transient power demand and had to be hybridized with a more dynamic power source. The robustness of the control system employed in the simulated FCB models kept the fuel economy almost constant as fuel cell stack power was increased. This would lead us to conclude that a more robust control system could enable the use of fuel cell stacks with maximum power levels lower than the average trip power demand. This may reduce powertrain cost without affecting the fuel economy.

Since a railway vehicle's mass must remain unaffected by ESS sizing changes for traction purposes, ballast was required in the case of hydrogen storage. The low density of hydrogen, even when pressurized, meant that the volume restricted compartment on-board the railway vehicle limited the amount of hydrogen stored. Yet, enough hydrogen could be stored to outlast BSC hybrids.

The main conclusion is that clean ESS technology on-board moving railway vehicles are highly feasible from a technical point of view as a gateway technology to electrify the North American railway fleet. It is therefore recommended that an independent cost benefit analysis for the given case studies be conducted. For a more meaningful feasibility assessment, WTW emissions analysis of the proposed solutions is recommended.

Future work:

- It is recommended to conduct a study on the potential financial savings from reduced mechanical brake wear and tear versus the cost of installing supercapacitor banks.
- An independent cost-benefit study for the case studies presented in this thesis is recommended.
- WTW emissions analysis of the proposed solutions is recommended.
- A study on the application of the proposed technologies to freight rail systems is recommended.

Bibliography

[1] E. Boozarjomehri, E. Morrison, I. Roth, and G. Lovegrove, "Moving Away From Diesel and Towards All-Electric Locomotives in North America: Planning and Logistics of Ultra-Capacitor/Battery Technology," in *2012 Joint Rail Conference*, 2012, p. 777. [Online]. Available: http://www.scopus.com/inward/record.url?eid=2-s2.0-84892649247{&}partnerID=tZOtx3y1 → pages 2

[2] M. Ogasa, "Application of energy storage technologies for electric railway vehicles-examples with hybrid electric railway vehicles," *IEEJ Transactions on Electrical and Electronic Engineering*, vol. 5, no. 3, pp. 304–311, 2010. → pages 2, 9, 12, 13

[3] L. Mir, I. Etxeberria-Otadui, D. Arenaza, I. Perez, I. Sarasola, and T. Nieva, "A Supercapacitor Based Light Rail Vehicle : System design and operations modes," in *IEEE Energy Conversion Congress and Exposition*, vol. 146. San Jose, CA: IEEE, 2009, pp. 1632–1639. → pages

[4] Z. Gao, J. Fang, Y. Zhang, D. Sun, L. Jiang, and X. Yang, "Control Research of Supercapcitor Energy Storage System for Urban Rail Transit Network," in *Information Science, Electronics and Electrical Engineering (ISEEE), 2014 International Conference on*, 2014, pp. 181–185. → pages

[5] I. Szenasy, "Capacitive and hybrid energy storages for metro railcars," *IEEE International Electric Vehicle Conference*, pp. 8–12, 2013. → pages 2

[6] A. R. Miller, K. S. Hess, D. L. Barnes, and T. L. Erickson, "System design of a large fuel cell hybrid locomotive," *Journal of Power Sources*, vol. 173, no. 2 SPEC. ISS., pp. 935–942, 2007. → pages 3, 14, 24

[7] C. R. Akli, B. Sareni, X. Roboam, and A. Jeunesse, “Integrated optimal design of a hybrid locomotive with multiobjective genetic algorithms,” *International Journal of Applied Electromagnetics and Mechanics*, vol. 30, no. 3-4, pp. 151–162, 2009. → pages 3, 26

[8] A. Jaafar, C. R. Akli, B. Sareni, X. Roboam, and A. Jeunesse, “Sizing and energy management of a hybrid locomotive based on flywheel and accumulators,” *IEEE Transactions on Vehicular Technology*, vol. 58, no. 8, pp. 3947–3958, 2009. → pages 3, 24

[9] M. Meinert, P. Prenleloup, S. Schmid, and R. Palacin, “Energy storage technologies and hybrid architectures for specific diesel-driven rail duty cycles: Design and system integration aspects,” *Applied Energy*, vol. 157, pp. 619–629, 2015. → pages 4, 11

[10] L. Yu, J. H. He, H. T. Yip, F. Du, Z. Q. Bo, and J. Hu, “Simulation of regenerative braking in DC railway system based on MATLAB/Simulink,” *Universities Power Engineering Conference UPEC 2010 45th International*, no. iv, pp. 1–5, 2010. → pages 8

[11] S. M. Mousavi Gazafrudi, A. Tabakhpour Langerudy, E. F. Fuchs, and K. Al-Haddad, “Power Quality Issues in Railway Electrification: A Comprehensive Perspective,” *IEEE Transactions on Industrial Electronics*, vol. 62, no. 5, pp. 3081–3090, 2015. → pages 8

[12] A. Ogunsola, A. Mariscotti, and L. Sandrolini, “Estimation of stray current from a DC-electrified railway and impressed potential on a buried pipe,” *IEEE Transactions on Power Delivery*, vol. 27, no. 4, pp. 2238–2246, 2012. → pages 9

[13] L. Bertolini, M. Carsana, and P. Pedeferri, “Corrosion behaviour of steel in concrete in the presence of stray current,” *Corrosion Science*, vol. 49, no. 3, pp. 1056–1068, 2007. → pages 9

[14] M. Steiner, M. Klohr, and S. Pagiela, “Energy storage system with Ultracaps on board of railway vehicles,” *European Conference on Power Electronics and Applications*, 2007. → pages 9, 13

[15] F. Kiessling, *Contact Lines for Electric Railways. Planning, Design, Implementation, Maintenance.* Erlangen : Publicis. → pages 9

[16] R. Hou, Y. Yang, and A. Emadi, “Hybrid electric locomotive powertrains,” *IEEE Transportation Electrification Conference and Expo, ITEC Asia-Pacific*, pp. 1–6, 2014. → pages 10

[17] “Electrical Transportation Annual Report of Committee on Transportation,” Detroit, Michigan, Tech. Rep., 1927. → pages 10

[18] E. I. Altman, “Predicting railroad bankruptcies in America,” *The Bell Journal of Economics and Management Science*, vol. 4, no. 1, pp. 184–211, 1973. → pages 10

[19] T. Murray, *The Milwaukee Road.* St. Paul, Minn. : MBI Pub. Co. → pages 10

[20] A. Hoffrichter, J. Silmon, F. Schmid, S. Hillmansen, and C. Roberts, “Feasibility of discontinuous electrification on the Great Western Main Line determined by train simulation,” *Proceedings of the Institution of Mechanical Engineers, Part F: Journal of Rail and Rapid Transit*, vol. 227, no. 3, pp. 296–306, 2012. → pages 10

[21] R. Cousineau, “Development of a Hybrid Switcher Locomotive,” *IEEE Instrumentation & Measurement Magazine*, no. February, pp. 25–29, 2006. → pages 11

[22] S. Subhedar, P. Majumdar, R. Kilaparti, and D. Schroeder, “Duty cycle and transport phenomenon analysis of battery storage system for hybrid locomotive application,” in *ASME 2012 Rail Transportation Division Fall Technical Conference*, Omaha, Nebraska, 2012, pp. 169–179. → pages 24

[23] O. Mitsuyuki, T. Shinji, F. Takehito, T. Eiichi, K. Takashi, and S. Motomi, “Development of a New Energy Train hybrid type ,” in *The World Congress on Railway Research 2003*, 2003, pp. 48–54. → pages 11

[24] H. Hirose, K. Yoshida, and K. Shibanuma, “Development of catenary and storage battery hybrid train system,” in *Electrical Systems for Aircraft, Railway and Ship Propulsion.* IEEE, oct 2012, pp. 1–4. → pages vii, 12

[25] G. D. Marin, G. F. Naterer, and K. Gabriel, “Rail transportation by hydrogen vs. electrification - Case study for Ontario, Canada, II: Energy supply and distribution,” *International Journal of Hydrogen Energy*, vol. 35, no. 12, pp. 6097–6107, 2010. → pages 14

[26] ——, "Rail transportation by hydrogen vs. electrification - Case study for Ontario, Canada, I: Propulsion and storage," *International Journal of Hydrogen Energy*, vol. 35, no. 12, pp. 6097–6107, 2010. → pages 14

[27] A. R. Miller, "Tunneling and mining applications of fuel cell vehicles," *Fuel Cells Bulletin*, vol. 3, no. 22, pp. 5–9, 2000. → pages 14

[28] C. R. Akli, X. Roboam, B. Sareni, and A. Jeunesse, "Energy management and sizing of a hybrid locomotive," *European Conference on Power Electronics and Applications*, vol. c, pp. 1–10, 2007. → pages 14, 24

[29] A. Hoffrichter, P. Fisher, J. Tutcher, S. Hillmansen, and C. Roberts, "Performance evaluation of the hydrogen-powered prototype locomotive 'Hydrogen Pioneer'," *Journal of Power Sources*, vol. 250, pp. 120–127, 2014. → pages 15

[30] W. Chen, F. Peng, Z. Liu, Q. Li, and C. Dai, "System integration of China's first PEMFC locomotive," *Journal of Modern Transportation*, vol. 21, no. 3, pp. 163–168, 2013. → pages 15

[31] O. Tremblay, "Experimental Validation of a Battery Dynamic Model for EV Applications Experimental Validation of a Battery Dynamic Model for EV Applications," vol. 3, no. October, pp. 289–298, 2015. → pages vii, 16

[32] S. N. Motapon, O. Tremblay, and L.-A. Dessaint, "Development of a generic fuel cell model: application to a fuel cell vehicle simulation," *International Journal of Power Electronics*, vol. 4, no. 6, pp. 505–522, 2012, pMID: 52427. → pages vii, 17, 20

[33] J.-J. Hwang, Y.-J. Chen, and J.-K. Kuo, "The study on the power management system in a fuel cell hybrid vehicle," *International Journal of Hydrogen Energy*, vol. 37, no. 5, pp. 4476–4489, 2012. → pages vi, vii, 17, 20, 117

[34] J. Cho, H. S. Kim, and K. Min, "Transient response of a unit proton-exchange membrane fuel cell under various operating conditions," *Journal of Power Sources*, vol. 185, no. 1, pp. 118–128, 2008. → pages vii, 18, 19

[35] C. Liu and L. Liu, "Optimal power source sizing of fuel cell hybrid vehicles based on Pontryagin's minimum principle," *International Journal of Hydrogen Energy*, vol. 40, no. 26, pp. 8454–8464, 2015. → pages 18

[36] C. H. Zheng, N. W. Kim, and S. W. Cha, "Optimal control in the power management of fuel cell hybrid vehicles," *International Journal of Hydrogen Energy*, vol. 37, no. 1, pp. 655–663, 2012. → pages 18

[37] R. L. Borup, J. R. Davey, F. H. Garzon, D. L. Wood, and M. A. Inbody, "PEM fuel cell electrocatalyst durability measurements," *Journal of Power Sources*, vol. 163, no. 1 SPEC. ISS., pp. 76–81, 2006. → pages 18

[38] W. S. Lin and C. H. Zheng, "Energy management of a fuel cell/ultracapacitor hybrid power system using an adaptive optimal-control method," *Journal of Power Sources*, vol. 196, no. 6, pp. 3280–3289, 2011. → pages 19

[39] M. C. Kisacikoglu, M. Uzunoglu, and M. S. Alam, "Load sharing using fuzzy logic control in a fuel cell/ultracapacitor hybrid vehicle," *International Journal of Hydrogen Energy*, vol. 34, no. 3, pp. 1497–1507, 2009. → pages 19

[40] P. Thounthong, S. Raël, and B. Davat, "Energy management of fuel cell/battery/supercapacitor hybrid power source for vehicle applications," *Journal of Power Sources*, vol. 193, no. 1, pp. 376–385, 2009. → pages 19, 25, 57

[41] A. Arce, A. J. del Real, and C. Bordons, "MPC for battery/fuel cell hybrid vehicles including fuel cell dynamics and battery performance improvement," *Journal of Process Control*, vol. 19, no. 8, pp. 1289–1304, 2009. → pages 20

[42] Z. Yu, D. Zinger, and A. Bose, "An innovative optimal power allocation strategy for fuel cell, battery and supercapacitor hybrid electric vehicle," *Journal of Power Sources*, vol. 196, no. 4, pp. 2351–2359, 2011. → pages 20

[43] C. Y. Li and G. P. Liu, "Optimal fuzzy power control and management of fuel cell/battery hybrid vehicles," *Journal of Power Sources*, vol. 192, no. 2, pp. 525–533, 2009. → pages 20

[44] P. Thounthong, P. Tricoli, and B. Davat, "Performance investigation of linear and nonlinear controls for a fuel cell/supercapacitor hybrid power plant," *International Journal of Electrical Power and Energy Systems*, vol. 54, pp. 454–464, 2014. → pages 20

[45] T. Q. Hua, R. K. Ahluwalia, J. K. Peng, M. Kromer, S. Lasher, K. McKenney, K. Law, and J. Sinha, "Technical assessment of compressed hydrogen storage tank systems for automotive applications," *International Journal of Hydrogen Energy*, vol. 36, no. 4, pp. 3037–3049, 2011. → pages 21

[46] J. Baert, S. Jemei, D. Chamagne, D. Hissel, S. Hibon, and D. Hegy, "Sizing of a hybrid locomotive," in *Vehicle Power and Propulsion Conference*. IEEE, 2011. → pages 24

[47] D. Fares, R. Chedid, F. Panik, S. Karaki, and R. Jabr, "Dynamic programming technique for optimizing fuel cell hybrid vehicles," *International Journal of Hydrogen Energy*, vol. 40, no. 24, pp. 7777–7790, 2015. → pages 26

[48] D. Tarsitano, L. Mazzola, S. Arrigoni, F. L. Mapelli, and F. Cheli, "Energy management algorithms comparison for an electric bus with an hybrid energy storage system by means of dynamic programming," *IEEE Vehicular Technology Conference*, 2014. → pages

[49] S. Lu, S. Hillmansen, and C. Roberts, "A power-management strategy for multiple-unit railroad vehicles," *IEEE Transactions on Vehicular Technology*, vol. 60, no. 2, pp. 406–420, 2011. → pages 26

[50] D. Fares, R. Chedid, S. Karaki, R. Jabr, F. Panik, H. Gabele, and Y. Huang, "Optimal power allocation for a FCHV based on linear programming and PID controller," *International Journal of Hydrogen Energy*, vol. 39, no. 36, pp. 21 724–21 738, 2014. → pages 26

[51] V. Herrera, A. Saez-de Ibarra, A. Milo, H. Gaztanaga, and H. Camblong, "Optimal Energy Management of a Hybrid Electric using Genetic Algorithm," *Electrical Systems for Aircraft, Railway, Ship Propulsion and Road Vehicles (ESARS), 2015 International Conference on*, no. 6, pp. 3–5, 2015. → pages 26

[52] M. Jain, C. Desai, and S. S. Williamson, "Genetic algorithm based optimal powertrain component sizing and control strategy design for a fuel cell hybrid electric bus," *Vehicle Power and Propulsion Conference, 2009. VPPC '09. IEEE*, pp. 980–985, 2009. → pages 26

[53] J. Ribau, R. Viegas, A. Angelino, A. Moutinho, and C. Silva, "A new offline optimization approach for designing a fuel cell hybrid bus," *Transportation Research Part C: Emerging Technologies*, vol. 42, pp. 14–27, 2014. → pages 26

[54] C. Dextreit and I. Kolmanovsky, V, "Game Theory Controller for Hybrid Electric Vehicles," *IEEE Transactions on Control Systems Technology*, vol. 22, no. 2, pp. 652–663, 2014. → pages 26

[55] J. Shen and A. Khaligh, "A Supervisory EnergyManagement Control Strategy in a Battery/Ultracapacitor Hybrid Energy Storage System," *IEEE Transactions on Transportation Electrification*, vol. 1, no. 3, pp. 223–231, 2015. → pages 26

[56] M. Jain, C. Desai, N. Kharma, and S. S. Williamson, "Optimal Powertrain Component Sizing of a Fuel Cell Plug-in Hybrid Electric Vehicle Using Multi- Objective Genetic Algorithm," *IECON '09. 35th Annual Conference of IEEE on Industrial Electronics*, pp. 3741–3746, 2009. → pages 26

[57] Q. Wu, S. Luo, and C. Cole, "Longitudinal dynamics and energy analysis for heavy haul trains," *Journal of Modern Transportation*, vol. 22, no. 3, pp. 127–136, 2014. → pages 33

[58] S. Lu, S. Hillmansen, T. K. Ho, and C. Roberts, "Single-train trajectory optimization," *IEEE Transactions on Intelligent Transportation Systems*, vol. 14, no. 2, pp. 743–750, 2013. → pages 34

[59] J. Bernard, M. Hofer, U. Hannesen, A. Toth, A. Tsukada, F. N. Büchi, and P. Dietrich, "Fuel cell/battery passive hybrid power source for electric powertrains," *Journal of Power Sources*, vol. 196, no. 14, pp. 5867–5872, 2011. → pages 64

[60] P. Garcia, L. M. Fernandez, C. A. Garcia, and F. Jurado, "Energy management system of

fuel-cell-battery hybrid tramway," *IEEE Transactions on Industrial Electronics*, vol. 57, no. 12, pp. 4013–4023, 2010. → pages 64

[61] a. Ravey, N. Watrin, B. Blunier, and A. Miraoui, "Energy sources sizing for hybrid fuel cell vehicles based on statistical description of driving cycles," *Ieee Transactions on Vehicular Technology*, vol. 60, no. 9, pp. 4164–4174, 2010. → pages 64

[62] P. Thounthong, V. Chunkag, P. Sethakul, B. Davat, and M. Hinaje, "Comparative study of fuel-cell vehicle hybridization with battery or supercapacitor storage device," *IEEE Transactions on Vehicular Technology*, vol. 58, no. 8, pp. 3892–3904, 2009. → pages 64

[63] A. Fadel and B. Zhou, "An experimental and analytical comparison study of power management methodologies of fuel cell-battery hybrid vehicles," *Journal of Power Sources*, vol. 196, no. 6, pp. 3271–3279, 2011. → pages 64

[64] D. R. Peterman, J. Frittelli, and W. J. Mallett, "High Speed Rail (HSR) in the United States," Tech. Rep., 2009. → pages 93

Appendix

Appendix A

Tables

Table A.1: The specifications of Panasonic's UPF454261 Lithium-ion battery.

UPF454261 specifications			
Rated capacity:		1450	mAh
Nominal voltage:		3.7	V
Weight:		27.0	g
Energy density:	Volumetric	462	Wh/l
	Gravimetric	199	Wh/kg

Table A.2: The specifications of Maxwell's BCAP3400 supercapacitor.

BCAP3400 specifications			
Rated capacitance:		3400	F
Rated capacity:		1400	mAh
Nominal voltage:		2.85	V
Weight:		520	g
Energy density:	Volumetric	7.9e-6	Wh/l
	Gravimetric	7.7	Wh/kg

Table A.3: The specifications of the 100 kW *Honda FCX* PEMFC model used in this study as obtained from [33].

PEMFC specifications			
Stack power:	Nominal	85.5	kW
	Maximum	100	kW
Internal resistance:		0.17572	Ω
Nernst voltage:		1.1729	V/cell
Nominal utilization:	Hydrogen	95.24	%
	Oxidant	50.03	%
Nominal consumption:	Fuel	794.4	slpm
	Air	1891	slpm
Exchange current:		0.024152	A
Exchange coefficient:		1.1912	
Fuel composition:		99.95	%
Oxidant composition:		21	%
Fuel flow rate at nominal hydrogen utilization:	Nominal	374.8	lpm
	Maximum	456.7	lpm
Air flow rate at nominal oxidant utilization:	Nominal	1698	lpm
	Maximum	2069	lpm
System temperature:		368	K
Fuel supply pressure:		3	bar
Air supply pressure:		3	bar

Table A.4: The specifications of British Class 43 Locomotive.

Physical Specs	
Length	17.79 m
Width	2.74 m
Height	3.8 m
Wheel Diameter	1.016 m
Mass	70.25 tonnes
Fuel Capacity	4500 L
Performance Specs	
Maximum Speed	200 km/h
Maximum Engine Power	1600 kW

Table A.5: The gradient profile of the Trehafod to Treherbert trip.

Distance(km)	Grade(m/km)
0	9.90099
0.14079	14.70588
0.33387	13.69863
0.46259	21.2766
0.51086	3.69004
0.57522	2.27273
0.6074	2.5
0.83266	2.7248
0.96138	10.20408
1.04183	9.00901
1.21882	7.19424
1.54062	9.25926
1.58889	11.76471
1.63716	10.52632
1.68543	5
.	.
.	.
.	.
.	.
.	.
.	.
.	.
11.17853	8.54701
11.40379	9.70874
11.66123	7.93651
11.75777	5.74713
12.16002	6.89655
12.54618	7.87402
12.75535	6.84932
12.94843	8.26446
13.54376	6.99301
13.70466	10.20408
13.84947	11.90476

Table A.6: The speed limit profile of the Trehafod to Treherbert trip.

Distance (km)	Velocity (km/h)
0	48.27
0.30168	48.27
0.36202	64.36
.	.
.	.
1.63094	64.36
1.72967	40.225
.	.
.	.
1.99661	40.225
1.99935	32.18
2.03866	32.18
2.07797	64.36
.	.
.	.
4.18339	64.36
4.58564	80.45
.	.
.	.
9.01042	80.45
9.31211	56.315
9.5882	56.315
9.58911	56.315
9.61379	96.54
.	.
.	.
12.94879	96.54
13.79717	80.45
13.83739	80.45
13.87396	80.45
13.9023	0